

Shielding and mediating of hydrogen bonding in amide-based (macro)molecules

Citation for published version (APA):

Harings, J. A. W. (2009). *Shielding and mediating of hydrogen bonding in amide-based (macro)molecules*. [Phd Thesis 1 (Research TU/e / Graduation TU/e), Chemical Engineering and Chemistry]. Technische Universiteit Eindhoven. <https://doi.org/10.6100/IR641657>

DOI:

[10.6100/IR641657](https://doi.org/10.6100/IR641657)

Document status and date:

Published: 01/01/2009

Document Version:

Publisher's PDF, also known as Version of Record (includes final page, issue and volume numbers)

Please check the document version of this publication:

- A submitted manuscript is the version of the article upon submission and before peer-review. There can be important differences between the submitted version and the official published version of record. People interested in the research are advised to contact the author for the final version of the publication, or visit the DOI to the publisher's website.
- The final author version and the galley proof are versions of the publication after peer review.
- The final published version features the final layout of the paper including the volume, issue and page numbers.

[Link to publication](#)

General rights

Copyright and moral rights for the publications made accessible in the public portal are retained by the authors and/or other copyright owners and it is a condition of accessing publications that users recognise and abide by the legal requirements associated with these rights.

- Users may download and print one copy of any publication from the public portal for the purpose of private study or research.
- You may not further distribute the material or use it for any profit-making activity or commercial gain
- You may freely distribute the URL identifying the publication in the public portal.

If the publication is distributed under the terms of Article 25fa of the Dutch Copyright Act, indicated by the "Taverne" license above, please follow below link for the End User Agreement:

www.tue.nl/taverne

Take down policy

If you believe that this document breaches copyright please contact us at:

openaccess@tue.nl

providing details and we will investigate your claim.

Shielding and Mediating of Hydrogen Bonding in Amide-based
(Macro)Molecules

PROEFSCHRIFT

ter verkrijging van de graad van doctor aan de
Technische Universiteit Eindhoven, op gezag van de
Rector Magnificus, prof.dr.ir. C.J. van Duijn, voor een
commissie aangewezen door het College voor
Promoties in het openbaar te verdedigen
op donderdag 2 april 2009 om 16.00 uur

door

Jules Armand Wilhelmina Harings

geboren te Heerlen

Dit proefschrift is goedgekeurd door de promotoren:

prof.dr. S. Rastogi
en
prof.dr. P.J. Lemstra

A catalogue record is available from the Eindhoven University of Technology Library.

ISBN: 978-90-386-1622-3

Copyright © 2009 by J.A.W. Harings

Printed at Linssen Grafische Vormgevers, Maasbracht, The Netherlands.

Cover picture: Shielding of hydrogen bonding by Berk Hess.

Cover design: Jules Harings and Roel Gerardts (Linssen Grafische Vormgevers).

This research forms part of the research program of the Dutch Polymer Institute (DPI), Technology Area Bio-inspired Polymers, DPI project #603.

Voor pap,

Contents

Summary	ix
Chapter 1 Introduction	1
1.1 Polymer crystallization.....	1
1.2 Extended chain crystals in polyethylene.....	2
1.3 Hydrogen bonding in polyamides; enhanced secondary interactions.....	3
1.4 Hydrogen bonding in silk; inspiration by natural silk spinning.....	6
1.5 Dissolution of polyamides in the superheated state of water.....	7
1.6 Objective of the thesis.....	8
1.7 Outline of the thesis.....	9
1.8 References.....	10
Chapter 2 The role of superheated water on the crystallization of N,N'-1,2-ethanediyl-bis(6-hydroxy-hexanamide); implications on crystallography and phase transitions	13
2.1 Introduction.....	14
2.2 Experimental section.....	16
2.2.1 <i>Materials</i>	16
2.2.2 <i>Differential scanning calorimetry</i>	16
2.2.3 <i>Wide angle X-ray diffraction</i>	17
2.2.4 <i>Optical microscopy</i>	17
2.3 Results and discussion.....	18
2.3.1 <i>Phase transitions in EDHA</i>	18
2.3.2 <i>Influence of water molecules on hydrogen bonding</i>	24
2.4 Conclusions.....	30
2.5 References.....	31

Chapter 3	The role of superheated water on shielding and mediating hydrogen bonding in N,N'-1,2 ethanediyl-bis(6-hydroxy-hexanamide) crystallization	33
3.1	Introduction.....	34
3.2	Experimental section.....	35
3.2.1	<i>Materials</i>	35
3.2.2	<i>Fourier transfer infrared spectroscopy</i>	36
3.2.3	<i>Solid state nuclear magnetic resonance spectroscopy</i>	37
3.3	Results and discussion.....	37
3.3.1	<i>Hydrogen bonding in melt crystallized EDHA</i>	37
3.3.2	<i>Melt versus H₂O crystallization; the localization of H₂O molecules at RT</i> ...	43
3.3.3	<i>The migration of water molecules; a crystal transformation</i>	46
3.4	Conclusions.....	54
3.5	References.....	56
Chapter 4	Erasing conformational limitations in N,N'-1,4-butanediyl-bis(6-hydroxy-hexanamide) crystallization from the superheated state of water	59
4.1	Introduction.....	60
4.2	Experimental section.....	61
4.2.1	<i>Materials</i>	61
4.2.2	<i>Differential scanning calorimetry</i>	62
4.2.3	<i>Wide angle X-ray diffraction</i>	62
4.2.4	<i>Optical microscopy</i>	63
4.2.5	<i>Fourier transfer infrared spectroscopy</i>	63
4.2.6	<i>Solid state nuclear magnetic resonance spectroscopy</i>	64
4.3	Results and discussion.....	64
4.3.1	<i>Thermal motion and hydrogen bonding in melt crystallized BDHA</i>	64
4.3.2	<i>Crystallization from the superheated state of water; chain packing and hydrogen bonding efficiencies</i>	71
4.3.3	<i>Influence of enclosed H₂O molecules on hydrogen bonding efficiencies</i>	80
4.4	Conclusions.....	84
4.5	References.....	85

Chapter 5	Shielding and de-shielding of hydrogen bonding for the development of oriented polyamide crystals; inspiration by natural silk spinning	87
5.1	Introduction.....	88
5.2	Experimental section.....	89
5.2.1	<i>Polyamides, kosmotropic cations and chaotropic anions</i>	89
5.2.2	<i>Dissolution in superheated water; differential scanning calorimetry</i>	90
5.2.3	<i>Restoration of hydrogen bonding; crystallization</i>	90
5.2.4	<i>Characterization by FTIR, NMR and WAXD</i>	91
5.2.5	<i>Fourier transfer infrared spectroscopy</i>	91
5.3	Results and discussion.....	92
5.3.1	<i>Influence of ions on the dissolution behavior in superheated water</i>	92
5.3.2	<i>Shielding of hydrogen bonding on crystallization from the superheated state of water</i>	95
5.3.3	<i>Re-establishment of hydrogen bonding</i>	97
5.4	Conclusions.....	101
5.5	References.....	102
Chapter 6	Strain induced crystallization of polyamide 46 from aqueous lithium iodide solution; a technological assessment	105
6.1	Introduction.....	106
6.2	Experimental section.....	109
6.2.1	<i>Materials and sample preparation</i>	109
6.2.2	<i>Dynamic mechanical thermal analyses</i>	109
6.2.3	<i>Tensile testing</i>	110
6.2.4	<i>Differential scanning calorimetry</i>	110
6.2.5	<i>Solid state ⁷Li nuclear magnetic resonance spectroscopy</i>	110
6.2.6	<i>Wide angle X-ray diffraction</i>	111
6.2.7	<i>Polarized infrared spectroscopy</i>	111
6.3	Results and discussion.....	112
6.3.1	<i>Crystal and orientation development in semicrystalline PA46 at ambient conditions</i>	112
6.3.2	<i>Characterization of semicrystalline and amorphous samples</i>	113
6.3.3	<i>Structure development on drawing; do the ions migrate?</i>	117
6.3.4	<i>Structure development on complete removal of ion in superheated water...</i>	124
6.4	Conclusions and recommendations.....	126
6.4.1	<i>Conclusions</i>	126

6.4.2	<i>Recommendations</i>	127
6.5	References.....	128
	Samenvatting.....	131
	Acknowledgements.....	135
	Curriculum Vitae.....	137
	List of Publications.....	138

Summary

Polymers are long chain molecules comprising continuously repeating building blocks, monomers, which are chemically linked via covalent bonds, for example the C-C bond in polyethylene. A distinction can be made in biopolymers that are made in nature and synthetic polymers that are produced by the chemical industry (plastics).

Properties of polymeric materials are not only determined by the primary chemical structure, i.e. the chemical composition of the polymer chain, but also by the secondary interactions between the chains (intermolecular interactions) and the conformation (shape). Especially in biopolymers, a delicate balance between the primary chemical structure, i.e. the chain composition, and intra- and intermolecular interactions is encountered. A well known example is the double helix in DNA, which carries the essence of life. Another example is peptides, or proteins, where unique conformations are dependent on a balance between the sequence of monomer units, here amino acids, and secondary interactions (e.g. hydrogen bonding) between monomers in a single molecule, the formation of the known α -helix and β -sheet structures, and/or between molecules.

Synthetic polymers are in comparison to biopolymers chemically less sophisticated, rendering higher thermal stability. Hence, synthetic polymers can be directly processed via melt routes into end products, for example by means of injection molding or extrusion, while biopolymers such as cellulose (wood) have to be chipped. The conformation and secondary interactions between molecules are essential in synthetic polymers as well. An extreme example in this respect is the simplest polymer on earth: polyethylene (PE). Taking polyethylene as precursor, the industry produces flexible films and containers on one hand, and superstrong fibers with a specific strength and stiffness larger than steel on the other. In these fibers all polymer molecules exist in extended chain conformation perfectly aligned in the fiber direction. Between the apolar PE molecules only relatively weak van der Waals forces reside, but with sufficient length of the molecules the sum of the weak secondary interactions between the molecules induces sufficient frictional forces between the chains that the stress is transferred to the covalent bonds in the main chain upon deformation (in the fiber direction), resulting in high strength and stiffness. These superstrong polyethylene fibers can be considered as 1-dimensional diamond at fast deformation rates, whereas at low deformation rates, i.e. long time-scales, creep occurs. Another disadvantage of these PE fibers is the relatively low melting temperature, approximately 150°C.

More ideal would be the use of polyamides (nylons) as precursor for superstrong fibers since polyamides prevent creep by hydrogen bonding and possess high melting temperatures. Chemically polyamides are similar to proteins where the monomers are connected by amide moieties. Polymer chemists often describe proteins as decorated nylons

(nylon 2). In the past a lot of industrial research effort has been addressed to the development of superstrong polyamide fibers in a similar way as PE, i.e. drawing and aligning the chains in the fiber direction, unfortunately without success. In processing polyamides, either from the melt or from solution, cooling induces crystallization into chain folded crystals that are comparable with stacks of β -sheets in proteins. Because of relatively strong interchain hydrogen bonding the chain folded crystals cannot be unfolded like in the case of polyethylene.

The aim of the thesis is to shield hydrogen bonding in polyamides temporarily during processing and drawing and to restore the hydrogen bonding once the chains are ideally aligned and extended. Based on the dissolution of polyamides in the superheated state of water (PhD thesis Esther Vinken, TU/e 2008) and inspired by natural silk spinning, where in the glands of spiders and silk worms hydrogen bonded moieties of the proteins are shielded and mediated by water molecules, salts (ions) and pH, a new reversible shielding route in polyamide processing is introduced.

Since the amorphous phase in polyamides imposes limitations in investigating the role of water molecules on crystalline hydrogen bonding in polyamides after crystallization from the superheated state of water, low molar mass model compounds, expected to represent the crystalline domains in aliphatic polyamides, have been studied in the dissolution in, and crystallization from the superheated state of water (chapters 2, 3 and 4). The model molecules are bisamide-diols, possessing two central amide motifs (head-to-head) and two hydroxylic end groups. The aliphatic segment length, which separates the polar moieties, can be varied in analogy to polyamides.

Hydrogen bonding in polyamides resides *in* the structural amide planes, which stack to form chain folded crystals. A bisamide-diol with a short aliphatic segment between the amide motifs combined with two longer identical segments between the amide and hydroxyl moieties crystallizes in a stack of crystalline planes in which the molecules are held together by amide-amide hydrogen bonding. In case of a rather equal segment length between all polar groups in the bisamide-diol, amide-hydroxyl hydrogen bonding occurs *between* the structural amide planes. Hence, the role as a model compound is questionable in such a scenario. Nevertheless, the thermodynamic, structural and conformational behavior is, identical to polyamides, dependent on a balance between thermal motion and hydrogen bonding efficiency. Both bisamide-diols are soluble in the superheated state of water. During crystallization upon cooling the interaction of water molecules with the amide motifs erases the conformational limitations of the intrinsically rigid amide moieties. The extra degree of freedom during crystallization entails ideal crystalline hydrogen bonding, stabilizing the crystalline structures. Moreover, water molecules can be trapped within the crystal lattice during crystallization.

In the second part of the dissertation, water molecules are assisted by a series of Hofmeister ions in shielding and mediating of hydrogen bonding in polyamides. The Hofmeister series is a classification based on the hydrating nature of ions, known as

kosmotropic and promoting the organization of water molecules, or non-hydrating character of ions, referred to as chaotropic and disordering the water structures.

Close to the Brill transition temperature, a reversible crystal transformation that arises due to variations in aliphatic molecular motion and hydrogen bonding efficiencies, polyamides can be dissolved in the superheated state of water. With increasing ionic strength large non-hydrating ions of halogenic origin, such as bromide and iodide, perturb the hydrogen bonding network between water molecules. Since the diffusivity of water molecules and its solutes increases, water molecules and small strongly hydrating cations penetrate the polyamide crystal at lower temperatures, perturbing the amide-amide hydrogen bonding in the crystal. Next to the suppression of the dissolution temperature, the crystallization temperature upon cooling decreases as well. To minimize the nonpolar surface area, hydrophobic hydration entails secretion of the anions to the hydrophobic methylene segments at high ionic strength. With the interaction of the cations, preferably lithium, a charge distribution along the polyamide chains is formed that suppresses crystallization even at room temperature. Extensional deformation of the aqueous polyamide solution in excess of water results in the migration of ions, restitution of intermolecular hydrogen bonding and orientation. However, although the aqueous solutions can be deformed into drawable filaments, the strength upon crystallization is lost due to the absence of chain overlap, meaning that stress transfer between the chains is insufficient.

To promote chain overlap a processing (extrusion) route for concentrated polyamide LiI solutions is explored in chapter 6. Here, the hydrogen bonding is temporarily shielded by ions to prevent the formation of chain folded crystals during processing. Strain induced crystallization upon drawing restores amide-amide hydrogen bonding, high orientation factors and lattice perfection. Though these aspects are essential in realizing high strength and high modulus materials, the crystallinity and the melting temperature are considerably suppressed by incomplete removal of ions. Time-resolved wide angle X-ray experiments reveal that the migration of ions is primarily time-dependent at temperatures above the glass transition temperature. Efficient migration of ions in superheated water at 150°C results in high crystallinities and consequential high melting temperatures, preserving the high orientation and crystal perfection. However, experimental verification of the ultimate goal: the development of high strength and stiff polyamide fibers, could not be realized due to the intrinsic problem of removing all ions effectively that requires optimization in terms of fiber diameter and spin/drawing parameters. Ideal experimental conditions are of technological origin and require optimization in an industrial environment. The author hopes that the results in this dissertation will contribute to a new technology resulting to a new generation of (super)strong polyamide fibers.

Chapter 1

Introduction

1.1 Polymer crystallization

Polymers are long molecules having molar masses that typically range in the order of 10^4 to 10^6 g/mol and in specific cases even more. As the word “polymer” implies these molecules consist of many, *in Greek: poly*, continuously repeating molecular building blocks or parts, or *meros* in the Greek language. In the case of a well defined, regular molecular architecture, i.e. the way the building blocks or monomers are connected to each other, polymers tend to crystallize. In a quiescent molten state or solution, individual polymer chains exist in a random coil conformation that is characterized by no apparent order of the molecules¹. At high solute concentrations, as well as in the melt, long polymer chains entangle with each other resulting in physical constraints. Upon cooling from the melt or by changing the solvent characteristics the interpenetrating molecules tend to organize into crystals. The semi-crystalline nature of polymers arises as the crystallization of these long molecules is a balance between kinetics and thermodynamics.

Although Storks postulated a chain folding mechanism for crystallization of polyethylene in 1938², the concept did not flourish until the mid fifties when Ziegler discovered high density polyethylene, HDPE. Keller, Fischer and Till independently discovered chain folding in HDPE single crystals, that were grown from dilute solution³⁻⁵. Single crystal studies using electron and X-ray diffraction techniques revealed lamellar type morphology where lamellar thickness typically varied between 10 to 20 nm depending on the crystallization conditions. Electron diffraction studies performed on these crystals revealed chains perpendicular to the basal plane of the lamellae (Figure 1.1a,b). In combination with the fact that polymer chains are several hundreds of nanometers in length, it was conclusively stated that a polymer molecule folds back and forth to match the lamellar thickness. Folding of the chains in the plane of the growing faces results in chain folding along four different directions and hence four distinct sectors arise⁶.

On larger length scales quiescent crystallization of polymers, either from the melt or solution, results in the organization of lamellae into spherulitic or dendritic (or spiral terrace formation) morphologies^{1,7,8}. Polymeric spherulites, which as the word implies are small spheres, consist of an ensemble of crystal lamellae that grow radially outwards from a nucleating centre (Figure 1.1c,d). The growth process of individual lamellae is hampered in the chain direction (*c*-axis) by kinetic limitations, whereas the growth in the transverse direction is hardly restricted, resulting the crystallographic *b*-axis to be positioned along the spherulitic radius⁹. The generation of spherulitic centers and the respective growth rates are dependent on the creation of nuclei with sufficient geometrical dimensions, correlated to a

delicate balance between the bulk free energy change and interfacial free energies¹⁰. If the lamellar structure is characterized by a two-fold symmetry parallel to the growth direction, often originating in chirality, twisting of the lamellae occurs¹².

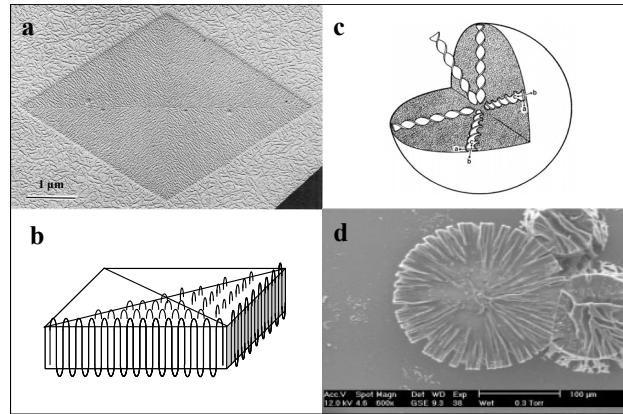


Figure 1.1: a) Visualization of a solution grown polyethylene single crystal (Wittmann and Lotz 1985)¹¹; b) Representation of a chain folded crystal with tight adjacent re-entrant folds (after Keller)⁶; c) Illustration of a polymeric spherulite, consisting of radially growing stacks of twisted crystal lamellae (from Lotz and Cheng)¹²; d) SEM micrograph of enzymatically etched polylactide spherulites. The absence of the amorphous component, realized by etching, stresses the organization of the crystalline lamellae¹³.

1.2 Extended chain crystals in polyethylene

At the end of the seventies major breakthroughs in solution spinning of polyethylene boosted the development of high modulus fibers from flexible polyethylene chains with extraordinary anisotropic properties in the fiber load direction¹⁴. Scientists were triggered by calculations performed on a single extended polymer chain by Treloar¹⁵. In a hypothetical experiment under ideal conditions, where a single polymer chain exists in vacuum and no secondary interactions are present (enthalpic contribution is zero), the deformation of a single chain reduces the entropy. Following the first law of thermodynamics the force required to deform a random coil into fully extended chain conformation is described by equation 1.1.

$$F = -T \cdot (dS/dl)_{T,P} \quad (1.1)$$

Once a chain is fully extended, further deformation requires perturbation of the covalent bonding. Following these thoughts, initial calculations on a single polyethylene

chain by Treloar revealed a theoretical tensile modulus of 182 GPa¹⁵. In the years hereafter following advanced calculations, for example semi-empirical quantum calculations based on for example spectroscopically determined force constants and ab initio quantum calculations¹⁶⁻²¹, scientists reported elastic modulus for a single chain up to 369 GPa.

Considering the size of an extended polymer molecule, for example a polyethylene molecule of less than 10 microns in length and 1 nm in diameter, a single polymer chain to produce a high performance fiber is not realistic. In order to have effective contribution of the bond energies in individual polymer chains to the anisotropic properties of the fiber, it is crucial to align the chains in the fiber load direction and to achieve optimal overlap between the chains, where the energy of the secondary interactions equals at least the energy of the covalent carbon-carbon bonds in the main chain²². Secondary interactions in polyethylene are relatively weak van der Waals forces and require ultra high molecular weights to have sufficient overlap/interaction between adjacent chains for effective stress transfer and to prevent slippage.

However, the requirement of ultra high molecular weight polymers imposes some challenges in processing. Above a certain molecular weight polymer chains tend to entangle, resulting in the zero shear viscosity to scale with $M^{3.4}$ where M is the molecular weight. The number of topological constraints increase with increasing molar mass and pose limitations on the required draw ratios for adequate chain alignment²³. To enable large scale deformation in polyethylene the entanglements can be diminished or even removed by spinning from diluted solutions to achieve enhanced stiffness^{14,24-26}. The weak secondary van der Waals interactions in polyethylene cannot circumvent chain slippage (creep) under constant stress.

1.3 Hydrogen bonding in polyamides; enhanced secondary interactions

Due to complications in the processing of ultra high molecular weight polyethylene (UHMWPE) and its low melting temperature stronger secondary interactions in flexible polymers have been of interest, for example hydrogen bonding that arises in polyamides. Stronger secondary interactions may facilitate the use of polymers of relatively low molar mass, having fewer entanglements per polymer chain and hence lower zero shear viscosities. Besides, hydrogen bonding provides an opportunity to overcome creep and better thermal stability.

Polyamides (PA) comprise well defined aliphatic sequences that are connected via regularly distributed amide groups. Since the nitrogen atom is electronegative, the NH proton is electron deficient in nature and tends to interact intimately with free electrons that can be donated by the electron rich oxygen atom of a carbonyl of another amide moiety. This electron exchange results in the fact that the amide motif serves both as hydrogen bonding donor and acceptor. During crystallization hydrogen bonded sheets of regularly

folded chains are formed that stack into 3D crystals where the secondary interactions between the hydrogen bonded sheets are secondary van der Waals forces²⁷⁻²⁹.

By varying the distribution of the amide moieties along the polymer backbone, the melting/crystallization temperature and the crystalline structure can be tailored. The higher the hydrogen bonding density, and hence the shorter the length of the aliphatic segments between the amide motifs, the higher is the melting temperature. For example melting temperature of PA46 and PA66 is around 295°C and 250-260°C, respectively. The way amide motifs are distributed along the polymer chain influences the crystal structure. Depending on the length and the distribution of the aliphatic blocks the hydrogen bonded sheets can be arranged either progressively or alternatively.

In some cases, for an example in PA46, both structures can be formed, maintaining linearly aligned hydrogen bonds³⁰. In the case of PA66, alternating as well as progressive hydrogen bonded sheets can be formed^{31,32}. PA46 and PA66 are even-even polyamides(PAxy), viz. condensation products of diamines and diacids or diacyl chlorides respectively. PA 6 is an even polyamide (PAx) that is synthesized from only one difunctional monomer, caprolactam. As polymers tend to crystallize in a chain folded way,

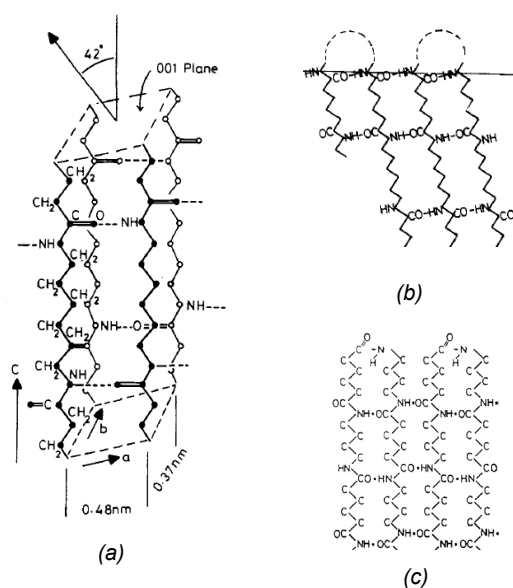


Figure 1.2: The triclinic unit cell of PA 6,6 in stick representation (a) with $a = 0.49 \text{ nm}$, $b = 0.54 \text{ nm}$, $c = 1.72 \text{ nm}$ and $\alpha = 45.8^\circ$, $\beta = 77^\circ$, $\gamma = 63.5^\circ$ (after Bunn and Garner^{30,31}). The interchain and intersheet distances are the projected distances between the polymer chains in the ac - (0.44 nm) and bc -plane (0.37 nm) respectively. In PA 66 folding of the methylene units and hydrogen bonding induce a progressive shear between adjacent chains and tilting of the chains (b). The incorporation of amide moieties in the folds of an alternating PA46 hydrogen bonding sheet (c), where the chains are positioned normal to the lamellar surface (from Atkins et al.³⁰)

because of a balance between kinetics and thermodynamics, the stem in a PA6 crystal can form hydrogen bonds with a neighboring stem if the chains organize in an alternating fashion³³⁻³⁶. Single crystal studies on PA66 have revealed a chain tilt by 42° with respect to the lamellar normal to optimize the hydrogen bonding interactions between the neighboring chains. However, when a symmetric distribution of the methylene units along the amide motifs exists, for example in PA46, maximum hydrogen bonding strength can be achieved in the alternating stacks without chain tilt³⁰. In the case of PA46 optimum hydrogen bonding efficiency is realized by an adjacent re-entry sharp fold similar to the β -turn in proteins. The sharp fold entails the presence of unsaturated hydrogen bonding amide moieties at the fold plane, promoting the water absorption. The hydrogen bonded sheets stack by van der Waals forces, in an either alternating or progressive shear of adjacent sheets. In a unit cell of polyamide crystals, for example the one of PA66 depicted in figure 1.2, the distance between neighboring chains in the hydrogen bonded sheet and the distance between the hydrogen bonded sheets, where van der Waals forces dominate, are referred to the interchain/intrasheet and interchain/intersheet distances respectively.

The development of extended chain polyamide crystals however faces an additional processing problem. In general flexible polymers are oriented/drawn at temperatures close to the melting temperature T_m , which is expressed as:

$$T_m = \Delta H / \Delta S \quad (1.2)$$

If the orientation/drawing temperature is much higher than the melting temperature, the polymer chains will relax and molecular orientation will be lost. On the other hand, if the orientation/drawing temperature is just above the melting temperature, the decrease in entropy S on stretching the chain will increase the melting temperature promoting the formation of lamellar crystals at the drawing temperature. Unlike, in polyethylene where the secondary interactions (van der Waals forces) between adjacent stems is smaller than the covalent bond energy along the main chain, the energy required to disrupt the hydrogen bonds that reside between the chains is close to the dissociation energy of a covalent carbon-carbon bond³⁷. The essence of the hydrogen bonding hurdle is not the energy of a hydrogen bond, but the cooperative strength of an ensemble of hydrogen bonds that are heavily directional and placed in a regular close-spaced sequence. The weak van der Waals interactions enable the formation of extended chain crystals by pulling out of chains from the lamellar crystals of polyethylenes, whereas the strong secondary interactions in polyamides do not allow formation of the extended chain crystals in the same way.

Thus temporarily shielding of the hydrogen bonding moieties by extra components will suppress crystallization and facilitate large scale deformation of polyamides. To benefit from the secondary interactions restitution of hydrogen bonding by efficient removal of the shielding agents in the oriented polyamides is desired. In the past several attempts in achieving drawability and extended chain polyamide crystals were based on the

use of reversible interactions of plasticizers comprising, ammonia^{38,39}, iodine^{40,41}, inorganic salts in melt spinning⁴²⁻⁴⁵, Lewis acid-base complexes, e.g. GaCl₃⁴⁶ and polar aprotic solvents, all with limited success especially in the efficient removal of the shielding agents.

1.4 Hydrogen bonding in silk; inspiration by natural silk spinning

Despite the scientific efforts mentioned above, nature shows exquisite examples of spun polypeptides, where prior to spinning the hydrogen bonding is shielded. Polypeptides or proteins can be considered as a decorated polyamide 2. Nature produces peptides in the ribosomes, translating the mRNA into complex polymers consisting of 20 monomeric amino acids with full control over molar mass, polydispersity, amino acid sequences, rendering the desired structure or conformation to fulfill the specific tasks. If the decoration, i.e. the R groups of the amino acids, comprises sufficiently small groups, such as protons or methyl groups in the case of alanine and glycine, parallel and anti-parallel hydrogen bonded β -sheets can be formed that stack to form crystals analogous to polyamide crystals^{47,48}.

Silks are a class of materials in nature where the role of such hydrogen bonded crystals, consisting of stacked β sheets (Figure 1.3), is clearly expressed⁴⁸⁻⁵⁰. Spiders as well as silkworms produce polypeptides with regularly distributed alanine and glycine or solely alanine sequences incorporated in a highly elastic peptide chain. Folding in silk peptides is favored by thermodynamic reasons. The energetic penalty for folding is compensated by

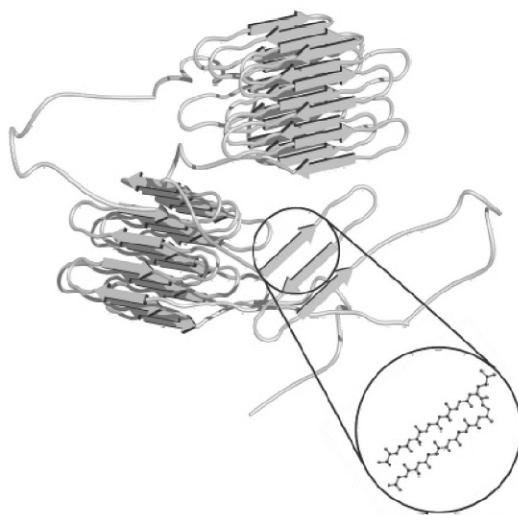


Figure 1.3: Self organization of a silk peptide chain into hydrogen bonded β sheets that stack by van der Waals forces, forming 3D crystals (copied from Van Hest and Tirrel⁴⁸)

interchain/intrasheet amide-amide hydrogen bonding. Due to the high hydrogen bonding density in peptides the “lamellar” spacing is only 2-3 nm in length. Spiders have several glands producing different proteins or protein blends, rendering silk fibers with different functionalities and unique mechanical properties⁵¹. In the major ampullate gland alanine rich fibroins are synthesized to meet the high stiffness, strength and toughness required for the dragline and web frame. The exceptional toughness, especially in case of the sticky viscid silk, shows strain-rate dependence, coping with static loads if the spider falls along its dragline or for the dynamic impact in viscid silk for prey capture. Reported E-moduli range between 10 to 50 GPa, elongation to breaks between 10 to 30% and tensile strengths between 1.0 and 1.4 GPa⁴⁸. However, the properties change at relatively high humidity where water molecules plasticize the amorphous component and saturate or hydrate the amide moieties of the amorphous phase, which under “dry” conditions contribute to the unique mechanical performance⁵².

Neglecting the dimensional aspects the crystalline domains in silk, either from spiders or worms, closely resemble chain folded crystals in synthetic polyamides, particularly in the PAX family. However, while solution spinning of synthetic polyamides has no industrial relevance due to the lack in controlling hydrogen bonding, spiders spin from aqueous peptide solutions mediating the hydrogen bonding at ambient temperature and pressure. It was reported that prior to spinning water molecules, ionic interactions and pH in the gland inhibit and template interchain hydrogen bonding⁵³⁻⁵⁶. During the spinning process variations in the type of ions, the ionic strength, the water content and pH determine the structure development in the silk dope, e.g. liquid crystallinity, and in the different fibroins that eventually results in the unique combination or properties.

1.5 Dissolution of polyamides in the superheated state of water

Recently, it has been shown in our group that water in its superheated state can be a good solvent for a range of synthetic aliphatic polyamides. These findings offer the possibility to use superheated water as a medium to transport ions to cap the hydrogen bonding moieties. Here, I recall the salient features of synthetic polyamides that are of relevance for the studies performed in this thesis.

The thermally induced Brill transition in aliphatic polyamides, commonly known as nylons, is a solid-state transformation from mainly a monoclinic or triclinic structure into a pseudo-hexagonal packing^{27-29,57-59}. The transition arises due to the tendency of thermally introduced gauche conformers to migrate from the lattice, which consists of stacked hydrogen bonded sheets having van der Waals secondary interactions⁶⁰⁻⁶². The migration entails a crankshaft type motion along the *c*-axis, where the rotational motion originates in a growing population of gauche conformers. The crankshaft type of motion initiates the out-of-plane wagging vibrations of the amide motifs. With increase in the interchain/

intersheet distance with temperature weakening of the van der Waals forces causes, the either progressive or alternative shear between the hydrogen bonded sheets. Despite the relatively high out-of-plane wagging vibrations caused by the migration of gauche conformers from the lattice, the retention of electron exchange between the hydrogen bonded moieties combined with the motion along the *c*-axis decreases the interchain/intrasheet distance⁶². The temperature where the interchain/intersheet and interchain/intrasheet distances merge, as depicted in wide angle X-ray diffraction, is referred to as the Brill transition temperature⁶³.

At elevated pressures and temperatures, close to the Brill transition, polyamides can be dissolved in the superheated state of water⁶⁴⁻⁶⁶. Here the perturbation of the hydrogen bonding interactions and especially weakening of the van der Waals forces between water molecules entails an enhanced diffusivity of water molecules⁶⁷. At these high temperatures the hydrogen bonding efficiency between amide moieties in adjacent crystal stems of the polyamide also decreases. In spite of the reduction in hydrogen bonding efficiency, the water and amide protons, which similar to any hydrogen bonded proton in electron deficiency, still tend to interact with free electrons present in the carbonyl moieties and the water molecules. Consequently the dynamic electron exchange between mobile water molecules and amide motifs perturbs the interchain/intrasheet hydrogen bonding, resulting in the dissolution of polyamides in the superheated state of water^{64-66,68}, i.e. water behaves as a good solvent for polyamides. Upon cooling crystallization occurs above the boiling point of water, where the continuous electron exchange between the water molecules and amide motifs leads to the entrapment of water molecules within the crystal lattice^{65,66,69-71}.

1.6 Objective of the thesis

In the past several attempts have been made to shield the hydrogen bonding in nylons temporarily. One of the main driving forces to perform such studies has been to obtain oriented and extended chain crystals, rendering high modulus, high strength polyamides. However, in spite of successful shielding of the amide motifs, removal of the shielding agents from the hydrogen bonding motifs has not been successful. Dissolution of polyamides in the superheated state of water, possibly facilitating transportation of ions to the amide moieties, opens an unexplored possibility for chain orientation and extended chain crystals, even at room temperature.

The aim of the thesis is to generate a fundamental understanding on shielding and mediating hydrogen bonding in (poly)amide crystallization from the superheated state of water. Based on the dissolution process of polyamides in the superheated state of water⁶⁴⁻⁶⁶ and inspired by natural silk spinning using a series of Hofmeister ions⁶⁷, explained in figure 1.4, a novel route for shielding and de-shielding hydrogen bonding in the development of high modulus polyamides is introduced.

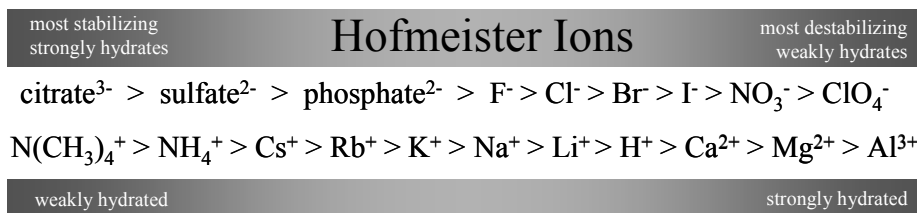


Figure 1.4: The Hofmeister classification of ions. Chaotropic or weakly hydrating ions disrupt the organization of water molecules, while kosmotropic or strongly hydrating ions promote the organization of water molecules. Dependent of the type of ions peptides can be solubilized in (salting-in) or precipitated from aqueous media (salting-out)⁶⁷. In general the precipitation of peptides from aqueous solutions is promoted by a mixture of kosmotropic anions and chaotropic cations.

1.7 Outline of the thesis

Since the amorphous component in semicrystalline polyamides poses experimental challenges in investigating the location and role of water molecules on crystalline hydrogen bonding efficiencies, low molecular weight amide model components are discussed in the first part of the dissertation. Two bisamide-diol model molecules with high hydrogen bonding density and representing even-even polyamides of the polyamide 2y and 4y families have been investigated.

In chapter 2 the crystallization of N,N'-1,2-ethanediyl-bis(6-hydroxy-hexanamide), a model molecule that belongs to the class of bisamide-diols, from the melt and the superheated state of water is discussed extensively. Thermodynamic and structural changes, which are studied by differential scanning calorimetry (DSC), time-resolved wide angle X-ray scattering diffraction (WAXD) and optical microscopy, reveal the influence of superheated water on crystallography and phase transitions. Interpretation of the WAXD patterns is moreover assisted by ab initio powder diffraction indexing.

In order to address the conformational changes, the location of the water molecules and the hydrogen bonding geometries, polarized Fourier transform infrared (FTIR) spectroscopy on single crystals of EDHA and solid state ¹H and ¹³C nuclear magnetic resonance spectroscopy experiments are discussed in chapter 3. The findings presented in as well chapter 2 as chapter 3 have been supported by molecular dynamics simulations performed by Hess et al.⁷¹. Since the conclusions of the simulations are in close agreement with the experimental findings some conclusive simulation results are embedded in the concluding part of chapter 3.

Although EDHA serves purpose of a model compound in understanding of hydrogen bonding in polyamides, the polyamides generally consist of longer aliphatic building blocks, featuring lower hydrogen bonding densities. In chapter 4 the influence of hydrogen bonding densities, that is, the balance between polar and apolar moieties, on the

ability to host water molecules in the crystal lattice is investigated by increasing the length of the diamine segment using 1,4-diaminobutane. N,N'-1,4-butanediyl-bis(6-hydroxyhexanamide) crystallized either from the melt or from the superheated state of water is discussed from a thermodynamic, structural and conformational aspect using DSC, WAXD, optical microscopy, FTIR and solid state ^1H and ^{13}C NMR spectroscopy.

Initial crystallization experiments of the bisamide-diols in the presence of Hofmeister salts, covering cations and anions of kosmotropic and chaotropic origin, have triggered the exploration of kosmotropic cations and chaotropic anions to suppress and mediate hydrogen bonding in polyamide crystallization, chapter 5. Shielding and de-shielding processes of amide-amide hydrogen bonding are identified by various characterization techniques such as DSC, WAXD, FTIR and solid state ^1H and ^{13}C NMR spectroscopy, dichroic measurements and optical microscopy.

Based on successful shielding and de-shielding experiments, as discussed in chapter 5, a technology assessment of the concept is presented by extruding polyamide 46 monofilaments from the melt and the superheated state of water. Drawability, structure development and mechanical properties of the PA46 filaments, in the presence of kosmotropic cations and/or chaotropic anions, are revealed by DSC, dynamic mechanical thermal analyses (DMTA), ^7Li NMR and FTIR spectroscopy, WAXD and tensile testing.

1.8 References

1. Flory, P. J. *Principles of Polymer Chemistry*, Cornell University Press, Ithaca, New York, **1953**.
2. Storks, K. H. *J. Am. Chem. Soc.* **1938**, 60, 1753.
3. Till, P. H. *J. Polym. Sci.* **1957**, 24, 301.
4. Keller, A. *Phil. Mag.* **1957**, 2, 1171.
5. Fischer, E. W. *Naturforsch.* **1957**, 12a, 753.
6. Bassett, D.C.; Frank, F.C.; Keller, A. *Nature* **1959**, 184, 810-811.
7. Keller, A. *In Growth and Perfection of Crystals*, John Wiley and Sons Inc., New York, **1948**, 499-528.
8. Abo el Maaty, M. I.; Hosier, I. L.; Bassett, D. C. *Macromolecules* **1998**, 31, 153-157.
9. Bassett, D.C.; Hodge, A.M. *Proc. R. Soc. Lond. A* **1978**, 359, 121-132.
10. Mandelkern, L. *In Crystallization of Polymers, 2nd edition, vol.2 Kinetics and Mechanisms*, Cambridge University Press **2004**.
11. Wittmann, J. C. ; Lotz, B. *J. Polym. Sci. Polym. Phys. Edn.* **1985**, 23, 205-226.
12. Lotz, B.; Cheng, S.Z.D. *Polymer* **2005**, 46, 577-610.
13. He, Y.; Wu, T.; Wei, J.; Fan, Z.; Li, S. *J. Pol. Sci. B. Pol. Phys.* **2008**, 46, 959-970.
14. Smith, P.; Lemstra P. J. *J. Mater. Sci.* **1980**, 15, 505-514.
15. Treloar, L. R. G. *Polymer* **1960**, 1, 95-103.

-
16. Barham, P. J.; Keller, A. *J. Pol. Sci. Lett.* **1962**, 17, 591.
 17. Clements, J.; Jakeways, R.; Ward, I. M. *Polymer* **1978**, 19, 639.
 18. Strobl, G. R.; Eckel, R. *J. Pol. Sci.* **1976**, 14, 913.
 19. Hong, S. Y.; Kertesz, M. *Phys. Rev. B.* **1990**, 41, 368.
 20. Suhai, S. *J. Pol. Sci. Phys.* **1983**, 21, 1341.
 21. Tashiro, K.; Kobayashi, M.; Tadokoro, H. *Macromolecules* **1978**, 11, 914.
 22. Termonia, Y.; Meaking, P.; Smith, P. *Macromolecules* **1985**, 18, 2246-2252.
 23. Smith, P.; Lemstra, P. J.; Booiij, H. C. *J. Polym. Sci., Polym. Phys. Edn.* **1981**, 19, 877-888.
 24. Smith P.; Lemstra, P. J.; Kalb, B.; Pennings, A. J. *Polym. Bull.* **1979**, 1, 733-736.
 25. Smith, P.; Matheson, Jr., R. R. and Irvine, P. A. *Polym. Commun.* **1984**, 25, 294.
 26. Smook, J.; Pennings, A. J. *Polym. Bull.* **1983**, 10, 291-297.
 27. Jones, N. A.; Atkins, E. D. T.; Hill, M. J.; Cooper, S. J.; Franco, L. *Macromolecules* **1996**, 29, 6011-6018.
 28. Jones, N. A.; Atkins, E. D. T.; Hill, M. J.; Cooper, S. J.; Franco, L. *Polymer* **1997**, 38, 2689-2699.
 29. Jones, N. A.; Atkins, E. D. T.; Hill, M. J.; Cooper, S. J.; Franco, L. *Macromolecules* **1997**, 30, 3569-3578.
 30. Atkins, E. D. T.; Hill, M. J.; Hong, S. K.; Keller, A.; Organ, S. *Macromolecules* **1992**, 25, 821-837.
 31. Bunn, C. W.; Garner, E. V. *Proc. Roy. Soc.* **1947**, A189, 39-68.
 32. Jones, N. A.; Atkins, E. D. T.; Hill, M. J. *J. Pol. Sci. B, Pol. Phys.* **2000**, 38, 1209-1221.
 33. Parker, J. P.; Lindenmeyer, P. H. *J. Appl. Pol. Sci.* **1977**, 21, 821-837.
 34. Cooper, S. J.; Atkins, E. D. T.; Hill, M. J. *Macromolecules* **1998**, 31, 5032-5042.
 35. Atkins, E. D. T.; Hill, M. J.; Jones, N. A.; Sikorski, P. *J. Mat. Sci.* **2000**, 35, 5179-5186.
 36. Li, Y.; Goddard III, W. A. *Macromolecules* **2002**, 35, 8440-8455.
 37. Postema, A. R.; Smith, P.; English A. D. *Polym. Comm.* **1990**, 31, 444-447.
 38. Zachariades, A. E.; Porter R. S. *J. Appl. Pol. Sci.* **1979**, 24, 1371-1382.
 39. Kanamoto, T.; Zachariades, A. E.; Porter, R. S. *J. Appl. Polym. Sci. Polym. Phys. Edn.* **1982**, 20, 1485-1496.
 40. Chuah, H. H.; Porter, R. S. *Polymer* **1986**, 27, 1022-1029.
 41. Lee, Y. H.; Porter, R. S. *J. Macromol., Sci., Phys. B* **1995**, 34, 295-309.
 42. Acierno, D.; Bianchi, E.; Ciferri, A.; Cindio, B.; Migliaresi, C.; Nicolais, L. *J. Polym. Sci. Polym. Symp.* **1976**, 54, 259-269.
 43. Acierno, D.; Lamantia, F. P.; Polizzotti, G.; Ciferri, A. *J. Polym. Sci. Polym. Phys. Edn.* **1979**, 17, 1903-1912.
 44. Ciferri, A.; Acierno, D.; Alfonso, G. C. *Patent US4167619* **1979**.
 45. Richardson, A.; Ward, I. M. *J. Polym. Sci., Polym., Phys. Edn.* **1981**, 19, 1549-1565.
 46. Vasanthan, N.; Kotek, R.; Jung, D. W.; Shin, D.; Tonelli, A. E.; Salem, D. R. *Polymer* **2004**, 45, 4077-4085.

-
47. Levitte M.; Chotia, C. *Nature* **1976**, 261, 552-558.
 48. Van Hest, J. C. M.; Tirrell, D. *Chem. Comm.* **2001**, 1897-1904.
 49. Viney, C. *Supramol. Sci. A* **1997**, 75-81.
 50. Matsumoto, A.; Chen, J.; Collette, A. D.; Kim, U. J.; Altman, G. H.; Cebe, P.; Kaplan, D. L. *J. Phys. Chem. B* **2006**, 110, 21630-21638.
 51. Gosline, J. M.; Guerette, P. A.; Ortlepp, C. S.; Savage, K. N. *J. Exp. Biol.* **1999**, 202, 3295-3303.
 52. Gosline, J. M.; Denny, M.; DeMont, M. E. *Nature* **1984**, 309, 551-552.
 53. Dicko, C.; Vollrath, F.; Kennedy, J. M. *Biomacromolecules* **2004**, 5, 704-710.
 54. Zhou, L.; Chen, X.; Shao, Z.; Huang, Y.; Knight, D. P. *J. Phys. Chem. B.*, **2005**, 109, 16937-16945.
 55. Holland, C.; Terry, A. E.; Porter, D.; Vollrath, F. *Nature Mat.* **2006**, 5, 870-874.
 56. Wong Po Foo, C.; Bini, E.; Hensman, J.; Knight, D. P.; Lewis, R. V.; Kaplan, D. L. *Appl. Phys. A* **2006**, 82, 223-233.
 57. Jones, N. A.; Cooper, S. J.; Atkins, E. D. T.; Hill, M. J.; Franco, L. *J. Pol. Sci. B, Pol. Phys.* **1997**, 35, 675-688.
 58. Yoshioka, Y.; Tashiro, K. *Polymer* **2003**, 44, 7007-7019.
 59. Nair, S. S.; Ramesh, C.; Tashiro, K. *Macromolecules* **2006**, 39, 2841-2848.
 60. Yoshioka, Y.; Tashiro, K.; Ramesh, C. *Polymer* **2003**, 44, 6407-6417.
 61. Yoshioka, Y.; Tashiro, K. *J. Phys. Chem. B.* **2003**, 107, 11835-11842.
 62. Vinken, E.; Terry, A. E.; Hoffmann, S.; Vanhaecht, B.; Koning, C. E.; Rastogi, S. *Macromolecules* **2006**, 39, 2546-2552.
 63. Brill, R. *J. Prakt. Chem.* **1942**, 161, 49-64.
 64. Rastogi, S.; Terry, A. E.; Vinken, E. *Macromolecules* **2004**, 37, 8825-8828.
 65. Vinken, E.; Terry, A. E.; Van Asselen, O.; Spoelstra A. B.; Graf, R.; Rastogi, S. *Langmuir* **2008**, 24, 6313-6326.
 66. Vinken, E., PhD Thesis, Eindhoven University of Technology *Polyamides: Hydrogen bonding, the Brill transition, and superheated water* **2008**.
 67. Dill, K. A.; Truskett, T. M.; Vlachy, V.; Hribar-Lee, B. *Annu. Rev. Biophys. Biomol. Struct.* **2005**, 34, 173-199.
 68. Challa, G. *Plastica* **1969**, 22, 204-208
 69. Harings, J. A. W.; Van Asselen, O.; Graf, R.; Broos, R.; Rastogi, S. *Cryst. Growth Des.* **2008**, 8, 2469-2477.
 70. Harings, J. A. W.; Van Asselen, O.; Graf, R.; Broos, R.; Rastogi, S. *Cryst. Growth Des.* **2008**, 8, 3323-3334.
 71. Hess, B.; Harings, J. A. W.; Rastogi, S.; Van der Vegt, N. F. A. *J. Phys. Chem. B.* **2009**, 13, 627-631.

Chapter 2*

The role of superheated water on the crystallization of N,N'-1,2-ethanediyl-bis(6-hydroxy-hexanamide); implications on crystallography and phase transitions

A symmetrical, hydrogen bonded low molecular weight molecule N,N'-1,2-ethanediyl-bis(6-hydroxy-hexanamide), crystallized from melt or from the superheated state of water, is examined. Thermodynamic and structural changes during phase transitions are followed by DSC, time-resolved X-ray techniques and polarized optical microscopy. Considering the hydrogen bonding motifs present in this bisamide-diol, it is selected as a model compound for crystalline domains present in semicrystalline 2y polyamides. By studying this model compound it was moreover aimed to elucidate the specific role of water molecules that are likely to reside in the crystals obtained from the superheated state of water. On heating the melt crystallized sample, the observed crystalline transitions are not the same as observed in polyamides. However, similar to polyamides the origin of the transition is due to the electron exchange between the hydrogen bonding moieties and conformational changes in the aliphatic sequences. At low temperatures (below 22°C) non-trans conformations in the central diamine methylene moieties induce a different triclinic structure, having unit cell parameters close to monoclinic, with potential existence of interchain/intersheet hydrogen bonding. Crystallization from superheated water entails remarkable differences in the physical behavior. A metastable crystalline structure, obtained from the superheated state of water and possessing relatively large interchain/ intrasheet and interchain/intersheet distances, transforms into another hydrogen bonded crystal via sequential temperature cycles. When compared with the melt crystallized sample the crystal obtained after sequential temperature cycles show considerable difference in the crystal-to-crystal phase transition while melting remains the same. In combination with the increased crystal-to-crystal transition temperature, an expansion along the c-axis suggests a stabilizing effect of rigid hydroxylic protons that contribute to the unit cell parameters.

* Partially reproduced from Harings, J.A.W.; Van Asselen, O.; Graf, R.; Broos, R.; Rastogi, S. *Cryst. Growth Des.* **2008**, 8, 2469-2477

2.1 Introduction

Hydrogen bonds are a member of cooperative non-covalent interactions that contribute to spontaneous organization of molecules into higher order structures. Hydrogen bonding arises because of very strong dipole-dipole attraction between protons that are bonded to small, highly electronegative atoms, such as O, N or F, with free electron pairs present on other similar electronegative atoms¹. This unique phenomenon results in the accumulation of the electron density between the electron donor and acceptor. The presence of lone pairs of electrons or polarizable π electrons enables the partially unshielded proton (the electron deficient atom) to fulfill its continuous quest for electrons². In terms of self-assembly, boundary conditions such as temperature, pH, ionic strength and polarity induced interactions influence specific molecular motifs, e.g. hydrogen bonded moieties, and trigger the formation of myriads of meso- and macroscopic architectures.

Nature provides numerous exquisite structures where hydrogen bonding plays a crucial role, for example, DNA, which consists of two polynucleotide chains that form a right-handed double helix by specifically directed hydrogen bonds between complementary base pairs. Nevertheless, hydrogen bonding offers specific features in synthetic polymers as well. To quote, a familiar class of synthetic polymers that benefit from hydrogen bonded moieties belongs to the polyamide family. There are also recent examples where the very existence of polymers relies on a self-complementary array of cooperative hydrogen bonded building blocks that associate into well-defined reversible supramolecular structures^{3,4}.

Recently, the feasibility to dissolve hydrogen bonded polymers, from synthetic as well as natural origin, in superheated water was reported^{5,6}. The breakdown of the space filling percolating hydrogen bonded network, such as the tetrahedral arrangement of the nearest neighbor water molecules, disappears under these conditions, which are well below the supercritical point of water. Highly favorable interactions between the polymer and water, which result in a highly negative interaction parameter, enables water molecules to penetrate the crystallites, resulting in dissolution of the polymer⁷. Water molecules, which have become relatively mobile, tend to form different kinds of hydrogen bonded clusters⁸. On crystallization of the hydrogen bonded polymer, such as polyamide 4,6 from aqueous solution, water molecules seem to reside within the lattice forming clathrates⁹. However, the presence of an amorphous component in the investigated polyamides limits our fundamental understanding on the role of water molecules on hydrogen bonding within the crystalline lattice. To circumvent this problem, in this chapter a symmetrical, hydrogen bonded low molecular weight molecule N,N'-1,2-ethanediyl-bis(6-hydroxy-hexanamide) is proposed that might act as a model system, representing the crystalline domains of 2y polyamides (Figure 2.1). This molecule belongs to a class of bisamide-diols that was incorporated in aliphatic polyesters to introduce crystallizable segments, improving the thermal and mechanical behavior^{10,11}.

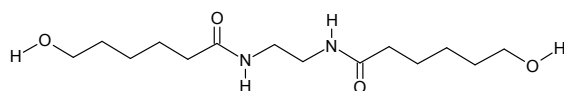


Figure 2.1: Chemical structure of *N,N'*-1,2-ethanediyl-bis(6-hydroxy-hexanamide).

To recall: in aliphatic polyamides sheets are formed by regularly folded chains that are strengthened by hydrogen bonds between the amide moieties of adjacent chains. Within the crystal the hydrogen bonded sheets are held together by van der Waals forces, either by a progressive (α) or alternating shear (β) arrangement¹²⁻¹⁵. Upon heating most polyamides undergo a solid-state crystal transition from either a monoclinic or triclinic to a pseudo-hexagonal phase, known as the Brill transition¹⁶. During the transition the typical interchain/intrasheet distance, corresponding to the 100 diffraction signal, and the interchain/intersheet distance, given by the 010/110 diffraction signal, merge into a single diffraction signal. Dimensional changes taking place in the hydrogen bonded network during the Brill transition are still a matter of debate. Detailed studies performed by Tashiro and co-workers highlight the origin of the Brill transition. To summarize, the introduction of gauche conformers at elevated temperatures entails disorder in the methylene sequences between hydrogen bonded motifs, and as such weaken the cooperative strength of the two-dimensional hydrogen bonded network¹⁷⁻¹⁹. These findings are further strengthened by studies performed on piperazine based comonomers, which solely act as hydrogen bonded acceptor²⁰⁻²². The tendency of gauche conformers to migrate from the lattice induces chain mobility along the *c*-axis, which is followed by twisting in the methylene segments next to the amide moieties that with retaining hydrogen bonding in the sheets eventually results in contraction in the 100 interchain/intrasheet distance.

Since the amide moieties in *N,N'*-1,2-ethanediyl-bis(6-hydroxy-hexanamide) are incorporated in a head-to-head fashion (similar to polyamide 4,6), these bisamide-diols are likely to form hydrogen bonded sheet structures by self-assembling processes similar to polyamides^{10,11}. Combining differential scanning calorimetry with optical microscopy and time-resolved WAXD it is aimed to investigate thermodynamic and structural changes in these bisamide-diols when crystallized from melt and/or superheated water. As stated above, these bisamide-diols are potential model systems for the crystalline domains in polyamides due to the absence of the amorphous regions.

2.2 Experimental section

2.2.1 Materials

1,2-Diaminoethane and ϵ -caprolactone were purchased from Aldrich, The Netherlands. Tetrahydrofuran (THF) and acetonitrile, both of analytical grade, were obtained from Biosolve, The Netherlands. N,N' -1,2-ethanediyl-bis(6-hydroxyhexanamide), from now on denoted as EDHA and sketched in Figure 2.1, was synthesized using a modified procedure of Katayama (Figure 2.2)²³. A solution of ϵ -caprolactone (0.17mol) in 25 mL of THF was added in 2 hours to a solution of 1,2-diaminoethane (0.087mol) in 50 mL THF. Subsequently, the mixture was stirred at 10°C for 40 hours. After THF was removed under reduced pressure, the precipitate was purified by successive recrystallization in an acetonitril/ water (7/1, v/v) solution at 5°C. Thermodynamic, structural and morphological aspects of melt and water crystallized EDHA were studied. Melt crystallized samples were obtained by cooling from melt at 10°C/min to 5°C. In a closed environment a part of the melt crystallized sample was dissolved in water at 90°C, disrupting the percolating hydrogen bonded network of water partially. Upon cooling the aqueous solution, at a rate of 10°C/min, the dissolved bisamide-diol crystallizes.

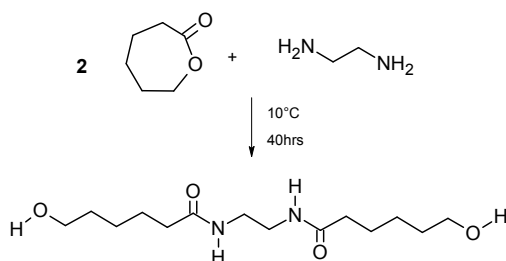


Figure 2.2: Synthesis of N,N' -1,2-ethanediyl-bis(6-hydroxy-hexanamide)

2.2.2 Differential scanning calorimetry

Thermodynamic behavior of the melt and the water crystallized EDHA (10°C/min) was studied under nitrogen atmosphere by DSC using a TA Q1000 apparatus. In order to study the phase transitions accurately, the crystals were exposed to two initial heating and cooling profiles from -25 up to 125°C, followed by two cycles from -25 up to 175°C. The heating and cooling rate of all cycles was 10°C/min and 3 min of isothermal conditions was applied at the temperature limits.

2.2.3 Wide angle X- ray diffraction

Wide angle X- ray diffraction experiments were performed at the high resolution Materials Science beamline ID11, located at the European Synchrotron Radiation Facility (ESRF), Grenoble, France. A synchrotron source was desired to investigate in situ the dissolution and recrystallization of hydrogen bonded (macro) molecules in the superheated state of water, a topic that is not specifically addressed here but covers a significant part of our research. Moreover, time-resolved measurements allowed us to investigate the structural changes within an experimental time scale identical to the DSC measurements. Two-dimensional diffraction patterns were recorded using a Frelon 2D detector having 2048 * 2048 arrays of pixels with a pixel size of 46.8 * 48.1 μm , providing the high resolution required for accurate determination of the peak positions.

Crystals grown from water were placed in a 1 mm diameter Lindemann capillary and exposed to two temperature cycles, from -25 up to 125°C and two cycles from -25 up to 175°C using a Linkam TMS94 hotstage at a heating/cooling rate of 10°C/min. During the last temperature cycles the water crystallized samples were exposed to temperatures above the melting temperature (157°C). DSC measurements revealed that melting erases the specific thermodynamic behavior of the EDHA crystals grown from the superheated state of water (Figure 2.6a). As a result, the crystallization process and successive phase transitions of the melt crystallized EDHA during the remaining temperature profile were monitored in situ. A 25 keV ($\lambda = 0.0496$ nm) X-ray beam of 50 μm size was used and a two-dimensional diffraction patterns of 0.5 s exposure time were collected at every 6 seconds. To calibrate the sample-to-detector distance a lanthanum hexaboride standard was used. After correction for the absorption and air scattering, all diffraction patterns were circumferentially integrated to give the intensity against the scattering vector q . The relation $d = 2\pi/q$ was used to convert the scattering into d -spacing. TREOR 90, a general trial-and-error method for the ab initio indexing of powder patterns, using a space group of P-1, in combination with a Pawley refinement was used to assign the observed diffraction signals and lattice parameters of the different unit cells^{24,25}.

2.2.4 Optical microscopy

Morphological and structural changes of water and melt crystallized EDHA were observed by optical microscopy using a Zeiss Axioplan Imaging 2. Single EDHA crystals were exposed to two temperature cycles from 5 to 125°C and one cycle from 5 to 175°C using a linkam TMS94 hotstage at 10°C/min. Making use of crossed polarizers and a retardation plate (λ) for red wavelength, optical images were taken at every 10°C.

2.3 Results and discussion

2.3.1 Phase transitions in EDHA

Figure 2.3 shows a typical DSC trace for melt crystallized EDHA. On heating from -25°C onward, three endothermic transitions are observed at 63, 85 and 157°C respectively. Considering the heat involved in the two transitions at 63°C and 85°C , the endothermic transitions can be attributed to phase transformations arising in the crystal lattice. The transition at 157°C , appears to originate in the melting of crystals. On cooling from 175°C , three exothermic peaks at 143, 80 and 22°C are observed. Considering the similar heat involved in the three transitions during the heating and cooling cycle, the transitions can be attributed to first order transitions. It is to be noted that the exothermic transition at 22°C requires larger supercooling ($\sim 41^{\circ}\text{C}$) compared to the exothermic transition at 80°C ($\sim 5^{\circ}\text{C}$). The lower supercooling required for the exothermic transition at 80°C suggests a lower entropic barrier in the phase transformation compared to the exothermic transition at 22°C . To reveal the crystallographic changes during these phase transformations, time-resolved X-ray diffraction studies have been performed.

Figure 2.4 shows a series of time-resolved X-ray diffraction patterns recorded on cooling EDHA from its melt. In accordance with the DSC trace as shown in Figure 2.3, liquid EDHA crystallizes at 143°C . Figures 2.4a-c represent the 2 dimensional WAXD patterns. Anisotropic distribution in intensity suggests the presence of some preferred orientation (textured crystals). The orientation in the in-situ melt grown crystals can be attributed to the external forces likely to arise from the substrate. Hence the arising anisotropic intensity profile cannot be attributed to the crystalline unit cell. Figure 2.4d

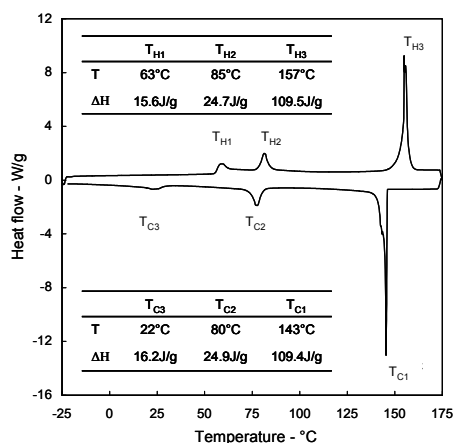


Figure 2.3: DSC thermogram of melt crystallized EDHA. The tables present the transition temperatures and the corresponding enthalpies.

shows a series of circumferentially integrated WAXD patterns along 2θ recorded on cooling. On recrystallization, at 143°C two intense diffraction signals at $d = 0.42$ and 0.41 nm, adjacent to each other in the 2θ range of 6.5 to 7.5° are observed. Together with these two signals, close to the beamstop a distinct diffraction signal at $d = 1.95$ nm ($2\theta = 1.46^\circ$) is observed. On cooling further to 85°C , the two adjacent diffraction signals tend to diverge, whereas the signal close to the beamstop shifts very slightly to 1.93 nm. The diffraction signal at 1.93 nm suggests a correlation with the length of the molecule, which is 2.03 nm in all-trans conformation. Together with the two intense diffraction signals ($d = 0.416$ and 0.407 nm at 125°C) two weak diffraction signals ($d = 0.449$ and 0.437 nm at 125°C) at lower angles are also observed. Similar to the intense signals the weak diffraction signals also tend to diverge on cooling. The changes occurring on cooling are depicted in Figure 2.4e. The divergence of the pairs of diffraction signals (intense and weak) resembles the crystallographic changes occurring in the 100 interchain/intrasheet and 010 interchain/ intersheet diffraction signals of polyamides on cooling below the Brill transition^{12-19,22}.

To assign the crystallographic packing of EDHA molecules, the TREOR 90 method in combination with a Pawley refinement is applied. A comparison of the observed and simulated diffraction signals at three representative temperatures is presented in Table 2.1 and illustrated in Figure 2.5 as well. Neglecting orientation, a good match between the observed and simulated diffraction patterns at 125°C is depicted, especially at small length scales. The method reveals a triclinic unit cell, with unit cell dimensions as shown in Table 2.2. Similar good matching is observed for all diffraction patterns between the onset of crystallization to 85°C . The corresponding indexed signals are shown in Figure 2.4a. Analogous to polyamides the interchain/intersheet distance decreases drastically as observed by the 100 diffraction signal, whereas the interchain/intrasheet spacing 010 hardly changes (Figure 2.4e). It is to be noted that in comparison to polyamide crystallography, in EDHA the interchain/intrasheet and interchain/intersheet spacings are inversely assigned. For various polyamides it has been reported that on cooling a diminishing population of gauche conformers induces less out of plane vibration of the amide motifs and as such strengthens hydrogen bonding and van der Waals interactions^{17-19,22}. Upon cooling progressive divergence of the 100 interchain/intersheet and 010 interchain/intrasheet diffraction signals, especially because of the van der Waals influenced 100 spacing that decreases progressively, is in accordance with the changes observed in polyamides on cooling below the Brill transition temperature.

Further cooling below 85°C , Figure 2.4d,e, results in a sudden change in the diffraction signals. This remarkable discontinuous change is likely to account for the phase transition as observed in DSC. With the transition, the projected length of the molecule along the c -axis, depicted by 001 diffraction signal, decreases from 1.93 (at 85°C) to 1.91 nm (at 75°C). Powder diffraction indexing (as calculated from the TREOR 90 method) shows an increase in the c value from 1.96 to 2.02 nm. This is rather consistent with the all-

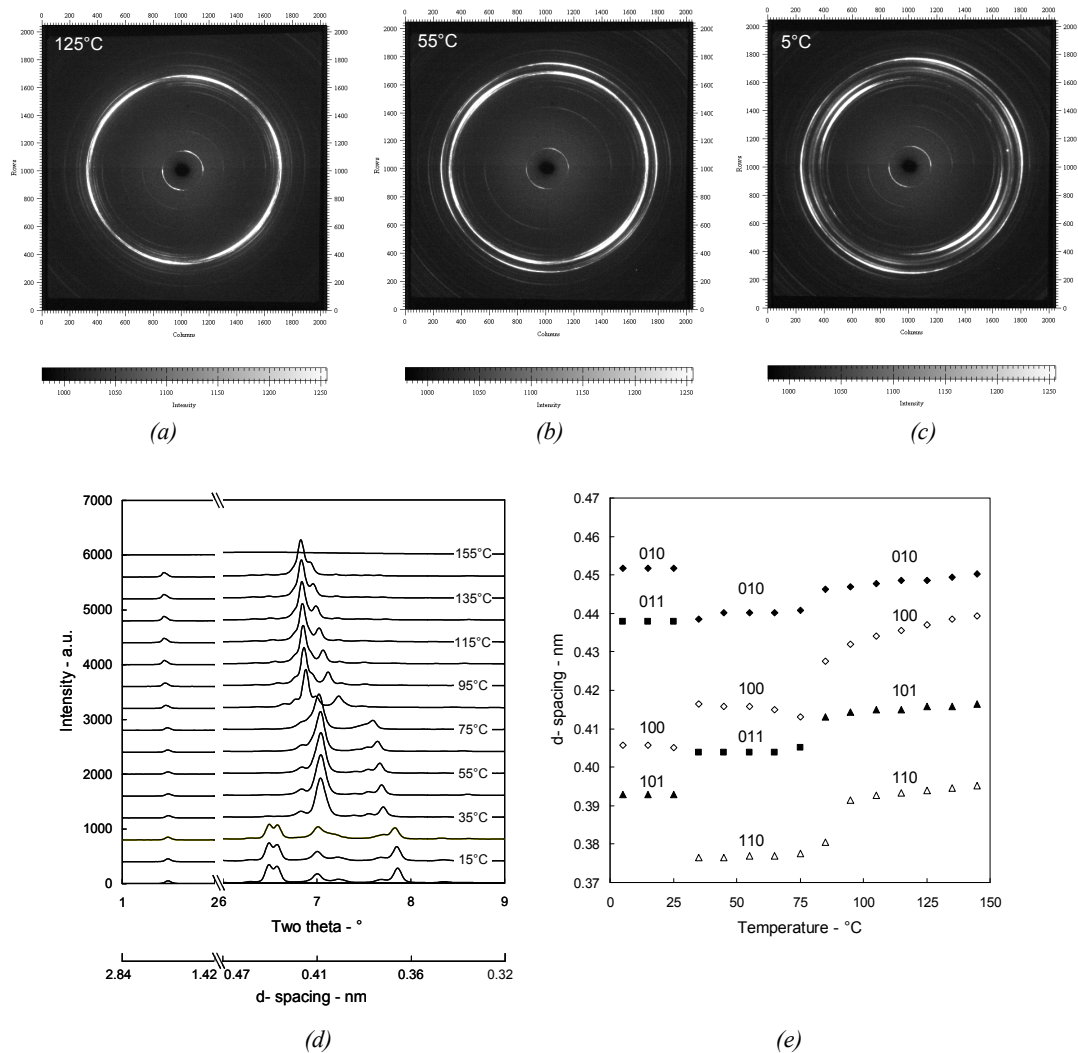


Figure 2.4: Structural changes by time-resolved WAXD ($\lambda = 0.0496$ nm) as EDHA was cooled from the melt at 10 °C/min. Diffraction images of textured crystals at representative temperatures, (a), (b) and (c). Since the observed orientation profiles are irrelevant in following the lattice parameters as a function of temperature, the WAXD images were integrated along the circumference. Analysis of the Bragg reflections as a function of temperature (d), resulted in the selection of representative diffraction patterns that were used for powder diffraction indexing to assign the interchain/intrasheet and interchain/intersheet diffraction signals. Variations of the interchain/intrasheet and interchain/intersheet spacings are followed as function of temperature, where the symbols \blacklozenge , \diamond , \blacktriangle , \triangle and \blacksquare represent the 010, 100, 101, 110 and 011 diffraction signals respectively (e).

trans conformation of the backbone (2.025 nm); taking the apparent length c as:

$$c = 0.125N - 0.02\delta - 0.03\varepsilon \quad (2.1)$$

where N is the number of backbone bonds (excluding the hydroxylic proton bonds), δ and ε are the number of nitrogen and oxygen atoms in the molecule respectively. Simultaneously, less defined boundaries along the c -axis are registered by a declining intensity of the 001 diffraction signals. With the continuous decrease in temperature gauche conformers are replaced by trans conformers and as a result the c -axis tends to increase. The decrease in the gauche conformers suppresses the rotational motion along the c -axis, which favors the establishment of more effective hydrogen bonding and van der Waals interactions.

Table 2.1: Powder diffraction indexing of melt crystallized EDHA on cooling at 5°C, 55°C and 125°C using the TREOR 90 method combined with a Pawley refinement ($\lambda = 0.0496$ nm)^{a)}

Bravais-Miller indices			Melt crystallized at 5°C			Melt crystallized at 55°C			Melt crystallized at 125°C		
h	k	l	$d_{obs.}$	$d_{sim.}$	Δ_d	$d_{obs.}$	$d_{sim.}$	Δ_d	$d_{obs.}$	$d_{sim.}$	Δ_d
			nm	nm	nm	nm	nm	nm	nm	nm	nm
0	0	1	1.910	1.910	0.000	1.886	1.886	0.000	1.933	1.933	0.000
0	0	2							0.967	0.967	0.000
0	0	3	0.629	0.637	-0.008	0.630	0.629	0.001	0.646	0.645	0.001
0	0	4	0.478	0.478	0.000	0.471	0.471	0.000	0.483	0.483	0.000
0	1	0	0.452	0.452	0.000	0.440	0.440	0.000	0.449	0.449	0.000
0	1	1	0.438	0.438	0.000	0.404	0.404	0.000			
0	1	2							0.407	0.406	0.001
0	1	3							0.368	0.368	0.000
0	-1	4	0.331	0.331	0.000				0.330	0.329	0.001
0	-1	5				0.340	0.338	0.002			
1	0	0	0.406	0.406	0.000	0.416	0.416	0.000	0.437	0.437	0.000
1	0	1	0.393	0.393	0.000				0.416	0.416	0.000
1	0	2							0.382	0.381	0.001
-1	0	1				0.384	0.383	0.001			
-1	0	3	0.370	0.370	0.000						
-1	0	4							0.346	0.345	0.001
1	1	0				0.377	0.377	0.000	0.394	0.394	0.000
1	1	1				0.371	0.371	0.000	0.378	0.378	0.000
1	1	2				0.352	0.352	0.000			
1	-1	1	0.362	0.361	0.001						
1	-1	2	0.340	0.341	-0.001						
-1	1	0	0.352	0.350	0.002						

^{a)} The observed diffraction signal, $d_{obs.}$, are assigned in Bravais-Miller indices and compared to the simulated diffraction signals, $d_{sim.}$. The difference is denoted as Δ_d .

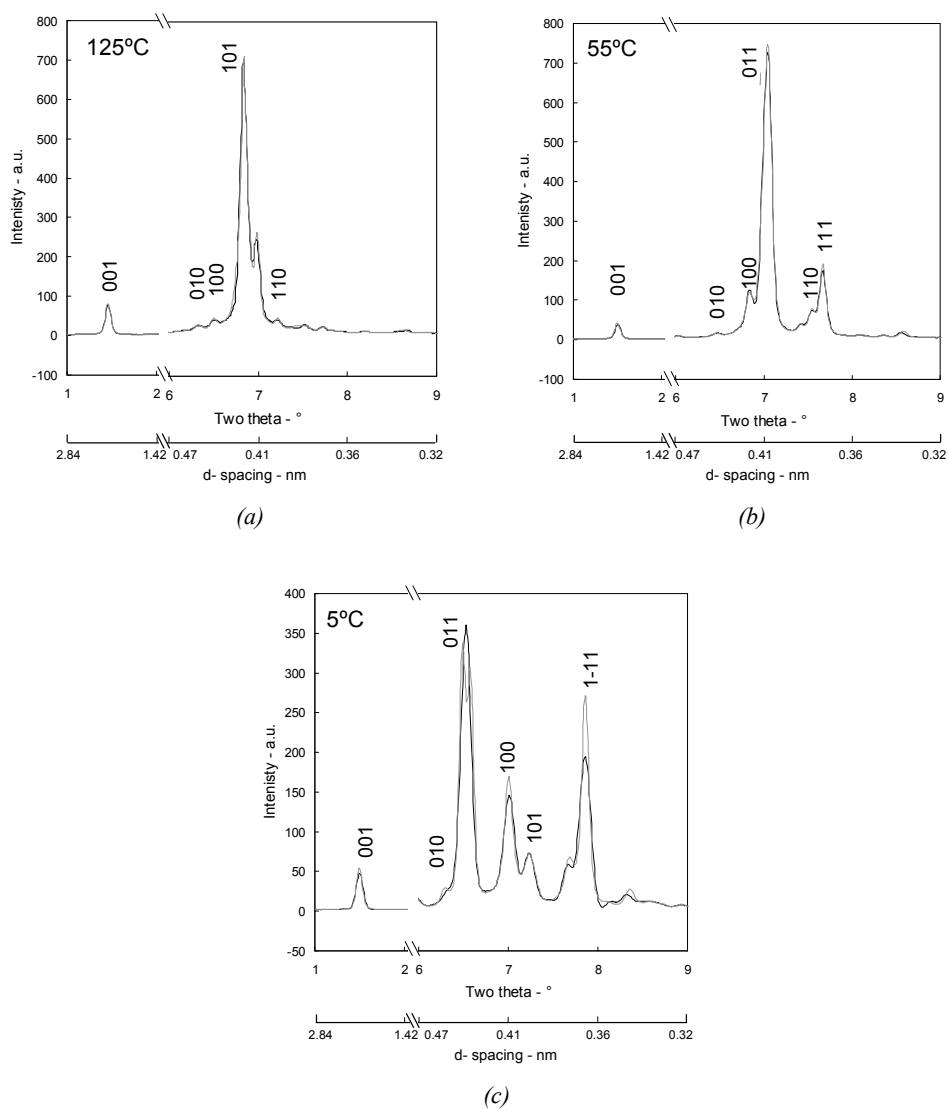


Figure 2.5: Experimental (grey) and TREOR 90 simulated (black) wide angle X-ray diffraction patterns at three different temperatures, a) 125, b) 55 and c) 5°C, as EDHA is cooled from the melt.

Table 2.1 shows a good match between the simulated X-ray diffraction pattern for the assigned triclinic phase with the experimental pattern recorded at 55°C. The assigned unit cell is shown in Table 2.2. The angle between the *b*- and *c*-axes, $\alpha = 102^\circ$, matches with linearly aligned hydrogen bonds within the sheets¹³. The conformational and structural parameters at 55°C offer the most efficient electron exchange between the amide moieties.

The established strong hydrogen bonding suppresses the out of plane wagging motion in the hydrogen bonded motifs enabling a denser packing of the hydrogen bonded sheets. This is observed as a decrease in the 100 interchain/intersheet distance to 0.416 nm. Though on transition, with the decrease in gauche conformers, the expansion of the c -axis occurs, strengthening of the secondary interactions involves a decrease in the unit cell volume from 0.414 to 0.396 nm³ at 125 and 55°C respectively.

On cooling further, below 55°C, after slight lattice contraction abrupt structural changes are observed at the third exothermic event T_{HI} as registered by DSC. On powder diffraction indexing of the X-ray diffraction pattern recorded at 5°C, the assigned triclinic unit cell shows a remarkable change in the angles between the axes. In a close approximation the assigned triclinic cell resembles to the monoclinic. Diffraction signals thus assigned are shown in Figure 2.4c. Considering the assigned signals, the observations are that while the 100 interchain/intersheet distance decreases from 0.416 to 0.406 nm, the 010 interchain/intrasheet distance increases from 0.440 to 0.452 nm (Figure 2.4). Although the projected length hardly changes, contraction of the c -axis from 2.02 to 1.91 nm occurs, suggesting deviation from the all-trans chain conformation. Regardless of the structural transformations, especially at low temperatures, it can be concluded that the secondary interactions within and between the hydrogen bonded sheets of EDHA show typical polyamide type of temperature dependence. A similar low temperature phase is also reported for the polyamide 2Y family by Jones et al.²⁶. A detailed study on the conformational changes arising with the phase transformations is revealed in chapter 3 and besides published as reference 27.

Recent studies on polyamides performed by us and others show that these polymers can be dissolved in the superheated state of water^{9,28,29}. Experimental evidence suggests the location of the water molecules within the lattice along with their presence in the amorphous phase⁹. These findings have implications in shielding of hydrogen bonding and thus influencing the crystal modulus. Due to the semicrystalline nature of polyamides the location of water molecules has been a matter of debate. The absence of amorphous regions in EDHA provides a unique opportunity to investigate the localization of water molecules and its implications on hydrogen bonding. What follows is a study on EDHA molecules crystallized from (superheated) water close to its boiling point.

Table 2.2: Diffraction signals and unit cell parameters of melt crystallized EDHA in three crystalline forms at three different temperatures T

T	structure	WAXD diffraction signals					unit cell parameters						
		010	100	101	011	110	a	b	c	α	β	γ	V
°C		nm	nm	nm	nm	nm	nm	nm	nm	°	°	°	nm ³
125	triclinic	0.449	0.437	0.416		0.394	0.475	0.483	1.96	93.2	98.3	68.2	0.414
55	triclinic	0.440	0.416		0.404	0.377	0.456	0.482	2.02	102	77.7	72.7	0.396
5	triclinic	0.452	0.406	0.393	0.438		0.432	0.478	1.91	90.4	92.4	110	0.372

2.3.2 Influence of water molecules on hydrogen bonding

When compared with the crystals grown from melt, EDHA crystals grown in aqueous environment exhibit considerable differences. Upon heating, unlike EDHA crystallized from the melt (Figure 2.3) where three endothermic transitions are observed, the water crystallized EDHA shows only two endothermic transitions. The two endothermic transitions are positioned at 95 and 157°C. Independent of the crystallization conditions, either from the melt or from the superheated state of water, the crystals melt at 157°C. In order to explore the origin of the endothermic transition of the water crystallized EDHA at 95°C (Figure 2.6a; first DSC trajectory), which differs distinctly from the two endothermic transitions in the melt crystallized samples below the melting point at 157°C (Figure 2.3), the crystals were exposed to two initial temperature cycles from -25 and 125°C prior to melting in a temperature cycle from -25 and 175°C (Figure 2.6a; third DSC trajectory). Cooling after the first heating run, first DSC trajectory shows two exothermic peaks at 83 and 59°C. On heating again the endothermic peak at 95°C appears together with a new endothermic peak at 111°C. With the appearance of the new peak, the enthalpy involved during the transition at 95°C reduces from 86 to 31 J/g. On successive cooling

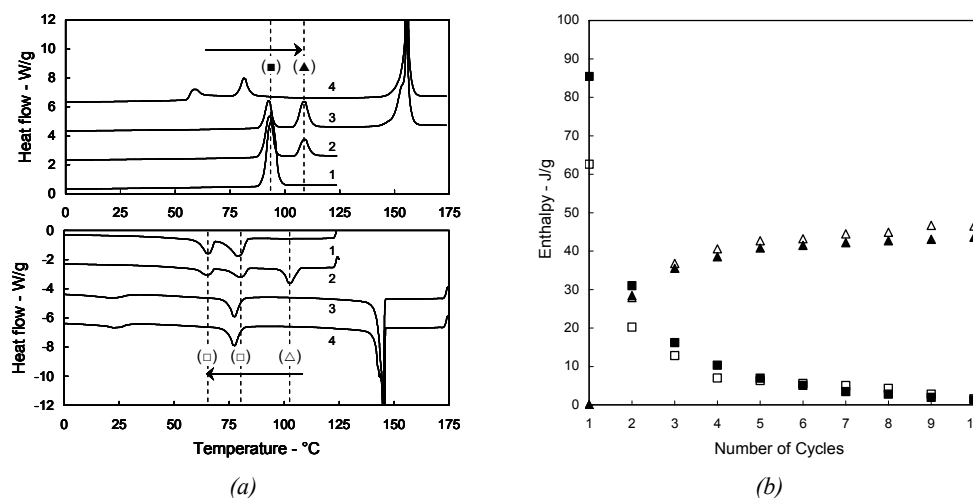


Figure 2.6: DSC results of EDHA crystallized from the superheated state of water that was exposed to (a) two heating (upper thermograms) and cooling profiles (lower thermograms) between -25 and 125°C, after which the samples were heated above the melting temperature at 157°C. A detailed study on the specific changes in the phase transitions at 95°C (■) and 111°C (▲) on heating and at 103°C (△) and 83/59°C (□) on cooling was investigated by following the corresponding enthalpies during 10 sequential temperature cycles ranging from -25 and 125°C (b).

together with the exothermic peaks at 83 and 59°C a new exothermic peak at 103°C appears. In the following intermezzo this particular trend was investigated in more detail applying 10 sequential temperature profiles ranging between -25 and 125°C, Figure 2.6b.

During the respective heating runs, presented in the upper part of Figure 2.6b, the enthalpy involved in the endothermic transition at 95°C decreases gradually to zero, whereas the endothermic transition at 111°C increases in enthalpy to 43J/g. While upon the successive cooling cycles, the exothermic transition at 103°C strengthens with the disappearance of the exothermic peaks at 83 and 59°C. Considering the identical enthalpy involved during the endo- and exothermic transitions at 111 and 103°C, and their existence after the successive heating and cooling runs, this new transition can be attributed to a first order crystal to crystal transition. Moreover, the disappearance of the endo- and exothermic peaks observed initially suggests a metastable nature of the crystals obtained from the superheated state of water. The intermezzo is finalized with the conclusion that the metastable crystals tend to transform into crystals having higher endo- and exothermic transitions at 111 and 103°C.

By heating the water crystallized sample above the melting temperature, the discussion of Figure 2.6a is continued. It is to be noted that in the third trajectory on heating both the 95°C and the 111°C transitions are still present. On cooling the molten sample crystallization occurs at 145°C and two exothermic events identical to the melt crystallized samples are observed, namely at 78°C (24.4 J/g) and 21°C (14.7 J/g).

The phase transitions recorded by DSC, as reported above, are reproducible. However, sometime on the very first heating run of the water crystallized material instead of two endothermic peaks at 95 and 157°C, three endothermic peaks at 95, 111 and 157°C are observed; a scenario similar to the second heating trajectory, Figure 2.6a.

It is feasible to obtain single crystals of EDHA from water. Platelet like crystals obtained from water provide a unique opportunity to follow the phase transitions in-situ by optical microscopy. Figure 2.7 depicts such crystals as observed in between cross polars using a red wave plate, mounted at 45° to the polarized light. Two crystals, named A and B, exhibit orange or blue color due to subtraction or addition of the fast direction of the light. On heating from 5 to 105°C, on the first transition Figure 2.6a, the colors of the platelets tend to change, following the first order transitions in the Michelle Levy chart. While crystal A changes in color from orange to blue, crystal B changes in color from blue to grey. The changes in color suggest a variation in retardation thickness, which is likely to arise due to changes in the molecular packing within the crystal. On heating further, with the transition at 111°C, once again sudden changes in the colors are observed suggesting changes in retardation thickness. On cooling, changes in colors together with the development of striations specifically around 83°C are observed. These striations tend to propagate through the crystal surface and are indicative for molecular rearrangement within the crystal. On cooling to 5°C, mechanical repositioning of the crystals causes crystal B to flip away from crystal A. It is to be noted that the color of crystal A does not return to the

starting condition, suggesting differences in the retardation thickness of the starting and cooled state of the same crystal. Crystal B becomes transparent after flipping. The transparency between the cross polars will arise if the chains are arranged parallel on the crystal surface, and the polarized light falls parallel to the chains. This is further confirmed as the crystal becomes highly birefringent on its rotation by 45° to the plane of incident polarization.

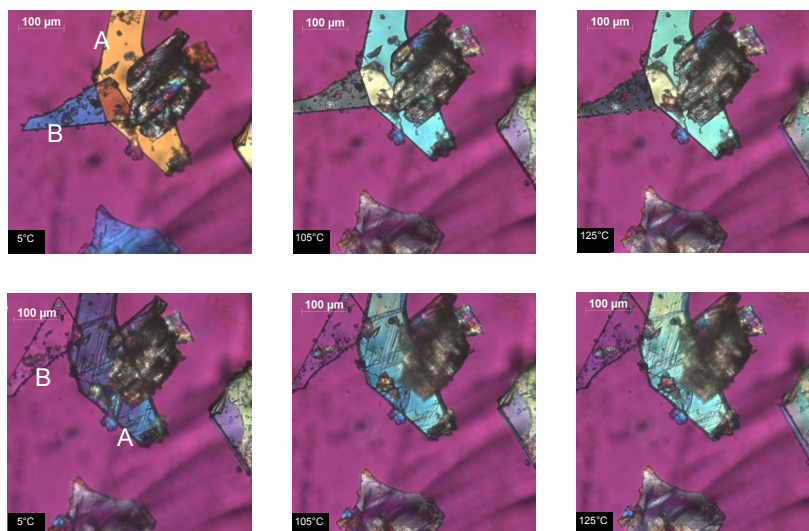


Figure 2.7: Optical micrographs demonstrating the crystalline transformations of EDHA single crystals grown from aqueous environment in sequential heating. During the 95°C transition in the first temperature run, presented in the upper row, all crystals change, A and B in particular change in color following the first order transitions in the Michelle Levy chart. A second heating of the crystals (lower row), shows only minor changes in birefringence of the crystals. However the transparency of crystal B after flipping indicates that the chains are positioned parallel on the surface.

To follow the crystallographic changes during the phase transitions, time-resolved WAXD studies are performed on the platelets that are isotropically distributed. In comparison with melt crystallized samples recorded at 5°C , Figure 2.4d, the water crystallized WAXD appears to have better resolved peaks, Figures 2.8a. Powder diffraction indexing (TREOR 90) reveals once more a triclinic packing of the chains with however differences in lattice parameters, Tables 2.3 and 2.4. For a comparison of the melt and the water crystallized EDHA at 5°C , see Tables 2.2 and 2.4 respectively. From the comparison, which is also illustrated by means of the diffraction patterns in Figure 2.9, it is evident that the unit cell volume has hardly changed on crystallization from the superheated state of

water. The lattice parameters however are affected considerably, which may arise due to presence of water molecules within the lattice. Especially the interchain/intrasheet and interchain/intersheet distances, represented by the 010 and 100 diffraction signals respectively, increase significantly. On heating, around 95°C the disappearance and shifting of several diffraction signals coupled with the changes in the intensity profile

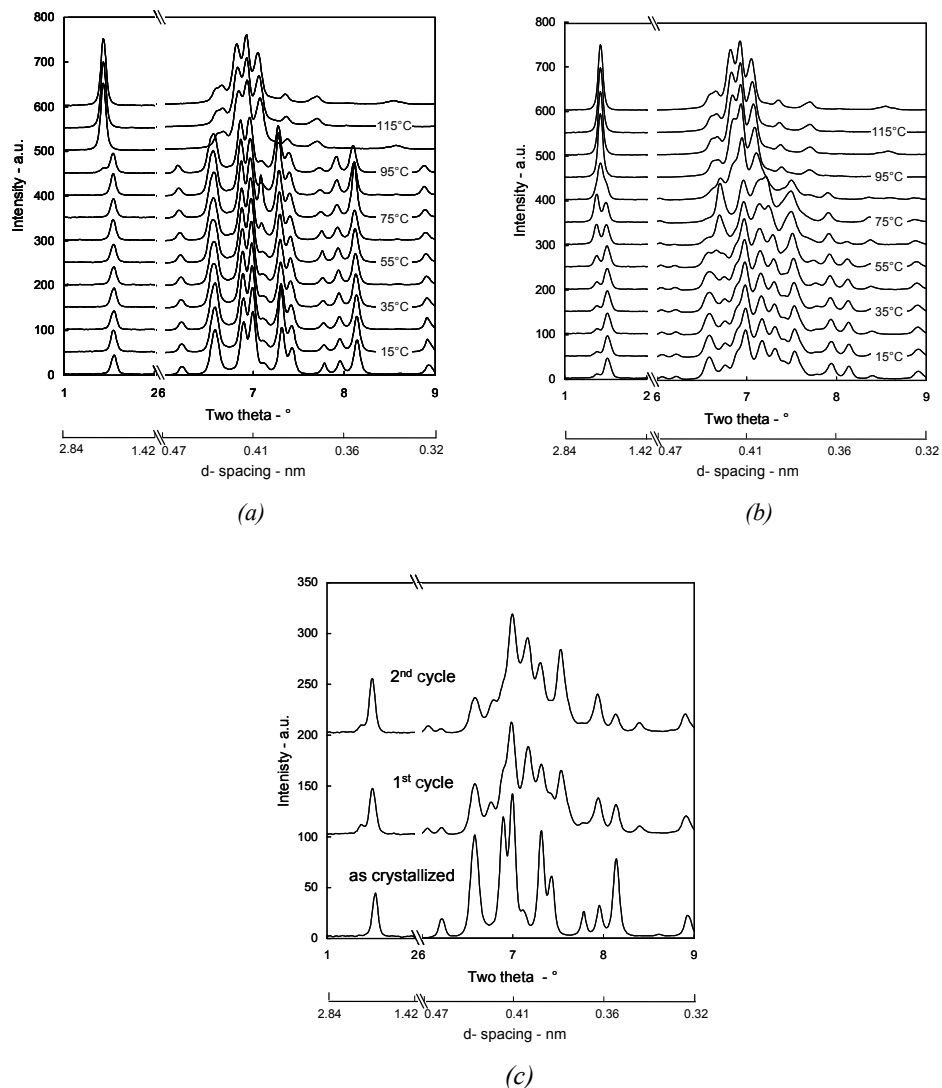


Figure 2.8: Structural changes by WAXD ($\lambda = 0.0496$ nm) in water crystallized EDHA at 95°C on heating (a) and two different crystalline rearrangements (b) of which the first transition results in a novel crystal that becomes more pronounced after two sequential temperature cycles (c).

suggests a sudden transformation in the lattice. In DSC this crystallographic transformation is observed as an endothermic transition. One of the apparent changes during the phase transformation is the increase in the d -value of the 001 diffraction signal from 1.82 to 1.93 nm, corresponding to the projected length of the molecule. Table 2.3 shows good coherence between the experimental and calculated powder diffraction pattern at 125°C. The Pawley refinement reveals a triclinic packing for the molecules at 125°C (Table 2.4). On heating from 5 to 125°C prior to the transition, hardly any significant changes are observed. While on cooling, Figure 2.8b, sudden changes in the crystallographic packing are revealed with the changes in the diffraction patterns at approximately 75 and 55°C. These transformations are in accordance with the phase transitions observed in the first cooling run in DSC, Figure 2.6a. The cooled X-ray diffraction pattern at 5°C, represents a mixture of the starting crystal (XRD pattern in the Figure 2.8a at 5°C) and the phase transformed XRD pattern having the endothermic transition temperature at 111°C in Figure 2.6a. On successive heating and cooling cycles, the XRD pattern at 5°C resolves to the XRD pattern shown in Figure 2.8c. The same pattern can be also obtained by subtraction of the XRD pattern at 5°C after the first cooling run with the starting XRD pattern recorded for the water crystallized EDHA sample. Powder diffraction indexing performed on the XRD pattern for the new crystal, obtained after two sequential temperature cycles and

Table 2.3: Powder diffraction indexing of water crystallized EDHA before, at 125°C, and after the crystal conformation using TREOR 90 combined with a Pawley refinement ($\lambda = 0.0496 \text{ nm}$)^{a)}

Bravais-Miller indices			H ₂ O crystallized before heating at 5°C			H ₂ O crystallized at 125°C			H ₂ O crystallized before cooling at 5°C		
h	k	l	$d_{obs.}$	$d_{sim.}$	Δ_d	$d_{obs.}$	$d_{sim.}$	Δ_d	$d_{obs.}$	$d_{sim.}$	Δ_d
			nm	nm	nm	nm	nm	nm	nm	nm	nm
0	0	1	1.830	1.830	0.000	1.976	1.976	0.000	1.872	1.872	0.000
0	0	2	0.915	0.915	0.000	0.988	0.988	0.000	0.936	0.936	0.000
0	0	3	0.609	0.610	-0.001	0.659	0.659	0.000	0.624	0.624	0.000
0	0	4	0.457	0.457	0.000	0.494	0.494	0.000	0.468	0.468	0.000
0	1	0	0.432	0.432	0.000	0.427	0.427	0.000	0.432	0.432	0.000
0	1	1	0.400	0.400	0.000	0.410	0.410	0.000	0.406	0.406	0.000
0	1	3	0.319	0.319	0.000						
0	-1	4	0.358	0.358	0.000						
1	0	0	0.412	0.412	0.000	0.417	0.417	0.000	0.418	0.418	0.000
1	0	1	0.389	0.389	0.000				0.390	0.391	-0.001
1	0	2				0.355	0.353	0.002			
1	0	3							0.320	0.318	0.002
-1	0	4							0.350	0.350	0.000
1	1	0	0.383	0.383	0.000	0.387	0.387	0.000	0.378	0.378	0.000
1	1	1	0.349	0.351	-0.002						
-1	-1	1	0.406	0.405	0.001	0.403	0.404	-0.001	0.397	0.397	0.000
-1	-1	4	0.365	0.365	0.000				0.359	0.359	0.000
-1	-1	5	0.330	0.330	0.000						

a) The observed diffraction signal, $d_{obs.}$, are assigned in Bravais-Miller indices and compared to the simulated diffraction signals, $d_{sim.}$. The difference is denoted as Δ_d .

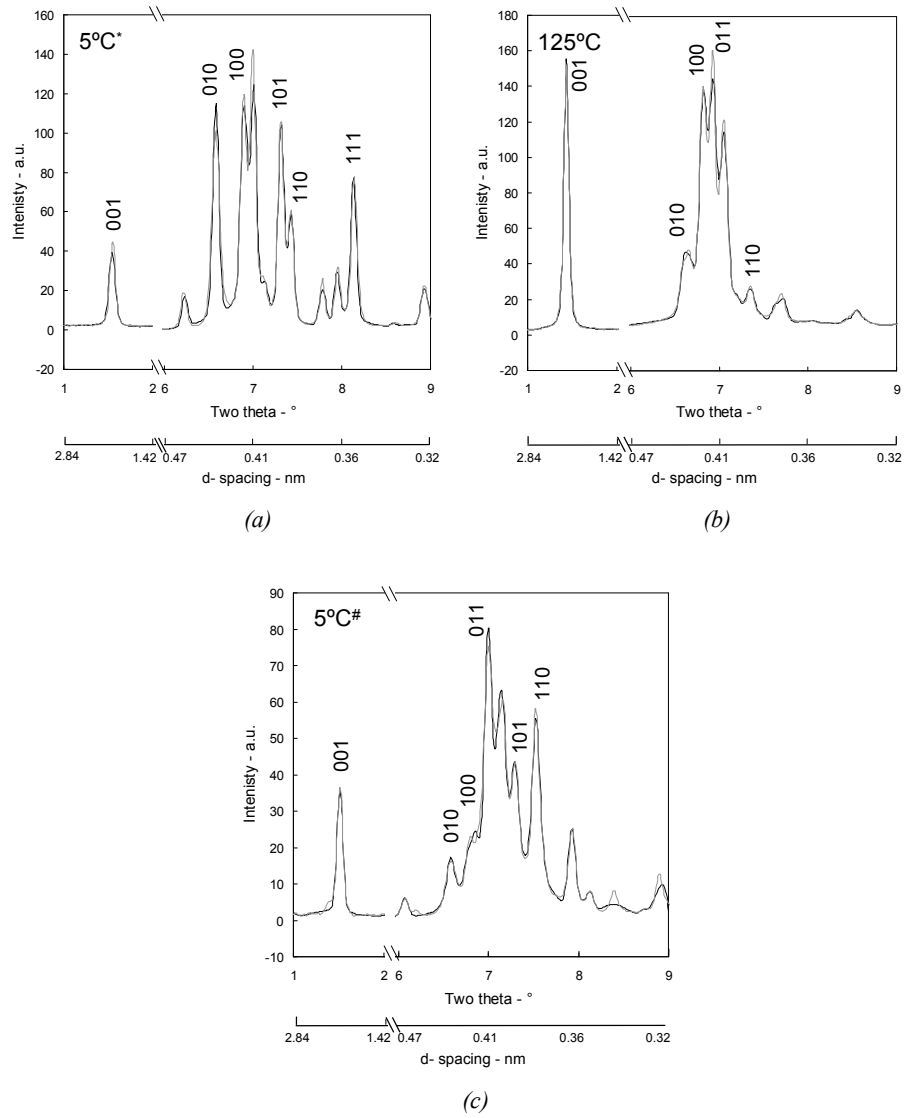


Figure 2.9: Experimental (grey) and TREOR 90 simulated (black) wide angle X-ray diffraction patterns of “fresh” EDHA crystals grown from the superheated state of water (a) that are exposed to a temperature cycle ranging from 5 to 125°C (figure b). Via the high temperature triclinic structure the water crystallized sample irreversible transforms in thermodynamically stable crystals, of which the diffraction patterns are shown in figure c.

having the endo- and exothermic transitions at 111 and 103°C, is shown in Table 2.3 as well. From the good fit of the simulated and experimentally observed XRD pattern it is evident that the crystal structure thus obtained is in a triclinic phase (Table 2.4). Lattice parameters of the new phase are shown in Table 2.2 as 5[#]. The observed minor changes in the crystallographic packing of the starting (5^{*}) and new phase (5[#]) are insufficiently substantial to justify the jump in the endothermic transition temperature from 95 to 111°C (Figure 2.6a). This increase in the endothermic transition may arise from hydrogen bonding efficiencies. Moreover, the increase in the *c*-axis to 1.99 nm may be explained by considering the rigidity arising in the hydroxylic protons located at the end of the molecule and as such contribute to the unit cell parameters.

Table 2.4: Diffraction signals and unit cell parameters of water crystallized EDHA prior* and after two sequential temperature cycles[#]

T	structure	WAXD diffraction signals					unit cell parameters						
		010	100	011	101	110	<i>a</i>	<i>b</i>	<i>c</i>	α	β	γ	<i>V</i>
°C		nm	nm	nm	nm	nm	nm	nm	nm	°	°	°	nm ³
5 [*]	triclinic	0.432	0.412	0.400	0.389	0.383	0.469	0.497	1.96	109	107	63.2	0.379
125 [*]	triclinic	0.427	0.417	0.410		0.387	0.481	0.478	2.09	102	108	63.9	0.407
5 [#]	triclinic	0.432	0.418	0.406	0.390	0.378	0.470	0.482	1.99	106	107	65.2	0.385

2.4 Conclusions

Below 85°C two salient crystal-to-crystal transitions are observed in EDHA crystallized from the melt that are not in agreement with the crystallographic changes occurring during the Brill transitions in polyamides. Nevertheless, the thermodynamic and crystallographic changes indicate that the two transitions, of which the first is marked by a relatively high entropic barrier, arise from the variations in hydrogen bonding efficiencies of the specific moieties and conformational changes along the backbone of the molecule. On heating, during the first endothermic transition at 63°C the triclinic crystal reorganizes into another triclinic crystal where the shear between neighboring chains α equals 102°, which indicates maximum hydrogen bounding efficiency. Simultaneously, non-trans aliphatic diamine conformations disappear and the molecular backbone, matching with the *c*-axis of the unit cell, adopts all-trans conformation. Above the second exothermic transition at 85°C a continuously growing population of gauche conformers, envisaged by a contraction of the *c*-axis, decreases the effective electron exchange between the amide motifs and weakens van der Waals forces considerably. After a sudden increase at 85°C the interchain/intrasheet and interchain/intersheet distances approach one another in a typical polyamide fashion.

Crystallization from superheated water results in a metastable triclinic structure. During sequential temperature cycles below the melting point, the metastable crystal reorganizes via a high temperature (above 95°C) triclinic structure into a new triclinic structure. In comparison with the melt crystallized sample, the metastable and new triclinic phases are characterized by relatively large interchain/intrasheet and interchain/intersheet distances. Expansion along the *c*-axis in the new triclinic phase results in the hypothesis that the rigid hydroxylic protons contribute to the unit cell and as such causes a significant increase in the transition temperature from 85 to 111°C. The melting temperature of EDHA crystallized from the melt and that crystallized from the superheated state of water are identical. Though these results demonstrate the influence of water molecules on stabilizing the crystals, the specific role of water molecules on hydrogen bonding and the crystal transformation at temperatures above 95°C requires further investigation. In the following chapter, with the help of FTIR and solid state NMR the presence of water molecules within the vicinity of the amide moieties and its role in the shielding of hydrogen bonding will be demonstrated.

2.5 References

1. Pimental, G. C.; McClellan, A. L. In *The Hydrogen Bond*, Freeman: San Francisco, **1960**.
2. Jeffrey, G. A. In *An Introduction to Hydrogen Bonding*, Oxford University Press: New York, **1997**.
3. J. -M. Lehn *Science* **1993**, 18, 1762-1763 .
4. Sijbesma, R. P.; Beijer, F. H.; Brunsveld, L.; Folmer, B. J. B.; Ky Hirschberg, J. H. K.; Lange, R. F. M.; Lowe, J. K. L.; Meijer, E. W. *Science* **1997**, 278, 1601-1604.
5. Rastogi, S.; Terry, A. E.; Vinken, E. *Macromolecules* **2004**, 37, 8825-8828.
6. Yin, J.; Rastogi, S.; Terry, A. E.; Popescu, C. *Biomacromolecules* **2007**, 8, 800-806.
7. Challa, G. *Plastica* **1969**, 22, 204-208.
8. Jedlovszky, P.; Brodholt, J. P.; Bruni, F.; Ricci, M. A.; Soper, A. K.; Vallauri, R. *J. Chem. Phys.* **1998**, 108, 8528-8540.
9. Vinken, E.; Terry, A. E.; Van Asselen, O.; Spoelstra A. B.; Graf, R.; Rastogi, S. *Langmuir* **2008**, 24, 6313-6326.
10. Lips, P. A. M.; Broos, R.; Van Heeringen, M. J. M.; Dijkstra, P. J.; Feijen, J. *Polymer* **2005**, 46, 7823-7833.
11. Lips, P. A. M.; Broos, R.; Van Heeringen, M. J. M.; Dijkstra, P. J.; Feijen, J. *Polymer* **2005**, 46, 7834-7842.
12. Jones, N. A.; Atkins, E. D. T.; Hill, M. J.; Cooper, S. J.; Franco, L. *Macromolecules* **1996**, 29, 6011-6018.

-
13. Jones, N. A.; Atkins, E. D. T.; Hill, M. J.; Cooper, S. J.; Franco, L. *Polymer* **1997**, 38, 2689-2699.
 14. Jones, N. A.; Atkins, E. D. T.; Hill, M. J.; Cooper, S. J.; Franco, L. *Macromolecules* **1997**, 30, 3569-3578.
 15. Nair, S. S.; Ramesh, C.; Tashiro, K. *Macromolecules* **2006**, 39, 2841-2848.
 16. Brill, R. *J. Prakt. Chem.* **1942**, 161, 49-64.
 17. Yoshioka, Y.; Tashiro, K.; Ramesh, C. *Polymer* **2003**, 44, 6407-6417.
 18. Yoshioka, Y.; Tashiro, K. *Polymer* **2003**, 44, 7007-7019.
 19. Yoshioka, Y.; Tashiro, K. *J. Phys. Chem. B.* **2003**, 107, 11835-11842.
 20. Vanhaecht, B.; Devroede, J.; Willem, R.; Biesemans, M.; Goonewardena, W.; Rastogi, S.; Hoffmann, S.; Klein, P. G.; Koning, C. E. *J. Polym. Sci. Part A.: Polym. Chem.* **2003**, 41, 2082-2094.
 21. Hoffmann, S.; Vanhaecht, B.; Devroede, J.; Bras, W.; Koning, C. E.; Rastogi, S. *Macromolecules* **2005**, 38, 1797-1803.
 22. Vinken, E.; Terry, A. E.; Hoffmann, S.; Vanhaecht, B.; Koning, C. E.; Rastogi, S. *Macromolecules* **2006**, 39, 2546-2552.
 23. Katayama, S.; Horikawa, H. *J. Appl. Polym. Sci.* **1971**, 15, 775-796.
 24. Werner, P. E.; Eriksson, L.; Westdahl, M. *J. Appl. Cryst.* **1985**, 18, 367-370.
 25. Engel, G. E.; Wilke, S.; Harris, K. D. M.; Leusen, F. J. J. *J. Appl. Cryst.* **1999**, 32, 1169-1179.
 26. Jones, N. A.; Cooper, S. J.; Atkins, E. D. T.; Hill, M. J.; Franco, L. *J. Polym. Sci. Part B.: Polym. Phys.* **1997**, 35, 675-688.
 27. Harings, J. A. W.; Van Asselen, O.; Graf, R.; Broos, R.; Rastogi, S., *Cryst. Growth Des.* **2008**, 8, 3323-3334.
 28. Korbee, R.A.; van Geenen, A.A. *Patent WO99/29767* **1999**.
 29. Korbee, R.A.; van Geenen, A.A. *Patent US6350805* **1999**.

Chapter 3*

The role of superheated water on shielding and mediating hydrogen bonding in N,N'-1,2-ethanediyl-bis(6-hydroxy-hexanamide) crystallization

The role of superheated water on hydrogen bonding in amide crystallization was examined by the use of low molecular weight N,N'-1,2-ethanediyl-bis(6-hydroxy-hexanamide) model crystals that form hydrogen bonded sheets stacked by van der Waals forces. Thermodynamic, structural and conformational studies reveal that despite a low temperature transition, which originates in a reversible change from cooperative configurational flip-flop to conformational hydroxylic hydrogen bonding, a delicate balance between conformational disorder/order in the aliphatic segments and hydrogen bonding efficiency between the hydrogen bonded moieties validates the role of N,N'-1,2-ethanediyl-bis(6-hydroxy-hexanamide) as a model compound representing the crystalline domains in polyamides. Crystallization from the superheated state of water results in the formation of a thermodynamically metastable phase, where water molecules in the vicinity of the amide moieties shield the interchain/intrasheet hydrogen bonding. Because of this shielding, water molecules erase the conformational limitations of the planar amide motifs during crystallization, and trans methylene conformations along the entire molecules coexist with strong intermolecular hydroxylic hydrogen bonding. By annealing or sequential temperature cycles the metastable crystals tend to transform irreversibly into thermodynamically more stable crystals. During the transformation the water molecules migrate from the amide moieties. Since the highly efficient hydrogen bonding between highly ordered hydroxylic end groups decreases the effect of thermally triggered rotating gauche conformers, less effect of the crankshaft type of motion in the methylene segments requires more energy to pursue a solid state crystalline transition. Conclusively, physically bound water molecules near the amide motifs shield intermolecular hydrogen bonding and mediate the formation of stabilizing hydroxylic hydrogen bonds.

* Partially reproduced from Harings, J.A.W.; Van Asselen, O.; Graf, R.; Broos, R.; Rastogi, S., *Cryst. Growth Des.* **2008**, 8, 3323-3334

3.1 Introduction

The thermally induced Brill transition in aliphatic polyamides, commonly known as nylons, is a solid-state transformation from mainly a monoclinic or triclinic structure into a pseudohexagonal packing¹⁻⁶. The transition arises due to the tendency of thermally introduced gauche conformers to migrate from the lattice, which consists of hydrogen bonded sheets that are stacked by van der Waals interactions. The migration entails a crankshaft type motion along the *c*-axis, initiating out-of-plane wagging vibrations of the amide motifs⁷⁻⁹. Together with a weakening of the van der Waals forces at elevated temperatures, which causes an increase in the intrachain/intersheet distance, the either progressive or alternative shear between the hydrogen bonded sheets also increases. Despite the relatively high out-of-plane wagging vibrations caused by the migration of gauche conformers from the lattice, the retention of electron exchange between the hydrogen bonded moieties combined with the motion along the *c*-axis decreases the interchain/ intrasheet distance⁹. The temperature where the interchain/intersheet and interchain/ intrasheet distances merge is referred as the Brill transition temperature¹⁰.

In the vicinity of the Brill transition, where the effectiveness of electron exchange decreases, the presence of water molecules in the superheated state is likely to influence the chain packing within the crystal. At temperatures close to (or above) the boiling point of water, the disruption of the space filling percolating hydrogen bonded network in water entails highly favorable interactions between nylon and water, enabling mobile water molecules to penetrate the crystalline domains and dissolution occurs¹¹⁻¹³. Under superheated conditions possible electron exchange between water molecules and another electron donor and acceptor pairs may cause the formation of clathrates on cooling¹³⁻¹⁴. In the previous chapter the use of a low molecular weight bisamide-diol molecule N,N'-1,2-ethanediyl-bis(6-hydroxy-hexanamide) (EDHA) was proposed as a model that represents crystalline domains in polyamides, circumventing variations in the amorphous component¹⁵. To elucidate the structural complexity of these self-assembled hydrogen bonded molecules, especially after crystallization from the superheated state of water, the support of conformational analysis by FTIR and solid state NMR spectroscopy is required.

Here some of the salient phase transitions that occur in EDHA crystallized from melt are recalled. Below 85°C, crystallographic changes in the two crystalline transitions of EDHA do not coincide with the anticipated crystallographic changes for the Brill transition. However, the crystallographic changes occurring during the two phase transitions suggest differences in electron exchange between the hydrogen bonded motifs and conformational changes along the *c*-axis. During the first of the two phase transitions (endothermic transition at 63°C) the crystal reorganizes into another triclinic structure with linearly aligned hydrogen bonds, increasing the maximum hydrogen bonding efficiency². The *c*-axis of the unit cell matches the molecular length in all-trans conformations. Above the second endothermic phase transition at 85°C, the molecular backbone starts to contract

with a continuously growing population of gauche conformers and a simultaneous weakening of the hydrogen bonding and van der Waals interactions. The interchain/intrasheet and interchain/intersheet distance, which suddenly increases at 85°C, approach one another similar to the observations on nylons.

In chapter 2 it was also demonstrated that crystallization of EDHA from the superheated state of water results in a metastable phase. On subsequent heating and cooling cycles below the melting point the metastable phase reorganizes into a new triclinic structure. Compared to the melt crystallized sample, the metastable and the new triclinic phases show increased interchain/intrasheet and interchain/intersheet diffraction signals. Expansion along the *c*-axis in the new triclinic phase results in the hypothesis that the hydroxylic protons located at the chain ends contribute to the unit cell and as such result into a considerably different single crystal-crystal (solid-solid) phase transition at 111°C, compared to the two phase transitions in the melt crystallized sample at 63 and 85°C¹⁵. However, the melting temperature of the two samples, crystallized from melt or superheated water, remains the same. These findings conclusively demonstrate the significant influence of water molecules on the stabilization of the crystal packing. To reveal the specific role of water molecules on the stabilization of the crystal lattice in more detail, temperature dependent FTIR and solid state ¹H and ¹³C NMR measurements have been performed. Both methods, and in particular the combination of both, are capable of distinguishing the influence of conformational changes and the influence of water molecules on hydrogen bonding in N,N'-1,2-ethanediyl-bis(6-hydroxy-hexanamide).

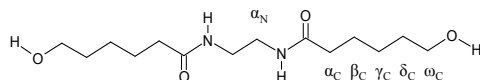


Figure 3.1: Labeling of *N,N'*-1,2-ethanediyl-bis(6-hydroxy-hexanamide)

3.2 Experimental section

3.2.1 Materials

1,2-Diaminoethane and ϵ -caprolactone were purchased from Aldrich, The Netherlands. Tetrahydrofuran (THF) and acetonitril, both of analytical grade, were obtained from Biosolve, The Netherlands. N,N'-1,2-ethanediyl-bis(6-hydroxy-hexanamide), denoted as EDHA and sketched in Figure 3.1, was synthesized using a modified procedure of Katayama¹⁶. A solution of ϵ -caprolactone (0.17 mol) in 25 mL of THF was added in 2 hours to a solution of 1,2-diaminoethane (0.087 mol) in 50 mL THF. Subsequently, the mixture was stirred at 10°C for 40 h. Then THF was removed under reduced pressure, and the precipitate was purified by successive recrystallization in an

acetonitril/water (7/1, v/v) solution. Melt crystallized samples were obtained by cooling from the melt at 10°C/min to 5°C. A part of the melt crystallized sample was dissolved in water at 90°C, thus partially disrupting the percolating hydrogen bonded network of water. Upon cooling the solution, at a rate of 10°C/min, the dissolved bisamide-diol crystallized.

3.2.2 Fourier transfer infrared spectroscopy

Conformational changes of melt crystallized EDHA as well as single crystals grown from H₂O and D₂O were studied by FTIR spectroscopy. The crystals were placed on a zinc selenium disk and spectra were recorded on a Bio-Rad FTS6000 spectrometer equipped with a microscope with a resolution of 2 cm⁻¹ in transmission mode. Polarized FTIR was performed on single crystals to gain further insight in the orientation of the hydrogen bonded moieties on an atomistic level. Single crystals grown from H₂O and D₂O were exposed to two temperature cycles from 5 to 125°C, followed by two cycles from 5 to 175°C. Phase transitions during the heating and cooling cycles are shown in Figure 3.2 and have been discussed in detail in chapter 2. Spectra of the melt crystallized samples were recorded in a single temperature cycle from 5 to 175°C. Phase transitions occurring during this cycle are shown by DSC trace 4. For FTIR studies, the temperature cycles, characterized by a rate of 10°C/min, were controlled by a linkam TMS94 hotstage. At every 10°C the average of 100 FTIR spectra was recorded after 3 min of isothermal period.

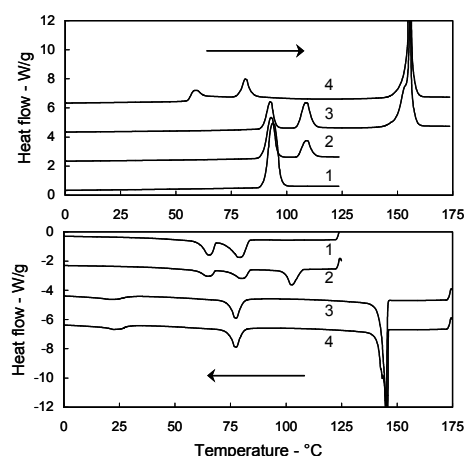


Figure 3.2: Four consecutive DSC thermograms of EDHA, from 1 to 4, during heating (upper set) and cooling (lower set) cycles are shown in this figure. The starting sample was crystallized from the superheated state of water. Thermograms 1 and 2 were heated/cooled from -25 to 125 °C. In cycle 3, the sample was heated above the melting temperature (157 °C). Thus trace 3 in the lower set shows crystallization on cooling from the melt. Trace 4 shows transitions in the melt crystallized sample.

3.2.3 Solid state nuclear magnetic resonance spectroscopy

Solid state ^1H and ^{13}C NMR spectroscopy were performed respectively on a Bruker Avance console operating at 700 MHz ^1H Larmor frequency and a Bruker DSX spectrometer with 500 MHz ^1H Larmor frequency at the Max Planck Institute for Polymer Research (MPI-P) in Mainz, Germany. For ^1H NMR measurements a zirconia rotor with 2.5 mm outer diameter, filled with either the melt or water crystallized sample, was placed in a commercial MAS probe and spun at 30 kHz. ^1H MAS spectra as well as two-dimensional ^1H double quantum correlation spectra were recorded in a temperature range from 22 up to 157°C. The known differences between bearing gas and sample temperature have been taken into account and the corrected temperatures are given throughout the chapter¹⁷. ^{13}C CP MAS NMR experiments in contrast were performed using rotors with 4 mm outer diameter, spinning at 10 kHz MAS frequency and spectra were recorded at various temperatures, ranging from 27 to 127°C.

3.3 Results and discussion

3.3.1 Hydrogen bonding in melt crystallized EDHA

In the low temperature phase, at ~20°C, EDHA molecules have a low molecular mobility. This is reflected in the ^1H NMR spectra by relatively broad signals, where the signal at a chemical shift of 8.6 ppm represents the NH proton and one broad unresolved peak covers all aliphatic protons (Figure 3.3). However, the ^{13}C CP MAS spectra, Figure 3.3, provide sufficient resolution even at low temperatures. The molecular assignment of the different ^1H and ^{13}C signals are summarized in Table 3.1 using the labeling scheme given in Figure 3.1. The splitting of the carbonyl (174.9 and 173.9 ppm) in the CP-MAS spectrum at ambient temperatures is indicative for two different chemical environments or local conformations, possibly suggesting the coexistence of in and out of plane hydrogen bonding. Normally, the higher chemical shift of the ^{13}C carbonyl signal, accounts for the lesser shielding of the carbon nucleus by its surrounding electron cloud. The shielding of the carbonyl nucleus by the electrons decreases with higher efficiency of the electron exchange between electron donor and acceptor. Another splitting is observed for the methylene groups next to the hydroxylic end groups (ω_{C}) at ambient temperatures (20°C). In contrast, the α_{C} ^{13}C signal at 36.5 ppm is in good agreement with reported α_{C} chemical shifts for even-even nylons, such as nylon 4.6 and nylon 6.6¹⁸, and the α_{N} methylene segment is positioned at a relatively high chemical shift (40.7 ppm). On heating from 20°C onward, prior to the endothermic phase transition at 63°C the position of the peaks and peak widths in the ^1H MAS and the ^{13}C CP-MAS NMR spectra remain unchanged.

With the first endothermic transition at 63°C (Figure 3.2), the ^{13}C CP-MAS NMR spectra shown in Figure 3.3, register major changes. For example, the $\alpha_{\text{N}}\text{CH}_2$ ^{13}C signal shifts from 40.7 to 39.9 ppm, whereas the chemical shift of the α_{C} methylene segment increases from 36.5 to 37.4 ppm. The β_{C} and γ_{C} methylene units, registered as a single peak (27.5 ppm) at 20°C, split into separate chemical shifts at 28.3 and 26.9 ppm. At the phase transition, the doublet of the carbonyl signal merges into a single NMR signal at 174.3 ppm. The same occurs for the ^{13}C signal for $\omega_{\text{C}}\text{CH}_2$ unit, which appeared in the low-temperature phase at 20°C as a doublet (63.4 and 62.9 ppm), and merges into a single chemical shift, 63.8 ppm. In the ^1H MAS spectrum, the signal of the amide proton shifts at the transition from 8.6 to 8.9 ppm. These observations are in agreement with the crystallographic changes occurring during the phase transition at 63°C¹⁵, where the hydrogen bonding between the amide moieties is influenced.

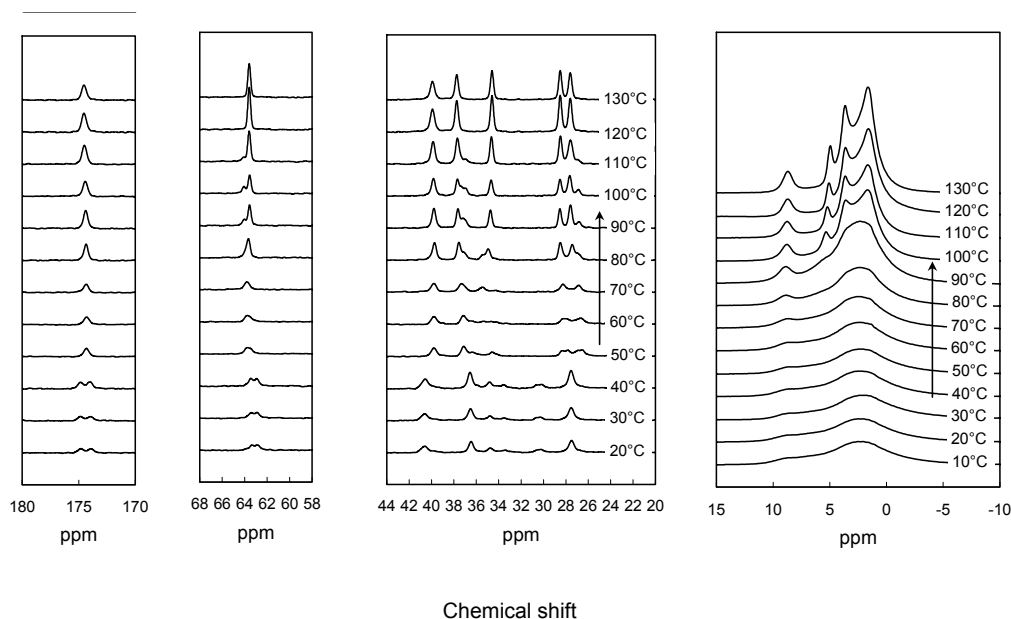


Figure 3.3: Solid state ^1H MAS (15 to -10 ppm) and ^{13}C CP-MAS spectra (180 to 20 ppm) for melt crystallized EDHA on heating up to 130°C.

Upon further heating, a second endothermic transition at 85°C is observed (Figure 3.2) which leads to substantial increase in intensity of the ^1H and the ^{13}C NMR signals. This sudden increase is attributed to the onset of molecular motion, reducing the T_2 of the ^1H spins and thus providing narrower ^1H lines and better CP efficiency. It should be noted that this change occurs without significant changes in the chemical shifts, though the emergence of a distinctly strong peak at 34.6 ppm is noticed in the ^{13}C spectra.

It is to be noticed that during the first endothermic transition the ^1H spectra hardly change, while the ^{13}C CP-MAS spectra change significantly with the major shifts in the peak positions. On the other hand, during the second endothermic transition distinct resolution in the ^1H spectra evolves while the ^{13}C spectra sharpens without changes in the chemical shift. From these observations it can be concluded that the first endothermic transition involves major changes that arises due to chain packing, most likely influenced by hydrogen bonding and complements the crystallographic studies (Table 2.2 in chapter 2). The second endothermic transition however causes a sudden increase in molecular mobility, favoring the induction of gauche conformers along the c -axis, which are observed in the ^{13}C CP-MAS spectra as the appearance of new peak at 34.6 ppm. The appearance of this signal in the ^{13}C CP-MAS spectrum prior to the second endothermic phase transition suggests that the induction of gauche conformers on heating triggers the transition. To follow the conformational changes arising from the phase transformations, which seem to be triggered by hydrogen bonding efficiencies, detailed FTIR studies have been performed.

Table 3.1: Representative ^1H and ^{13}C chemical shifts in the different crystalline states of EDHA crystallized from melt during heating and EDHA crystallized from the superheated state of water during the first temperature cycle

	Chemical shifts					
	C=O ^{13}C	ω_{C} ^{13}C	α_{N} ^{13}C	α_{C} ^{13}C	N-H ^1H	O-H ^1H
	ppm	ppm	ppm	ppm	ppm	ppm
Melt crystallized $^{\text{T1}}$						
130°C	174.6	63.6	40.0	37.8	8.6	4.8
60°C	174.3	63.8	39.9	37.4	8.9	-
20°C	174.9/173.9	63.4/ 62.9	40.7	36.5	9.2	-
H ₂ O crystallized $^{\text{T1}}$						
130°C	174.5	63.5	40.0	37.8	8.5	4.7
100°C	174.2	63.9	39.8	37.1	8.7	-
20°C	174.4	63.8	39.9	36.7	9.4	-
H ₂ O crystallized $^{\text{T1}}$						
130°C	174.6	63.6	40.0	38.9	8.4	4.6
90°C	174.4	64.0	40.0	37.3	8.7	-
20°C	174.3	63.7	40.0	37.1	9.1	-

During the first endothermic transition at 63°C in the FTIR spectra the resolution of the antisymmetric and symmetric CH₂ stretch vibrations in the region of 3000 to 2800 cm⁻¹ decreases. Especially the stretch vibrations at 2967 and 2888 cm⁻¹, arising due to restricted mobility at low temperature, tend to merge with the stronger peaks in the vicinity (Table 3.2). The observed shift to the lower wavenumber is in accordance with small cyclic

alkanes, where the ring tension increases the wavenumber of CH₂ stretch vibrations¹⁹. Moreover, the CH₂ scissoring band next to the NH at 1475 cm⁻¹, which is present due to constrained conformation in the crystal lattice, and the amide III band at 1251 cm⁻¹ (C-N stretch + C-N-H bend in plane, coupled to carbon) on the phase transition broadens significantly. This change implies a sudden release of restrictions in the aliphatic diamine segment. These observations are in accordance with the shifts observed on the phase transition in the ¹³C NMR signal of the methylene segments next to the amide moieties.

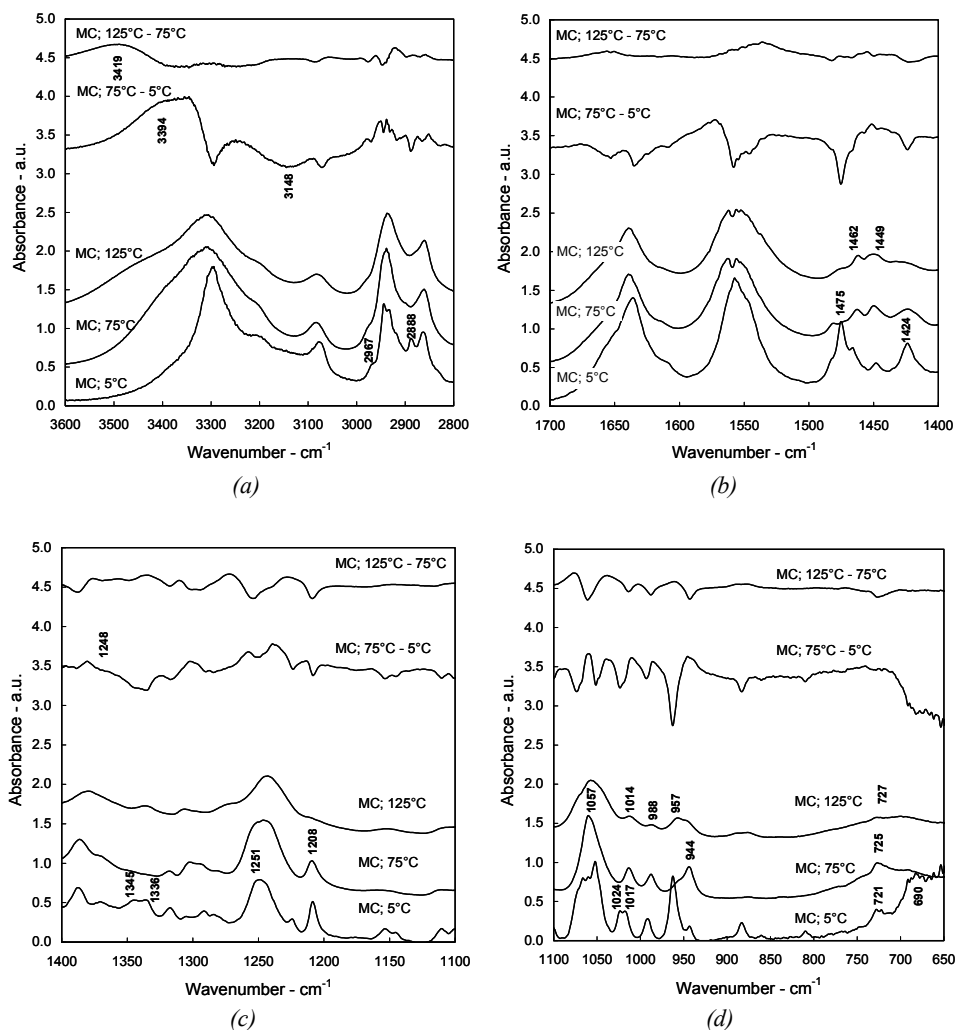


Figure 3.4: FTIR spectra of melt crystallized EDHA at 5°C, 75°C and 125°C, representing the different temperature dependent crystallographic packings. The subtraction spectra, represented as 75°C - 5°C and 125°C - 75°C, stress the conformational changes in the crystalline transitions.

These changes in NMR are too pronounced to be associated with the changes in hydrogen bonding observed on heating only¹⁸.

With the transition the appearance of the CH₂ scissoring vibrations at 1481 and 1424 cm⁻¹ are indicative for trans methylene-amide couplings on either side of the amide moiety. At the same time, the disappearance of the amide V band at 690 cm⁻¹ (NH out-of-plane scissoring) indicates the establishment of maximum hydrogen bonding efficiency. These observations, that is, the establishment of maximum hydrogen bonding efficiency in combination with the all-trans chain conformation of methylene units, are in agreement with the crystallographic findings of chapter 2.

The low wavenumber for the OH stretch vibration at 3148 cm⁻¹, suggests that the hydroxylic end groups are strongly hydrogen bonded at low temperatures. In biological structures such as β-cyclodextrinH₂O, cooperative arrangements of hydroxyl groups into long (O-H···O-H···)_n hydrogen bonded chains result in an entropic stabilization of crystalline structures^{19,20}. This type of hydrogen bonding, also referred to as flip-flop hydrogen bonding, might explain the position of the OH stretch vibration at 3148 cm⁻¹. The cooperative arrangement of the hydroxyl groups in combination with the retention of hydrogen bonding between amide moieties will promote an alternating tilt of the molecules within the hydrogen bonded sheets. The tilt will cause the length of the molecule along its backbone to deviate from the *c*-axis of the crystallographic unit cell, as witnessed by the crystallographic study, chapter 2. On heating through the first endothermic transition at 63°C the OH stretch band shows a pronounced shift from 3148 to 3394 cm⁻¹. This shift arises with the weakening of hydroxylic hydrogen bonding. The appearance of a weaker hydrogen bonded OH stretch band at 3394 cm⁻¹ and a better resolved C-OH vibration at 1057 cm⁻¹ suggests that the configurational nature of the hydrogen bonds changes.

At the low temperature, below 63°C, the covalent O-H bonds are continuously broken and the proton is transferred across the O-H···O bond²⁰. Above 63°C the covalent bond is less perturbed compared to the hydrogen bonding. Hence the hydroxyl groups are able to rotate from one hydrogen bonding position into the other, weakening the intermolecular hydrogen bonding. This change from cooperative configurational flip-flop to conformational hydrogen bonding, which triggers with the first endothermic event at 63°C, is also depicted by the vibrational changes. The changes are the loss of the C-OH stretch band at 1024 cm⁻¹ and the disappearance of the two OH bending vibrations at 1345 and 1336 cm⁻¹.

As observed by X-rays, with the second transition above 85°C, similar to nylons the interchain/intrasheet and interchain/intersheet distance approach each other. With the increase of gauche conformers (e.g., at 1462 and 1449 cm⁻¹) the skeletal C-C stretch bands at 1014 and 988 cm⁻¹ decrease. A simultaneous decrease in the relative intensity of the methylene rocking band at 727 cm⁻¹, reflects loss in the regular packing of methylene segments²¹. The enhanced mobility in the methylene chains with introduction of gauche conformers causes appearance of a well resolved ¹³C signal at 34.6 ppm (Figure 3.3).

Table 3.2: FTIR spectral vibrations of melt crystallized EDHA in the different triclinic structures at 5°C, 75°C and 125°C (*s* = strong, *m* = medium, *w* = weak, *v* = variable).

band frequencies (cm ⁻¹)			relative intensity	band assignment
5°C	55°C	125°C		
-	3394	3419	m	OH stretch vibration; H-bonded
3296	3309	3310	s	NH stretch vibration H-bonded
3204	3203	3202	m	Amide I and amide II combination band
3148	-	-	m	OH stretch vibration strongly/configurationally H-bonded
3081	3083	3081	m	Amide II overtone band
2967	-	-	w	α_N CH ₂ antisym. stretch vibration in constrained environment
2938 ± 5	2939	2936	s	CH ₂ antisym. stretch vibration
2888	-	-	m	α_N CH ₂ sym. stretch vibration in constrained environment
2861 ± 5	2861	2861	m	CH ₂ sym. stretch vibration
1636	1639	1639	s	Amide I: C=O stretch vibration
1557	1557	1555	s	Amide II: C-N stretch and C-N-H bending in-plane vibration
-	1481	-	w	CH ₂ scissoring next to NH (α_N CH ₂) in trans conformation
1475	-	-	m	α_N CH ₂ scissoring band in constrained environment
-	-	1462	m	CH ₂ scissoring in gauche conformation
-	-	1449	m	CH ₂ scissoring in gauche conformation
1424	1424	-	m	CH ₂ scissoring next to C=O (α_C CH ₂) in trans conformation
1345	-	-	w	OH bending vibration
1336	-	-	w	OH bending vibration
1251	1246/ 1209	1248/ 1209	v	Amide III: C-N stretch and C-N-H bending in-plane vibration coupled to skeletal carbon (α_C CH ₂)
1024	1057	1057	m/w	C-OH out-of-phase stretch vibration
1017	-	1014/ 988	m/w	Skeletal C-C stretch vibration
-	957	957	w/m	CC=O sym. stretch vibration in distorted conformation
943	944	-	w	CC=O sym. stretch vibration
721	725	727	w	most in-phase CH ₂ rocking mode in triclinic packing
690	-	-	w	Amide V: NH out-of-plane scissoring

The enhanced mobility caused by the increase in gauche conformers influences the vibrational modes of the hydroxyl groups, which is depicted by (1) broadening of the underlying OH stretch band that shifts from 3394 to 3419 cm⁻¹ on the transition, (2) broadening of the out-of-phase stretching of the C-OH vibration at 1057 cm⁻¹ and, (3) the sharp proton peak at 4.8 ppm at 130°C (Figure 3.3). Increased motion in the α_C CH₂-amide

couplings, which is witnessed by a typical distorted conformation of the symmetric $\text{CC}=\text{O}$ stretch vibrations at 957 cm^{-1} ²², promotes the out-of-plane wagging vibrations of the amide moieties. As a consequence less efficient electron exchange gives rise to better shielding of the proton nuclei in the amide motifs, causing a shift in the NH proton signal from 9.0 to 8.8 ppm. With the transition as the interchain/intrasheet hydrogen bonding weakens a slight shift of the amide II at 1555 cm^{-1} (C-N stretch; C-N-H bend-in-plane) and drastic changes in the amide III at 1248 and 1209 cm^{-1} are registered. While the crystal rearrangement at 63°C is caused by a change in the nature of hydrogen bonding, the phase transition at 85°C arises due to conformational changes in the methylene sequences.

3.3.2 Melt versus H_2O crystallization; the localization of H_2O molecules at RT

Previous studies performed by Vinken et al. suggest the presence of water molecules within the lattice¹³. In such a possibility the presence of the water molecules will influence the hydrogen bonding, which will feature in the NMR and FTIR spectra. What follows is our observation by the two techniques and a comparison with the melt crystallized sample. Figure 3.5 shows ^{13}C and ^1H spectra recorded on a water crystallized EDHA sample. Salient differences in the NMR spectra obtained from the melt and water crystallized samples are summarized in Table 3.1.

The very first, striking difference between the melt and the water crystallized EDHA is the ^{13}C signal for the carbonyl at room temperature. Around 174 ppm, unlike the split signals in the melt crystallized EDHA, a single peak at 174.4 ppm is observed in the water crystallized sample. This difference suggests the presence of only one specific chemical environment for the carbonyl carbon nucleus in the water crystallized EDHA. Considering the peak position of the carbonyl group of the water crystallized sample (174.4 ppm) similar to the melt crystallized sample between 63 to 85°C , the chemical environment of the two carbonyl groups can be considered to be the same. To recall, in EDHA crystallized from water at 20°C and the melt crystallized sample at temperatures between 63 and 85°C , identical alignment between the hydrogen bonding amide moieties is observed¹⁵.

Compared to the melt crystallized sample, in the water crystallized EDHA at 20°C the amide proton signal is observed at remarkably high chemical shift, namely at 9.4 ppm, with a relatively high intensity. The high chemical shift is indicative for an electron poor environment. In the water crystallized sample (at 20°C) the carbonyl shows a chemical environment similar to the melt crystallized EDHA ($63^\circ\text{C} < T < 85^\circ\text{C}$), but the chemical shift of the NH proton deviates significantly (8.9 ppm in comparison with 9.4 ppm) in the two samples. These observations suggest that crystallization from the superheated state of water hinders the establishment of hydrogen bonding between the adjacent amide motifs.

A comparison of the water and melt crystallized EDHA sample further reveals differences in the ^{13}C ω_{C} methylene signal at room temperature. The two signals at 63.4 and

62.9 ppm observed in the melt crystallized sample are replaced by a single peak at 63.8 ppm. Though the ^{13}C α_{C} methylene is hardly influenced by the crystallization conditions, the ^{13}C signal of the α_{N} carbon nuclei show significant changes. In the water crystallized sample the ^{13}C signal of the α_{N} carbon nuclei is observed at 39.9 ppm in comparison to 40.7 ppm in the melt crystallized EDHA at room temperature. Note that the α_{N} carbon nuclei position at 39.9 ppm is also observed in the melt crystallized EDHA but only at elevated temperatures between 63 and 85°C. To recall from the section above, this suggests the presence of all-trans conformation for aliphatic segments in the molecule.

What follows is a comparison between the melt and water crystallized sample as revealed by FTIR. The first columns of the Tables 3.2 and 3.3 summarize the vibrational bands with the corresponding assignments. At elevated temperatures water may promote the hydrolysis of amide based molecules such as EDHA, resulting in carboxylic acid and amine moieties. The absence of specific FTIR vibrations in the regions from 1760 to 1735 cm^{-1} and from 1730 to 1705 cm^{-1} , representing the non-hydrogen bonded and hydrogen bonded state respectively¹⁹, suggests that hydrolysis does not occur within the experimental time scale of dissolution. Besides, this conclusion is supported by the absence of amine protons in the ^1H MAS spectra of the water crystallized spectra that are presented in Figure 3.5. The comparison shows the absence of the cooperative $(\text{O}-\text{H}\cdots\text{O}-\text{H}\cdots)_n$ flip-flop hydrogen bonding at 5°C (Figure 3.6), which is expressed by the absence of a relatively broad OH stretch vibration at 3148 cm^{-1} in the water crystallized sample. Nevertheless, two new OH stretch vibrations are observed. One at 3401 cm^{-1} corresponding to an OH stretch vibration as observed in water molecules at room temperature and the other new vibration band overlapping with the NH stretch (3296 cm^{-1}) at 3302 cm^{-1} . The position of the second new vibrational band is identical to the OH vibration observed in solid state of water (ice)²³.

Crystallization of EDHA from D_2O instead of H_2O results in the disappearance of the above-mentioned specific OH stretch bands. As anticipated, the heavier deuterium atoms result in relatively weak O-D stretch vibrations in the region between 2550 and 2300 cm^{-1} ²³. A noticeable feature is that the ice-like OH stretch band at 3302 cm^{-1} remains present in the D_2O crystallized samples, indicating that no deuterium exchange of the hydroxylic protons occurs. The NH stretch vibration at 3302 cm^{-1} disappears and a doublet appears at 2473 and 2435 cm^{-1} , a typical observation originating in the deuterium exchange of the amide proton^{24,25}. This exchange is also depicted by the amide II combination band, where the C-N-H bend-in-plane vibration is replaced by a C-N-D bend-in-plane vibration at 1477 cm^{-1} . The spectra in Figure 3.6 demonstrate that crystallization in an aqueous environment induces weak antisymmetric and symmetric carboxylate vibrations at 1610 and 1442 cm^{-1} that are identically influenced by the introduction of the deuterium atoms (1601 and 1404 cm^{-1}). These observations strongly suggest the presence of water molecules in the vicinity of the carbonyl groups.

In assigning the vibrational modes in the FTIR spectra, especially in the high frequency region (from ~ 3600 to 2600 cm^{-1}) of the water crystallized samples, care has been taken to distinguish fundamental absorption bands from overtone or combination bands. Overtones are multiples of fundamental absorption bands, which means that the first overtone of a specific absorption band can be found by dividing the frequency by a factor 2. For secondary amides, such as polyamides and bisamide-diols, it is well accepted that the absorption band around 3080 cm^{-1} is an overtone band of the amide II absorption band at approximately 1560 cm^{-1} (C-N stretching and C-N-H bending in plane). Due to Fermi-enhancement with the fundamental NH stretch vibration at approximately 3300 cm^{-1} the amide II overtone band intensifies significantly. Fina and Yu assigned the shoulder present at the NH stretch band ($\sim 3300\text{ cm}^{-1}$) to a combination band of the amide I (CO stretch absorption) and the amide II vibrations²⁶. The decrease in absorption upon crystallization from deuterium oxide, where the amide protons are replaced by deuterons reducing the amide II absorption, support the overtone and combination band assignments (Table 3.3).

To gain further insight into the bound water and its influence on the conformation of the EDHA molecules polarized FTIR microscopy is performed on single crystals of EDHA grown from water. To recall, a detailed study performed by optical microscopy conclusively showed alignment of chains parallel to the crystal surface. Figures 3.7a,b represents polarized FTIR spectra, parallel and perpendicular to the molecular chains in a single crystal. Subtracted spectrum of the polarized FTIR is also shown in the figures and highlights the anisotropic vibrations present in the single crystals. The NH stretch band, which vibrates in strong polarization direction, appears well resolved at 3294 cm^{-1} in the subtracted H_2O spectrum. The subtracted spectrum also shows NH stretch vibration at 3332 cm^{-1} . Shift of the NH stretch band to higher wavenumber, 3332 cm^{-1} , suggests weakening of the interchain/intrasheet hydrogen bonding in the crystal lattice of water crystallized EDHA. It is to be noted that the two different NH stretch bands featuring in the subtracted spectrum are positioned in the opposite polarization directions. This distinction is likely to arise due to the presence of the NH moieties in two different chemical environments, a point to which we will come later.

In the same spectrum sharpening of the amide II band (1563 cm^{-1}), the amide III (1280 cm^{-1}), and the amide V bands (682 cm^{-1}) is also observed. The sharpening of bands suggest restricted environment for the NH moiety. These results when combined with the weakening of the interchain/intrasheet hydrogen bonding suggests restricted mobility in the dimensional space (i.e., bending in plane, out of plane scissoring) while free motion along the stretch direction remains.

As reported by Cooper et al. linearly aligned hydrogen bonds in nylons with maximum hydrogen bonding efficiency induce an equal polarization direction for the NH and carbonyl stretch vibrations. These stretch vibrations occur synchronically²⁷, where the synchronization arises due to the presence of interchain/intrasheet hydrogen bonding. Unlike the observations made by Cooper et al. on the single crystals of nylons, in the water

crystallized EDHA the NH stretch band at higher wavenumber (3332 cm^{-1}) shows vibration in opposite direction to the carbonyl stretch mode. These observations indicate the influence of the water molecule(s) present in the vicinity of carbonyl groups on shielding of the hydrogen bonding between the amide motifs of the adjacent chains.

It is anticipated that the shielding of the hydrogen bonding will influence the conformational changes. It is also to be realized that two different OH vibrational modes exist, one resembling a loose liquid like packing (3401 cm^{-1}) and the other a restricted solid like packing of the water molecules (3302 cm^{-1}). The origin of the loose and the restricted OH vibrations, off which the latter seems to be unaffected by the presence of heavy deuterium atoms, will be discussed in the following section. A closer look at the vibrational spectrum of the water crystallized EDHA and its comparison with the melt crystallized EDHA shows some differences in the hydroxylic OH stretch vibrations on the surface of the unit cell, for the water crystallized EDHA 3296 cm^{-1} , 3401 cm^{-1} and for the melt crystallized EDHA 3148 cm^{-1} . These differences tend to be localized to an extent that the adjacent COH vibration (1022 cm^{-1}), which shows restricted mobility by the narrow bandwidth, does not show any noticeable shift in wavenumber. Conformational changes arising due to all these complexities are summarized below.

In the water crystallized sample the presence of the $\alpha_{\text{N}}\text{CH}_2$ and $\alpha_{\text{C}}\text{CH}_2$ scissoring band at 1480 and 1432 cm^{-1} respectively together with the symmetric $\text{CC}=\text{O}$ stretch vibration at 957 cm^{-1} represent trans conformations for the methylene-amide couplings on either side of the amide moieties. These observations are in agreement with the lattice parameters calculated in our previously reported study that also emphasizes trans conformations for the amide-aliphatic couplings¹⁵. The high crystalline order and rigidity in the aliphatic segments, expressed by the well resolved antisymmetric CH_2 stretch vibrations, fit with the relatively low CH_2 scissoring absorptions in the 1500 to 1400 cm^{-1} region. The antisymmetric and symmetric αCH_2 stretch vibrations, in particular the α_{N} methylene units (2979 and 2897 cm^{-1}), are positioned at relatively high wavenumber and localized in a strong polarization direction. These findings stress that the presence of water in the vicinity of the amide motifs strongly affects the neighboring αCH_2 conformations.

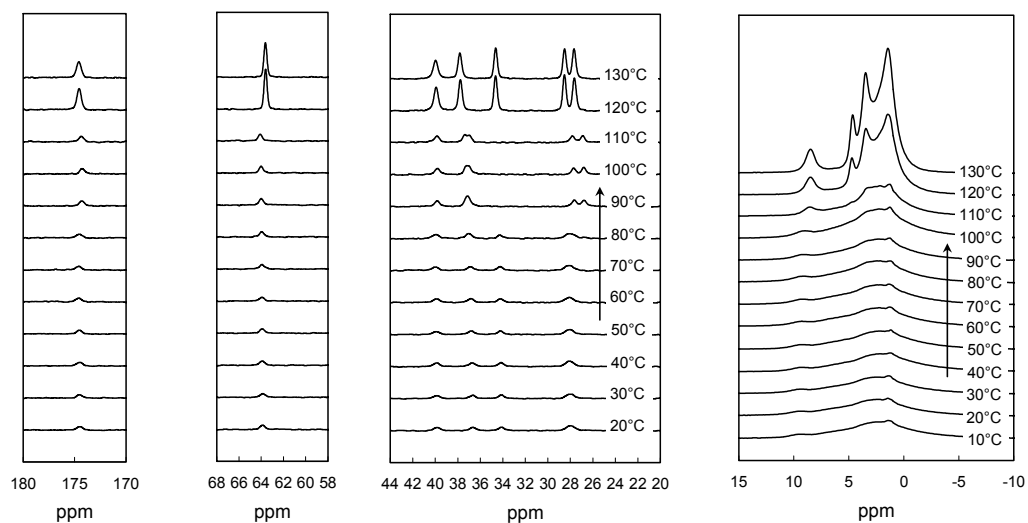
3.3.3 The migration of water molecules; a crystal transformation

From the observations reported in the section above it is evident that the water molecules reside within the crystal lattice of EDHA crystallized from the superheated state of water, influencing hydrogen bonding. Keeping our thermodynamic study in mind, the disappearance of the endo- and exothermic peaks at 95 and $83/59^\circ\text{C}$ respectively on sequential heating and cooling imply the metastable nature of these crystals prior to their irreversible transformation into a thermodynamically stable phase. On heating the stable crystals a crystal-to-crystal transition occurs at 111°C that is besides fully reversible on

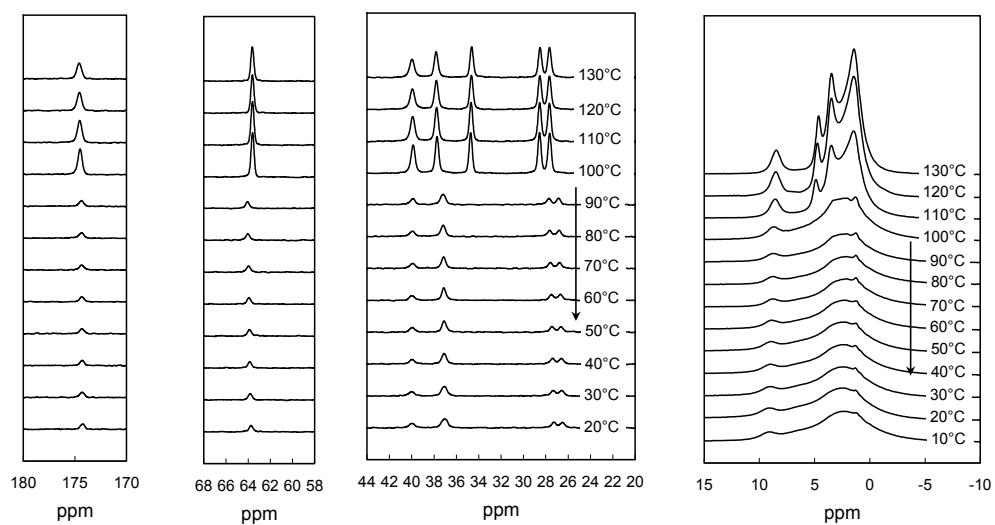
cooling (103°C). The crystal transformation from the metastable EDHA crystals into the thermodynamically stable state is shown by the DSC trajectories in Figure 3.2. Applying a heating rate of 10°C/min, it was furthermore concluded that the metastable crystals directly adopt the high temperature phase during the endothermic transition at 95°C, witnessed by time-resolved XRD measurements as well¹⁵. However, annealing the metastable crystals at 100°C in the DSC apparatus also results in the formation of the stable crystals with a transition temperature of 111°C and demonstrates the kinetic nature of the crystal transformation. In order to depict the metastable nature of the EDHA crystals obtained from the superheated state of water, temperature dependent solid state ¹H and ¹³C NMR and FTIR studies are discussed below.

The observation of two transitions at 95 and 111°C on heating in the NMR and FTIR spectra stress the coexistence of the metastable and thermodynamically stable crystals during the presented temperature cycle¹⁵. Thus, the temperature profile studied for conformational purposes is represented by DSC trace 2 in Figure 3.2. Because of the experimental time scale in the ¹³C NMR experiments, that is, an acquisition time of ~120 min, the endothermic transition at 95°C is already observed at 90°C. During the respective transition the intensities in both the ¹H MAS and ¹³C CP-MAS spectra hardly change. This observation, strengthened by the absence of the ¹³C signal for gauche conformers around 34.6 ppm, suggests that the 95°C transition is likely to arise from differences in chain packing, though the thermodynamic and structural studies have shown the transition to originate in enhanced mobility. On heating the efficiency in electron exchange between adjacent amide motifs generally decreases, weakening the interchain/intrasheet hydrogen bonding¹⁸. The ¹³C carbonyl signal however, shifts from 174.4 ppm at 20°C to 174.2 ppm at 100°C (Table 3.1) and indicates that the carbon nuclei of the carbonyl groups are less shielded after the 95°C transition. The amide ¹H signal on the other hand shifts from 9.4 ppm at 20°C to 8.7 ppm at 100°C and does match the anticipated changes in the chemical shift on heating, though the difference is relatively large to result from the weakening of interchain/intrasheet hydrogen bonding only. The presence of water molecules in the vicinity of the amide motifs may explain these contradictory findings in hydrogen bonding and will be further addressed in the section on FTIR spectroscopy below.

Upon further heating through the endothermic transition at 111°C, the appearance of the ¹³C signal at 34.6 ppm and the evident increase in intensities suggests that the transition is initiated by thermally induced gauche conformers. The solid state ¹H MAS and ¹³C CP-MAS spectra of the EDHA crystals obtained from the melt and the superheated state of water at 130°C are highly identical. The ¹³C carbonyl signal however, which for both crystals is positioned in a similar chemical environment at 174.6 ppm, shows a significant increase in the signal intensity. Besides, during the 111°C transition the amide ¹H signal shifts to lower chemical shift, from 8.9 to 8.6 ppm, whereas the carbonyl ¹³C signal increases from 174.3 to 174.6 ppm, both in accordance with a decrease in hydrogen bonding efficiency.



Chemical shift



Chemical shift

Figure 3.5: Solid state ^1H MAS (15 to -10 ppm) and ^{13}C CP-MAS spectra (180 to 20 ppm) for water crystallized EDHA during the initial heating (upper) and cooling (lower) run.

The transition from the metastable crystal into a thermodynamically stable crystal with an endothermic transition at 111°C goes along with several irreversible conformational changes on cooling. The shift of the amide proton signal from 9.4 to 9.1 ppm and the ^{13}C carbonyl signal from 174.5 to 174.3 ppm indicate increased shielding of the amide protons and the carbonyl carbon nuclei by surrounding electrons. These observations suggest establishment of interchain/intrasheet hydrogen bonding without hindrance of water molecules near the amide motifs. Conformational changes were also observed in the aliphatic segments of the molecule. Whereas the $\alpha_{\text{N}}^{13}\text{C}$ and $\omega_{\text{C}}^{13}\text{C}$ methylene signals do not change, the crystal transformation entails a shift in the $\alpha_{\text{C}}^{13}\text{C}$ methylene signal from 36.7 to 37.1 ppm and more changes in the aliphatic ^{13}C signals from 34.1 and 30.0 ppm to a doublet at 27.3 and 26.5 ppm. The strong resemblance of these ^1H and ^{13}C spectra with the NMR spectra at 100°C during the first heating run shows that within the experimental time scale the metastable phase transforms in the thermodynamically more stable state at 100°C.

Table 3.3: FTIR spectral vibrations of EDHA single crystals grown from superheated water at 5°C before and after (*) the initial temperature cycle ($s = \text{strong}$, $m = \text{medium}$, $w = \text{weak}$, $v = \text{variable}$).

band frequencies (cm^{-1})		relative intensity	band assignment
5°C	5°C*		
3401	-	w	OH stretch vibration; H-bonded like in liquid H_2O
3332	-	m	NH stretch vibration; rel. weakly H-bonded
3302	3294	s	OH stretch vibration; H-bonded like in ice
3296	3239	s/m	NH stretch vibration; H-bonded
3211	3216	m	Amide I and Amide II combination band
3085	3086	m	Amide II overtone band
2979	2971	w	$\alpha_{\text{N}}\text{CH}_2$ antisym. stretch vibration in constrained environment
2941/ 2926	2938	m/s	CH_2 antisym. stretch vibration
2897	2870	w/m	$\alpha_{\text{N}}\text{CH}_2$ sym. stretch vibration in constrained environment
2861/ 2855	2858	m	CH_2 sym. stretch vibration
1632	1646	s	Amide I: C=O stretch vibration
1610	-	w	COO $^-$ antisym. stretch vibration
1562	1563	s	Amide II: C-N stretch and C-N-H bending in-plane vibration
1480	-	w	CH_2 scissoring next to NH ($\alpha_{\text{N}}\text{CH}_2$) in trans conformation
1442	-	w	COO $^-$ sym. stretch vibration
1432	1413	m/s	CH_2 scissoring next to C=O ($\alpha_{\text{C}}\text{CH}_2$) in trans conformation
1280	1253/ 1244	s/m	Amide III: C-N stretch and C-N-H bending in-plane vibration coupled to skeletal carbon ($\alpha_{\text{C}}\text{CH}_2$)
1022	1053	m/s	C-OH out-of-phase stretch vibration
957	944	m	CC=O sym. stretch vibration
-	721	m	most in-phase CH_2 rocking mode in triclinic packing
682	-	w	Amide V: NH out-of-plane scissoring

In order to reveal the origin of the crystalline transformation, which on the basis of our thermodynamic studies seems to be related to the exothermic transition at 83°C on cooling (Figure 3.2), detailed FTIR studies are reported below. In contradiction to the high temperature phase of melt crystallized EDHA, where the interchain/intersheet diffraction signals approach or diverse from one another in a temperature dependent fashion, the water crystallized samples show no change in the diffraction signals upon heating above 111°C. Though no crystallographic changes are observed in the water crystallized EDHA, conformational changes are observed in NMR and FTIR spectroscopy.

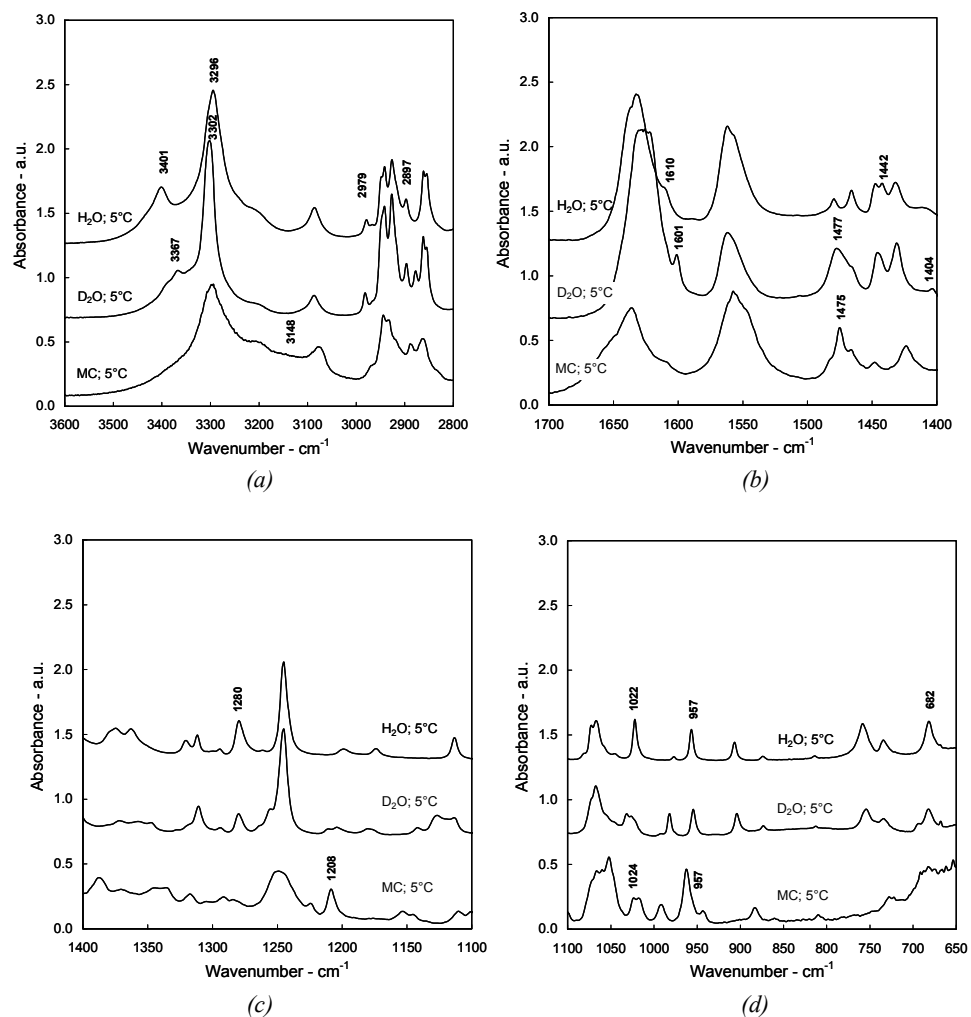


Figure 3.6: A comparison of melt (MC), D₂O and H₂O crystallized EDHA at 5°C by FTIR spectroscopy, depicting the influence of the H₂O and D₂O molecules in the crystal lattice on the vibrational modes.

The conformational changes are similar to the changes observed in the melt crystallized samples. In comparison with the melt crystallized sample the amide III and the symmetric CC=O stretch vibrations shift to lower frequencies, namely 1243 and 957 cm^{-1} respectively. The shift to lower frequencies in these coupling vibrations arises from restrictions in the vibrational modes and indicates less influence of the thermally induced gauche conformers in the aliphatic segments on the out-of-plane wagging of the amide motifs. The main differences between melt and water crystallized EDHA are depicted in the hydroxylic vibrations such as the low in-phase OH stretch and bending vibrations at 1057 and 1380 cm^{-1} , respectively. Above 111°C, the OH stretch vibrations at 3401 cm^{-1} , resembling the OH stretch of liquid water, disappear while the ice-like OH stretch vibration remains at 3303 cm^{-1} . The local restrictions in the hydroxylic end groups at high temperatures suggest the retention of highly efficient electron exchange between the hydroxylic end groups. Moreover, the ^1H NMR spectra show subtle, though salient changes for the hydroxylic proton that shifts from 4.9 ppm in the case of melt crystallized EDHA to 4.7 ppm for water crystallized EDHA at 130°C (Table 3.1). The decrease in chemical shift means that the crystallization from superheated water induces increased shielding of the hydroxylic proton nuclei. The restricted environment of the hydroxylic groups in the water crystallized sample might explain the diminishing effect of the gauche conformers on the out-of-plane wagging of the amide motifs. Less out-of-plane wagging vibrations, also witnessed by the low intensities of the stronger bonded NH proton (8.5 ppm) and the carbonyl ^{13}C (174.5 ppm), explains the retained interchain/intrasheet hydrogen bonding at 130°C. The changes in the hydroxylic environment are likely to influence the phase transitions on cooling (Figure 3.2). In the following paragraph the conformational changes occurring during the reorganization of the metastable phase (water crystallized) and its transformation into the thermodynamically stable triclinic phase will be highlighted¹⁵.

Similar to the solid state ^1H and ^{13}C NMR, FTIR spectroscopy cannot be applied to follow the in situ structural changes occurring during the transition of the metastable crystal to the thermodynamically stable phase as revealed by X-rays¹⁵. The transition at 95°C shows the disappearance of the liquid type of OH stretch vibration at 3401 cm^{-1} and the (anti)symmetric carboxylate vibrations at 1610 and 1442 cm^{-1} . This suggests the loss of water molecules in the vicinity of the amide motifs (Figure 3.7). At the same time the lesser bound NH stretch vibration at 3332 cm^{-1} disappears, while the hydrogen bonded NH stretch vibration shifts to 3239 cm^{-1} , indicative for more effective interchain/intrasheet hydrogen bonding. Moreover, the hydrogen bonded NH stretch and CO stretch vibrations (amide I) at 1646 cm^{-1} are envisaged in equal polarization direction and vibrate synchronically. In solid state NMR, the migration of the water molecules gives rise to a decrease in the ^{13}C carbonyl (174.3 ppm) and the ^1H NH (9.1 ppm) chemical shifts.

With the migration of water molecules from the amide moieties the strong hydrogen bonded environment for the hydroxyl groups (3301 cm^{-1}) prevails at 95°C. On cooling the hydrogen bonding efficiency increases, resulting in a lower wavenumber, namely 3294 cm^{-1}

¹. In melt crystallized EDHA the hydroxylic end groups form (O-H...O-H...)_n chains by cooperative configurational hydrogen bonding and promote an alternating tilt of the molecules within the hydrogen bonded sheets. The resulting OH stretch vibration at 3148 cm⁻¹ is indicative for the highly efficient electron exchange between the oxygen as electron

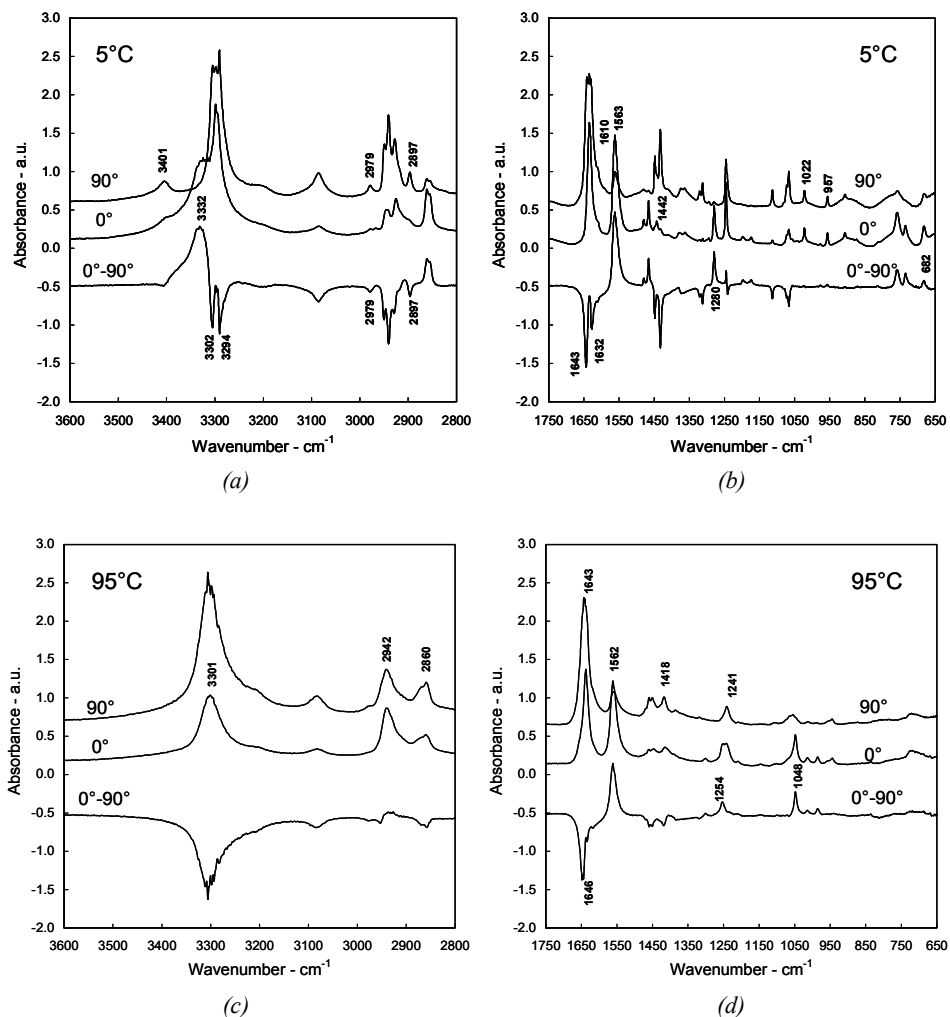


Figure 3.7: The migration of water molecules and its implications on hydrogen bonding followed by polarized FTIR spectra, parallel (90°) or perpendicular (0°) to the molecular chain, during the first heating profile at 5°C (a, b) and 95°C (c, d). Subtraction spectra (0°-90°) highlight the vibrational polarization directions.

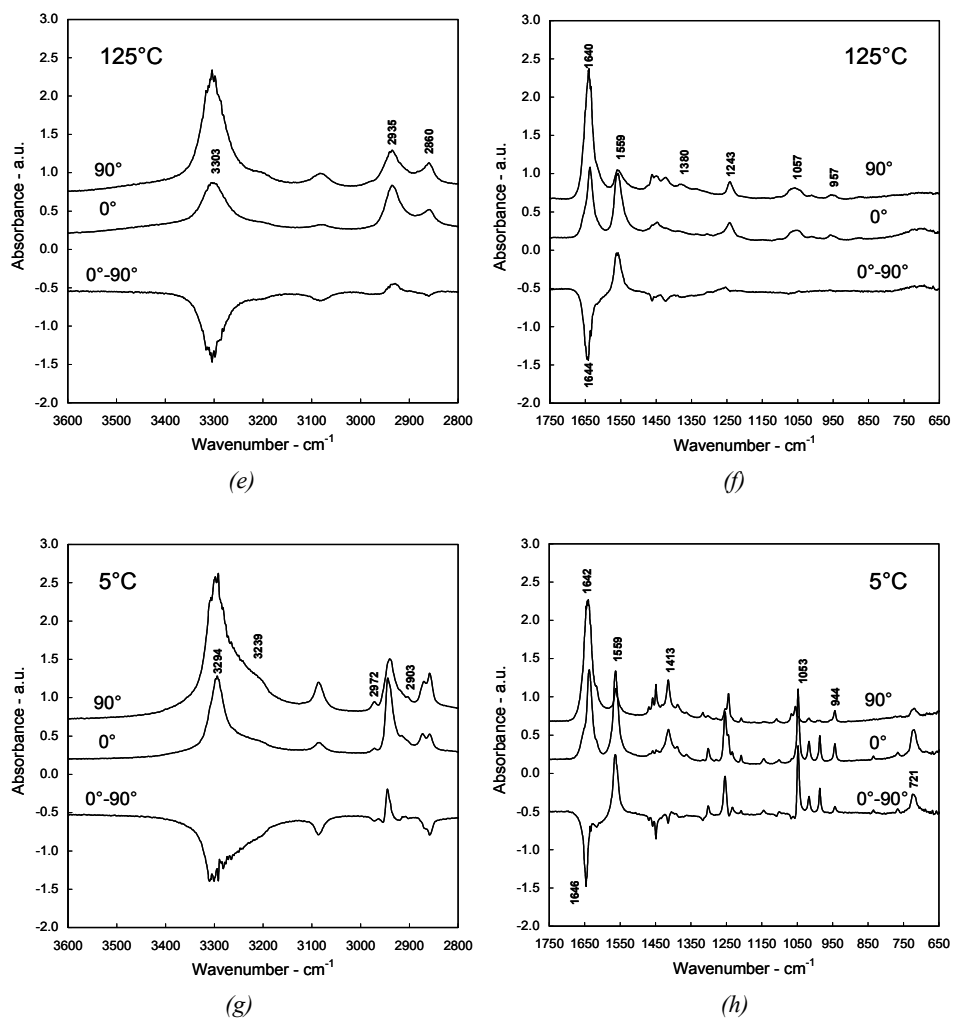


Figure 3.7 (continued): The migration of water molecules and its implications on hydrogen bonding by polarized FTIR spectra, parallel (90°) or perpendicular (0°) to the molecular chain, during the first heating profile at 125°C (e, f) and after successive cooling to 5°C (g, h). The subtraction spectra (0° - 90°) highlight the vibrational polarization directions.

donor and the proton as electron acceptor. The configurational hydrogen bonded structure perishes at 63°C in melt crystallized EDHA with the disappearance of the OH stretch band at 3148 cm^{-1} and the appearance of an OH stretch band at 3394 cm^{-1} , attributed to conformational OH hydrogen bonding. In the water crystallized EDHA the hydroxylic hydrogen bonds exist even after the phase transition at 111°C , though positioned at higher wavenumber (3294 cm^{-1}). Besides the peak position also the narrow peak width, arising

from rigid structures, matches the OH stretch vibrations in ice that in the biosphere occurs in a hexagonal packing to maximize the intermolecular hydrogen bonding efficiency^{23,28}. These findings in combination with the electron rich environment, in which the hydroxylic protons are located at 130°C, indicate that crystallization from the superheated state of water entails highly efficient hydroxylic hydrogen bonding. The formation of these hydrogen bonds in a potential hexagonal pattern at the interphase of adjacent unit cells (*ab* plane), requires an angle γ of approximately 60° as determined by WAXD in chapter 2¹⁵.

The coexistence of planar directed amide-amide and tetrahedral directed hydroxylic hydrogen bonding demands unfavorable conformations along the EDHA molecules. However, the presence of water molecules that shield the amide moieties during crystallization erase the conformational limitations. Due to the absence of preferential order in interchain/intrasheet hydrogen bonding between the amide motifs, the conformational “freedom” of the hydroxyl groups enables the formation of ideally aligned hydrogen bonded structures. The electron exchange between water molecules and the amide moieties templates the crystallization to form cooperatively stabilized EDHA crystals.

3.4 Conclusions

In melt crystallized EDHA at temperatures below 63°C the cooperative arrangement of hydrogen bonded (O-H···O-H···)_n chains in combination with retaining electron exchange between the amide moieties introduces non-trans aliphatic diamine conformation and requires an alternative tilt of the aligned molecules in adjacent sheets. As temperature increases, weakening of the extraordinary strong hydroxylic hydrogen bonding entails rotational motion that is responsible for the change of configurational to conformational hydrogen bonding. A continuous exchange of covalent and hydrogen bonds vanishes and the hydroxyl groups rotate from one hydrogen bonding position into the other. Due to a simultaneous release of the constrained amide- α_C methylene conformations ideally aligned hydrogen bonding establishes, resulting in a new triclinic packing (Figure 3.8). More and more methylene gauche conformers on further heating transfer the crankshaft type of motion to the amide motifs. The out-of-plane wagging vibrations of the amide motifs go along with a second solid state crystalline transition at 85°C, after which the interchain/intrasheet and interchain/intersheet distance of the novel triclinic phase approach one another in a typical nylon fashion prior to melting. Conclusively, though a Brill transition was not identified, a delicate balance between conformational (dis)order in the methylene segments and hydrogen bonding efficiency between the hydrogen bonded moieties validates the role of N,N'-1,2-ethanediyl-bis(6-hydroxy-hexanamide) as a model.

Crystallization of EDHA from the superheated state of water results in the formation of a thermodynamically metastable phase, in which water molecules near the amide moieties prevent the establishment of interchain hydrogen bonding as illustrated in Figure

3.9. Because of the shielding of amide-amide hydrogen bonding, erasing the conformational limitations of the planar amide motifs during crystallization, trans methylene conformations along the entire molecules coexist with strong intermolecular hydroxylic hydrogen bonding in the metastable crystals. By annealing above 95°C or sequential temperature cycles through the endothermic transition at 95°C on heating the metastable crystals transform irreversibly into thermodynamically more stable crystals. During the crystal transformation the water molecules migrate from the amide motifs. Since the highly efficient hydrogen bonding between highly ordered hydroxylic end groups decreases the effect of the thermally triggered rotating gauche conformers on the out-of-plane wagging vibrations of the amide moieties, the crystal to crystal transition occurs at 111°C. The versatile nature of water molecules, especially with respect to its hydrogen bonding geometries, provide ideal electron exchange processes in shielding and mediating intermolecular hydrogen bonding during crystallization from the superheated state of water.

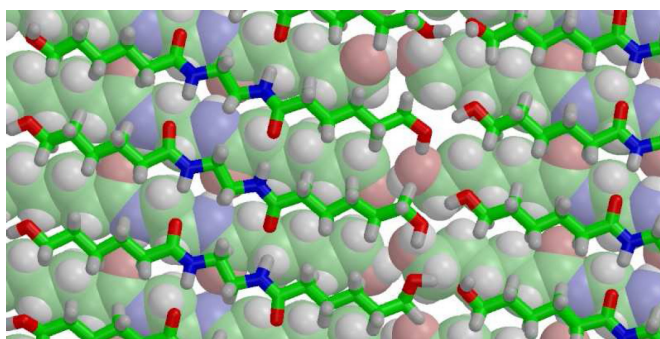


Figure 3.8: Top view of two hydrogen bonded sheets in EDHA crystallized from the melt at 55°C as revealed by molecular dynamics simulations using the OPLS-AA force field (Courtesy Berk Hess)²⁹.

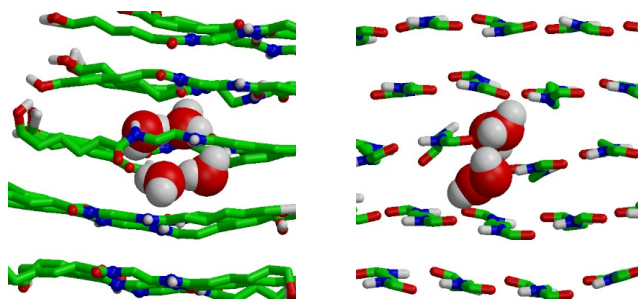


Figure 3.9: Two projections of stacked hydrogen bonded sheets at 77°C, accommodating a stable cluster of 4 water molecules satisfying all hydrogen bonding positions as revealed by molecular dynamics simulations using the OPLS-AA force field (Courtesy Berk Hess)²⁹.

3.5 References

1. Jones, N. A.; Atkins, E. D. T.; Hill, M. J.; Cooper, S. J.; Franco, L. *Macromolecules* **1996**, *29*, 6011-6018.
2. Jones, N. A.; Atkins, E. D. T.; Hill, M. J.; Cooper, S. J.; Franco, L. *Polymer* **1997**, *38*, 2689-2699.
3. Jones, N. A.; Atkins, E. D. T.; Hill, M. J.; Cooper, S. J.; Franco, L. *Macromolecules* **1997**, *30*, 3569-3578.
4. Jones, N. A.; Cooper, S. J.; Atkins, E. D. T.; Hill, M. J.; Franco, L. *J. Polym. Sci. Part B.: Polym. Phys.* **1997**, *35*, 675-688.
5. Yoshioka, Y.; Tashiro, K. *Polymer* **2003**, *44*, 7007-7019
6. Nair, S. S.; Ramesh, C.; Tashiro, K. *Macromolecules* **2006**, *39*, 2841-2848.
7. Yoshioka, Y.; Tashiro, K.; Ramesh, C. *Polymer* **2003**, *44*, 6407-6417.
8. Yoshioka, Y.; Tashiro, K. *J. Phys. Chem. B.* **2003**, *107*, 11835-11842.
9. Vinken, E.; Terry, A. E.; Hoffmann, S.; Vanhaecht, B.; Koning, C. E.; Rastogi, S. *Macromolecules* **2006**, *39*, 2546-2552.
10. Brill, R. J. *Prakt. Chem.* **1942**, *161*, 49-64.
11. Challa, G. *Plastica* **1969**, *22*, 204-208.
12. Rastogi, S.; Terry, A. E.; Vinken, E. *Macromolecules* **2004**, *37*, 8825-8828.
13. Vinken, E.; Terry, A. E.; Van Asselen, O.; Spoelstra A. B.; Graf, R.; Rastogi, S. *Langmuir* **2008**, *24*, 6313-6326.
14. Jedlovsky, P.; Brodholt, J. P.; Bruni, F.; Ricci, M. A.; Soper, A. K.; Vallauri, R. *J. Chem. Phys.* **1998**, *108*, 8528-8540.
15. Harings, J. A. W.; Van Asselen, O.; Graf, R.; Broos, R.; Rastogi, S. *Cryst. Growth Des.* **2008**, *8*, 2469 -2477.
16. Katayama, S.; Horikawa, H. *J. Appl. Polym. Sci.* **1971**, *15*, 775-796.
17. Langer, B.; Schnell, I.; Spiess, H. W.; Grimmer, A. R. *J. Magn. Reson.* **1999**, *138*, 182-186.
18. Ando, I.; Asakura, T. In *Solid State NMR of Polymers, Studies in Physical and Theoretical Chemistry*, Vol. 84, **1998**.
19. Lin-Vien, D.; Colthup, N. B.; Fateley, W. G.; Grasselli, J. G. In *The Handbook of Infrared and Raman Characteristic Frequencies of Organic Molecules*, Academic Press: SanDiego, **1991**.
20. Jeffrey, G. A.; Saenger, W. In *Hydrogen Bonding in Biological Structures*, Springer-Verlag Berlin Heidelberg, **1994**.
21. Tashiro, K.; Sasaki, S.; Kobayashi, M. *Macromolecules* **1996**, *29*, 7460-7469.
22. Rotter, G.; Ishida, H. *J. Polym. Sci. Part B.: Polym. Phys.* **1992**, *30*, 489-495.
23. Zelent, B.; Nucci, N. V.; Vanderkooi, J. M. *J. Phys. Chem. A.* **2004**, *108*, 11141-11150.
24. Grdadolnik, J.; Maréchal, Y. *Appl. Spectrosc.* **2005**, *59*, 1347-1356.

-
25. Grdadolnik, J.; Maréchal, Y. *Appl. Spectrosc.* **2005**, *59*, 1357-1364.
 26. Fina, L. J.; Yu, H. H. *J. Polym. Sci. Part B.: Polym. Phys.* **1992**, *30*, 1073-1080.
 27. Cooper, S. J.; Coogan, M.; Everall, N.; Priestnall, I. *Polymer* **2001**, *42*, 10119-10132.
 28. Jeffrey, G.A. In *An Introduction to Hydrogen Bonding*, Oxford University Press: New York, **1997**.
 29. Hess, B.; Harings, J. A. W.; Rastogi, S.; Van der Vegt, N. F. A. *J. Phys. Chem. B.* **2009**, *13*, 627-631.



Chapter 4*

Erasing conformational limitations in N,N'-1,4-butanediyl-bis(6-hydroxy-hexanamide) crystallization from the superheated state of water

Aliphatic polyamides consist of regularly distributed amide moieties located within an aliphatic chain, off which the segment length and polarity can be varied. The crystallization, and hence the eventual performance of the material can be tailored by changing the aliphatic lengths, and thus the hydrogen bonding density, and the polarity of the chain. In the present chapter, N,N'-1,4-butanediyl-bis(6-hydroxy-hexanamide) crystallized either from the melt or from the superheated state of water is investigated. A comparison with N,N'-1,2-ethanediyl-1,2-bis(6-hydroxy-hexanamide) reveals the role of the hydrogen bonding density on the accommodation of water molecules in amide based crystals grown from the superheated state of water. However, WAXD, FTIR and solid state ^1H and ^{13}C NMR spectroscopy reveal hydrogen bonding between the structural planes of amide moieties, while aliphatic polyamides and N,N'-1,2-diethyl-bis(6-hydroxy-hexanamide) feature hydrogen bonds that reside within the structural amide planes only. As a consequence, the role of N,N'-1,4-butanediyl-bis(6-hydroxy-hexanamide) crystals as a model system for polyamide 4y polymers is questionable. However, the thermodynamic and structural behavior as function of temperature is determined by a balance between thermally introduced gauche conformers and hydrogen bonding efficiencies. These crystals enable a thorough investigation in the effect of superheated water on the crystallization of these uniquely hydrogen bonded molecules. Crystallization from the superheated state of water results in denser molecular packing and enhanced hydrogen bonding efficiencies. The induced spatial confinement hinders molecular motion upon heating and thermodynamically more stable crystals are observed. Although the amide-hydroxyl hydrogen bonded crystals do not favor the accommodation of physically bound water molecules in the lattice, saturation of the amide motifs during crystallization erases conformational restrictions of the planar amide moieties that facilitates maximum hydrogen bonding efficiencies in the final lattice.

* Partially reproduced from Harings, J.A.W.; Yefeng, Y.; Van Asselen, O.; Graf, R.; Broos, R.; Rastogi, S., *Langmuir* **2009**, subm.

4.1 Introduction

The presence of water molecules in biological structures, especially in proteins and nucleic acids, is crucial in all kind of sophisticated mechanisms that sustain life. Dependent on the hydrogen bonding geometries and the location of water molecules, biological structures can be stabilized enthalpically or entropically¹. This demonstrates the important role of water molecules that goes even beyond stabilization. During evolution water has adopted an active role in self-assembly phenomena such as protein folding, protein-protein recognition and protein-DNA binding². Here, van der Waals interactions, hydrogen bonding, electrostatic and hydrophobic interactions are the key to sequence-specific DNA recognition by proteins. However, prior to the influence of the direct interactions, water molecules indirectly mediate the recognition and specificity, acting as a guide mapping unfavorable electrostatic forces and hydrogen bonding.

Despite the versatility of water, which is exquisitely used in nature to fulfill specific tasks, the use of water in synthetic polymeric structures, such as polyamides, has been scarcely exploited. In fact, it is the unique behavior of water that also facilitates the dissolution of polyamides in water at elevated temperature and pressure as reported by Rastogi and Vinken et al.^{3,4}. The disruption of the percolating hydrogen bonded network and the weakening of the van der Waals forces result in highly mobile water molecules. Simultaneously, close to the Brill transition in polyamides, the efficiency in electron exchange between amide moieties in adjacent crystal stems decreases⁵⁻⁷. In spite of the reduction in hydrogen bonding efficiency, the water and amide protons, which are like any hydrogen bonded proton in electron deficiency, prevail their quest for free electrons present in the carbonyl moieties and the water molecules. Consequently the electron exchange between mobile water molecules and amide motifs perturbs the interchain/intrasheet hydrogen bonding, resulting in the dissolution of polyamides in superheated water^{3,4,8}.

Upon cooling crystallization occurs above the boiling point of water, where the continuous electron exchange between the water molecules and the amide motifs leads to the entrapment of water molecules within the crystal lattice⁴. Since polyamides are semicrystalline in nature the use of a low molecular weight symmetrical bisamide-diol model compound was proposed in chapters 2 and 3, evading the complications of an amorphous component, to investigate the location of water molecules and its implications on hydrogen bonding within the crystalline domains^{9,10}.

It was concluded that a delicate balance between thermally induced gauche conformers and hydrogen bonding efficiency between amide motifs, the same balance in which the Brill transition originates, triggers crystalline phase transitions and validates the role of N,N'-1,2-ethanediyl-bis(6-hydroxy-hexanamide) as a model. Crystallization from the superheated state of water results in metastable crystals, where water molecules hinder the establishment of interchain/intrasheet hydrogen bonding. Shielding of the amide moieties erases the planar restrictions during crystallization and facilitates the coexistence

of all-trans methylene conformations and ideally aligned hydroxylic hydrogen bonds. The enhanced efficiency in electron exchange between adjacent hydroxyl groups lowers the effect of the thermally induced gauche conformers on the out-of-plane wagging vibrations of the amide motifs. Hence, in comparison with the melt crystallized sample the crystal-to-crystal transition, which originates from the balance between gauche conformers and hydrogen bonding efficiencies, shifts to a significantly higher temperature. The presence of water molecules near the amide moieties results in metastable crystals with a reduced crystal-to-crystal transition temperature, via which the metastable crystals transform irreversibly into the thermodynamically more stable structure. The migration of water molecules from the amide motifs, enabling interchain/intrasheet hydrogen bonding on cooling, forms the origin of the crystal transformation.

Polyamides feature variations in hydrogen bonding densities by changing the length of the aliphatic segments that are connected by amide motifs in either a symmetrical or anti-symmetrical way¹¹⁻¹⁵. In this study it is aimed to investigate the balance between the molecular motion in the aliphatic sequences on both sides of the amide moieties and the stability and effect of water-amide interactions. Another bisamide-diol, namely N,N'-1,4-butanediyl-bis(6-hydroxy-hexanamide), Figure 4.1, is introduced and compared with the previously reported N,N'-1,2-ethanediyl-bis(6-hydroxy-hexanamide)^{9,10}, both representing the crystalline domains in the polyamide XY family. Thermodynamic, structural and conformational changes are studied using DSC, time-resolved WAXD, FTIR spectroscopy and solid state ¹H and ¹³C NMR spectroscopy.

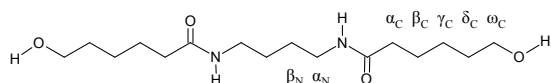


Figure 4.1: Chemical structure of N,N'-1,4-butanediyl-bis(6-hydroxy-hexanamide), in which the individual CH₂ groups are labeled.

4.2 Experimental section

4.2.1 Materials

1,4-Diaminobutane and ϵ -caprolacton were purchased from Aldrich, The Netherlands. Tetrahydrofuran (THF) and acetonitril, both of analytical grades, were obtained from Biosolve, The Netherlands. N,N'-1,4-butanediyl-bis(6-hydroxy-hexanamide), from now on denoted as BDHA and sketched in Figure 4.1, was synthesized according to the reaction scheme presented in Figure 4.2 using a similar procedure as described for N,N'-1,2-ethanediyl-bis(4-hydroxy-hexanamide), EDHA^{9,10,16}. A solution of ϵ -caprolacton (0.156 mol) in 37.5 mL of THF was added in 2 h to a solution of 1,4-

diaminobutane (0.080 mol) in 50mL THF. Subsequently, the mixture was stirred at 10°C for 3 days. After the THF was removed under reduced pressure, the precipitate was purified by successive recrystallization in an acetonitril/ water (7/1, v/v) solution at 5°C. Thermodynamic, structural and conformational aspects of melt and water crystallized BDHA were studied. Melt crystallized samples were obtained by cooling from melt at 10°C/min to 5°C. In a closed environment a part of the melt crystallized sample was dissolved in water at 100°C. The resulting water vapor pressure ensured dissolution in the superheated state of water. Upon cooling the aqueous solution, at a rate of 10°C/min, BDHA precipitated to form the water crystallized samples.

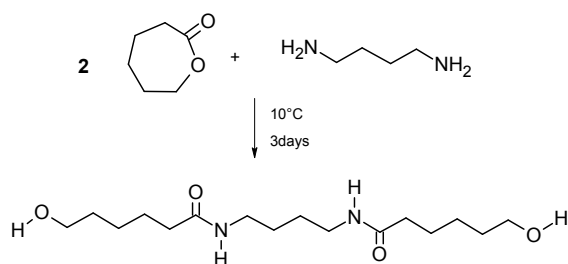


Figure 4.2: Synthesis of *N,N'*-1,4-butanediyl-bis(6-hydroxy-hexanamide).

4.2.2 Differential scanning calorimetry

Thermodynamic behavior of the melt and the water crystallized BDHA (10°C/min) was studied under nitrogen atmosphere by DSC using a TA Q1000 apparatus. In order to study the phase transitions accurately, the crystals were exposed to two initial heating and cooling profiles from -25 up to 125°C, followed by two cycles from -25 up to 175°C. The heating and cooling rate of all cycles was 10°C/min and 3 minutes of isothermal conditions were applied at the temperature limits.

4.2.3 Wide angle X-ray diffraction

Wide Angle X-ray Diffraction experiments were performed at the high resolution Materials Science beamline ID11, located at the European Synchrotron Radiation Facility (ESRF), Grenoble, France. Time-resolved measurements allowed us to investigate the structural changes within an experimental time-scale identical to the DSC measurements. Two-dimensional diffraction patterns were recorded using a Frelon 2D detector having 2048 x 2048 arrays of pixels with a pixel size of 46.8 x 48.1 μm, providing the high resolution required for accurate determination of the peak positions. Crystals grown from

water were placed in a 1 mm diameter Lindemann capillary and exposed to two temperature cycles, from -25 up to 125°C and two cycles from -25 up to 175°C using a Linkam TMS94 hotstage at a heating/cooling rate of 10°C/min. During the last temperature cycles the water crystallized samples were exposed to temperatures above the melting temperature (138°C). DSC measurements revealed that melting erases the specific thermodynamic behavior of BDHA crystals grown from the superheated state of water. As a result, the isotropic crystallization and successive phase transitions of the melt crystallized BDHA during the remaining temperature profile were monitored in-situ. A 25 keV ($\lambda = 0.0496$ nm) X-ray beam of 50 μm size was used and a two-dimensional diffraction patterns of 0.5 s exposure time were collected at every 6 seconds. To calibrate the sample-to-detector distance a lanthanum hexaboride standard was used. After correction for the absorption and air scattering, all diffraction patterns were integrated. TREOR 90, a general trial-and-error method for the ab initio indexing of powder patterns, using a space group of P-1, in combination with a Pawley refinement was used to assign the observed diffraction signals and lattice parameters of the different unit cells^{17,18}.

4.2.4 Optical microscopy

Morphological and structural changes of water and melt crystallized BDHA were observed by optical microscopy using a Zeiss Axioplan Imaging 2. Single BDHA crystals were exposed to two temperature cycles from 5 to 125°C and one cycle from 5 to 175°C using a linkam TMS94 hotstage at 10°C/min. Making use of crossed polarizers and a retardation plate (λ) for red wavelength, optical images were taken at every 10°C.

4.2.5 Fourier transfer infrared spectroscopy

Conformational changes of melt crystallized EDHA as well as single crystals grown from H₂O and D₂O were studied by FTIR spectroscopy. The crystals were placed on a zinc selenium disk and spectra were recorded on a Bio-Rad FTS6000 spectrometer equipped with a microscope with a resolution of 2 cm⁻¹ in transmission mode. Polarized FTIR was performed on single crystals to gain further insight in the orientation of the hydrogen bonded moieties on an atomistic level. Single crystals grown from water and heavy water were exposed to two initial temperature cycles from 5 to 125°C, followed by two cycles from 5 to 145°C. Spectra of the melt crystallized samples were recorded in a single temperature cycle from 5 to 175°C. For FTIR studies, the temperature cycles, characterized by a rate of 10°C/min, were controlled by a linkam TMS94 hotstage. At every 10°C the average of 100 FTIR spectra was recorded after 3 min of isothermal period.

4.2.6 Solid state nuclear magnetic resonance spectroscopy

Solid state ^1H and ^{13}C NMR spectroscopy was performed respectively on a Bruker Avance console operating at 700 MHz ^1H Larmor frequency and a Bruker DSX spectrometer with 500 MHz ^1H Larmor frequency at the Max Planck Institute for Polymer Research (MPI-P) in Mainz, Germany. For ^1H NMR measurements a zirconia rotor with 2.5 mm outer diameter, filled with either the melt or water crystallized sample, was placed in a commercial MAS probe and spun at 30 kHz. ^1H MAS spectra as well as two-dimensional Nuclear Overhauser Enhancement spectra (NOESY) were recorded in a temperature range from 20 up to 150°C. The known differences between bearing gas and sample temperatures have been taken into account¹⁹ and the corrected temperatures are given throughout the chapter. ^{13}C CP MAS NMR experiments in contrary were performed using rotors with 4mm outer diameter, spinning at 10 kHz MAS frequency and spectra were recorded at various temperatures, ranging from 20 to 130°C.

4.3 Results and discussion

4.3.1 Thermal motion and hydrogen bonding in melt crystallized BDHA

In order to reveal the influence of physically bound water molecules on hydrogen bonding and potential thermodynamic phase transitions, as observed in N,N' -1,2-diethylbis(6-hydroxy-hexanamide)^{9,10}, the balance between thermally triggered gauche conformers in the methylene segments and hydrogen bonding efficiencies in melt crystallized BDHA has to be well understood. Figure 4.3 shows the DSC thermogram of melt crystallized BDHA, which exhibits two transitions in the heating and cooling profiles. These observations differ from the EDHA results discussed in chapter 2 and 3, where three endothermic transitions on heating and three exothermic transitions on cooling were registered by DSC⁹.

The similar enthalpies for the first endothermic event T_{H1} at 79°C on heating and the second exothermic transition T_{C2} at 24°C on cooling (11.6 and 11.3 J/g respectively) suggest that both transitions arise from the same event that has moreover a high entropic barrier. Besides, it is to be noted that thermally triggered transitions were observed at similar temperatures in EDHA. The origin of the respective transitions in EDHA differed significantly in enthalpy and was assigned to two independent processes. The endothermic transition at 85°C arises from the introduction of gauche conformers initiating the out-of-plane wagging of the amide moieties, whereas the exothermic transition at 22°C upon cooling results from the formation of cooperative configurational hydroxylic hydrogen bonding. The melting of BDHA goes along with an endothermic transition T_{H2} at 137°C. The crystallization features several sharp exothermic transitions, where the total enthalpy

involved closely matches the enthalpy of melting, namely 132J/g. The multiple crystallization peaks most likely arise from separated drops of molten BDHA that crystallize individually at slightly different temperatures due to subtle variations in the heterogeneous nucleation process.

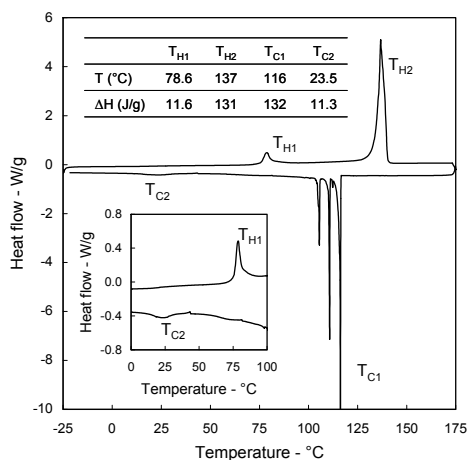


Figure 4.3: DSC thermogram of melt crystallized BDHA. In the table the transition temperatures and the corresponding enthalpies upon heating (T_{H1} and T_{H2}) and cooling (T_{C1} and T_{C2}) are listed. The inset shows a magnification to stress the low temperature transitions explicitly.

Temperature dependent WAXD experiments were performed to evaluate the potential as a model compound representing the crystalline domains in polyamides. To recapitulate, on heating polyamides weakening of the van der Waals forces induces an increase in the interchain/intersheet distance. Despite the out-of-plane wagging of the amide motifs, which is transferred from the gauche conformers in the methylene segments, the interchain/intrasheet hydrogen bonding prevails. In combination with the tendency of gauche conformers to migrate out of the lattice, hence introducing chain mobility along the *c*-axis, the interchain/intrasheet distance decreases. The temperature where the interchain/intrasheet and interchain/intersheet merge is referred as the Brill transition temperature²⁰. These characteristic structural changes can be followed in situ by time-resolved X-ray techniques.

Figure 4.4a shows the azimuthally integrated wide angle X-ray diffraction patterns of the melt crystallized sample on heating. By means of powder diffraction indexing, using the TREOR90 method and a Pawley refinement, the diffraction signals that represent the interchain/ intrasheet and interchain/intersheet distance were assigned and plotted as a function of temperature (Figure 4.4b). Upon heating, while the interchain/intrasheet distance in 4Y polyamides decreases significantly, as reported by Jones et al.¹¹⁻¹³, in the

melt crystallized samples the interchain/intrasheet diffraction signals 100 and 101 hardly change over the temperature range from 5 to 125°C. With the endothermic transition at 79°C the 100 and 101 diffraction signals, of 0.432 and 0.424 nm respectively, hardly change. These diffraction signals do not show any significant changes prior to melting. The signals related to the interchain/ intersheet distance however do change in analogical way to 4Y polyamides, where the interchain/intersheet distance increases progressively on heating. Up to the first endothermic transition at 79°C the 010 signal, which is the actual interchain/intersheet distance, remains constant and is superimposed by the interchain/intrasheet diffraction signal at 0.432 nm, while on heating from 5 to 75°C the 110 and 111 diffraction signals increase from 0.374 and 0.352 nm to 0.382 and 0.364 nm respectively. Above 79°C the interchain/intersheet diffraction signals, especially the 010 signal, increases considerably. Though the hydrogen bonded sheets are held together by van der Waals forces, the abrupt changes observed in the interchain/intersheet distances, and hence the endothermic transition at 79°C, are likely to arise from an increasing population of gauche conformers that weaken the secondary interactions between adjacent molecules. Upon cooling from the melt, the WAXD diffraction signals behave identically, indicating that the temperature dependent crystallographic changes are completely reversible.

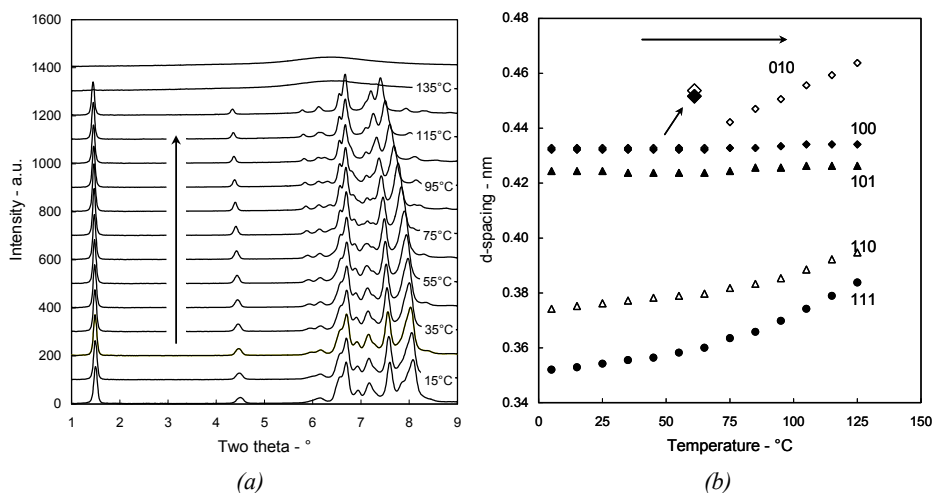


Figure 4.4: Structural changes of melt crystallized BDHA upon heating at 10°C/min by time-resolved WAXD ($\lambda = 0.0496$ nm). The azimuthally integrated diffraction patterns as function of temperature are plotted in Figure (a). Careful analysis of the Bragg reflections in combination with the TREOR90 powder diffraction indexing method assisted in assigning the crystallographic planes to the observed diffraction signals. Variations of the interchain/intrasheet and interchain/intersheet related spacings, given by closed and open symbols respectively, are followed as function of temperature on heating (b). It is to be noted that the 010 diffraction signal is superimposed by the 100 signal at temperatures below 75°C.

Although the structural behavior as a function of temperature suggests the viability of BDHA as a model system, the role of conformational changes and hydrogen bonding efficiencies is elaborated in a detailed solid state NMR spectroscopy study below.

Figure 4.5 presents the ^{13}C CP-MAS and ^1H MAS solid state spectra of melt crystallized BDHA on heating to 130°C (Figure 4.5a, b) and subsequent cooling (Figure 4.5c, d). The chemical shifts of characteristic signals are explicitly summarized in table 4.1. For the melt crystallized BDHA at 20°C , which was cooled below the exothermic transition at 22°C (Figure 4.3) during sample preparation, the ^{13}C carbonyl, α_{C} and α_{N} signals are in

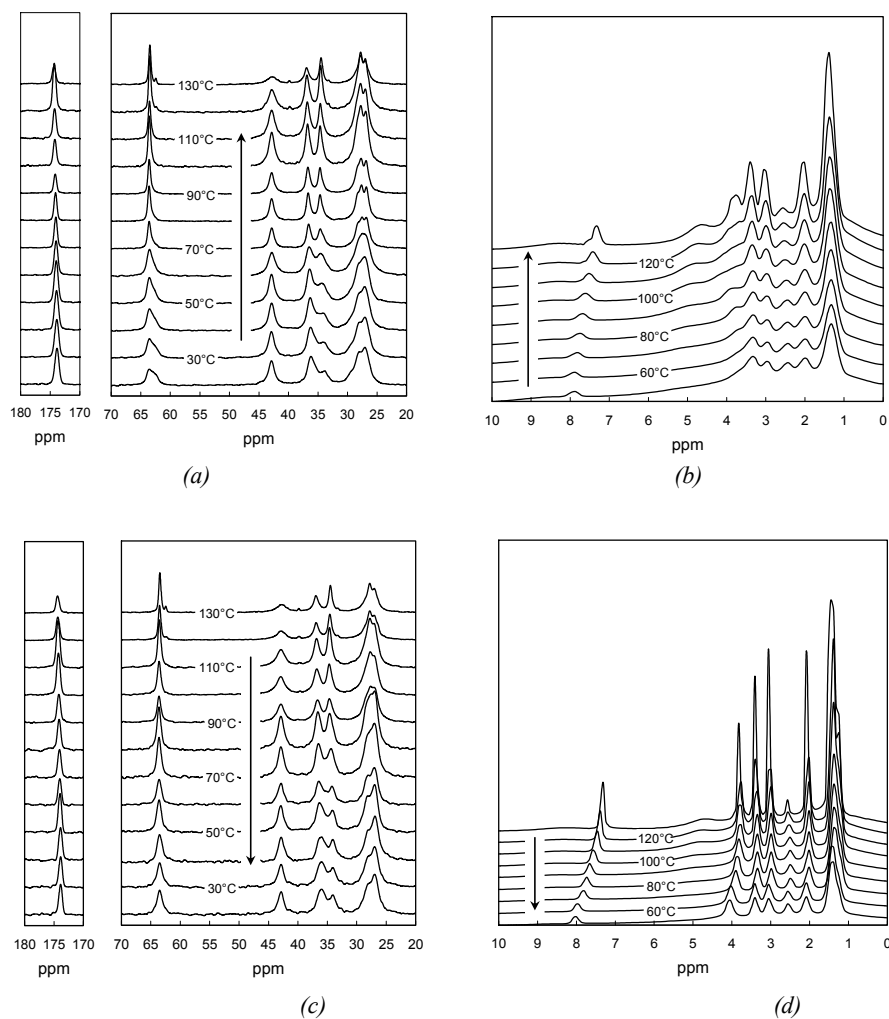


Figure 4.5: Solid state ^{13}C CP-MAS spectra, (a) and (c), and ^1H MAS spectra, (b) and (d), following the balance between thermal motion and hydrogen bonding efficiencies through the sequential heating, (a) and (b), and cooling profile, (c) and (d), below the melting temperature.

agreement with the reported chemical shifts for polyamide 66 in literature²¹. The ¹³C signal at 34.1 ppm at 20°C is assigned to gauche conformers¹⁰, which up to the endothermic transition at 79°C shifts to 34.5 ppm and gradually intensifies with increasing temperature. The changes in chemical shift and signal intensity indicate changes in the population and statistics of gauche conformers. Simultaneously the α_C ¹³C signal adopts a chemical shift of 36.5 ppm that according to Ando and Asakura arises from the gradual increase in molecular motion²¹. Moreover, within the respective temperature range, a gradual change in the chemical environment of the ω_C carbon nuclei is observed. While the chemical shift remains unchanged, the peak width at half height decreases from approximately 2 ppm at 20°C to 1 ppm at 60°C. Since narrowing of the CP-MAS signal reflects enhanced mobility, it is likely that the gradual increase in gauche conformers affects the hydrogen bonding efficiencies of the hydroxylic end groups.

Table 4.1: Chemical shifts of specific ¹³C CP-MAS and ¹H MAS signals in melt crystallized BDHA crystals through the exposed temperature profile ranging from 20 up to 130°C.

	CO ¹³ C	ω _C ¹³ C	α _N ¹³ C	α _C ¹³ C	¹³ C _{gauche}	N-H ¹ H	O-H ¹ H
	ppm	ppm	ppm	ppm	ppm	ppm	ppm
Melt crystallized ^{T1}							
120°C	174.3	63.5	42.8	36.9	34.5	7.45	3.75
80°C	174.1	63.6	42.9	36.7	34.6	7.73	3.75
60°C	174.0	63.5	42.8	36.5	34.5	7.87	3.82
20°C / 50°C ^{a)}	173.9	63.5	42.9	36.1	34.1	-	-
Melt crystallized ^{T1}							
120°C	174.3	63.5	42.9	36.9	34.6	7.38	3.75
80°C	174.1	63.6	42.9	36.6	34.6	7.73	3.82
60°C	174.0	63.6	42.9	36.5	34.2	7.94	3.96
20°C / 50°C ^{a)}	173.9	63.5	42.9	36.0	34.1	-	-

^{a)} Since the high spinning speed (30kHz) in the ¹H MAS experiments increases the sample temperature with approximately 30°C, the minimum temperature for the ¹H MAS signals is 50°C.

With the endothermic transition at 79°C the ¹³C CP-MAS signal of the methylene groups in gauche conformation intensifies significantly. At the same time the ω_C ¹³C signal increases in intensity too. The α_C ¹³C signal shifts from 36.5 ppm at 60°C to 36.7 ppm at 80°C. In the ¹H MAS spectra the amide and hydroxyl proton signals change from 7.87 and 3.82 ppm at 60°C to 7.73 and 3.75 ppm at 80°C respectively. A decrease in the chemical shifts of the nuclear spins accounts for an increased shielding of the nuclear spins by the surrounding electron clouds. Hence, the gradual induction of gauche conformers, expressed as a crankshaft type of motion, seems to initiate the out-of-plane wagging of the amide motifs. As a consequence the hydrogen bonding efficiencies in the amide and hydroxyl groups are reduced, resulting in the observed changes in the chemical shifts. On further heating the transfer of the rotational motion to the hydrogen bonded moieties becomes even

more pronounced. Prior to melting the ^{13}C carbonyl, the α_{C} ^{13}C and the NH ^1H signals change from 174.1, 36.7 and 7.73 ppm at 80°C to 174.3, 36.9 and 7.45 ppm at 130°C respectively. These findings suggest that the structural changes on heating indeed originate in a balance between emerging gauche conformers on heating and less effective electron exchange between electron donors and acceptors.

In analogy to the WAXD data the changes in solid state ^{13}C CP-MAS NMR experiments are reversible on cooling. Whereas a gradual decrease in gauche conformers is observed by a reduced peak intensity, a slight broadening of the ω_{C} ^{13}C signal was observed only at 20°C. Peak broadening arises from a decrease in molecular motion that enables more effective hydrogen bonding of the hydroxylic end groups. The formation of such hydrogen bonds poses restrictions on the entire molecular motion. Though the high spinning speeds in the ^1H MAS experiments did not allow measurements below 50°C¹⁹, explaining the well resolved ^1H MAS spectra and different chemical shifts on cooling, the effect of the increasing hydrogen bonding interactions on cooling is evident in the chemical shifts of the amide and hydroxylic proton signals. In contradiction to the out-of-plane wagging of the amide motifs on heating and the re-establishment of highly effective interchain/intrasheet hydrogen bonding on cooling in EDHA¹⁰, the continuous shift in the amide and hydroxylic proton signals suggests that interchain/intrasheet hydrogen bonding is not yet established on cooling BDHA to 50°C.

The NOESY spectrum, Figure 4.6, reveals a distinct correlation between the amide and hydroxylic protons, indicating that the two polar entities are aware of each others presence in space. Mixing times of 10 and 40 ms in the NOESY experiment do not realize

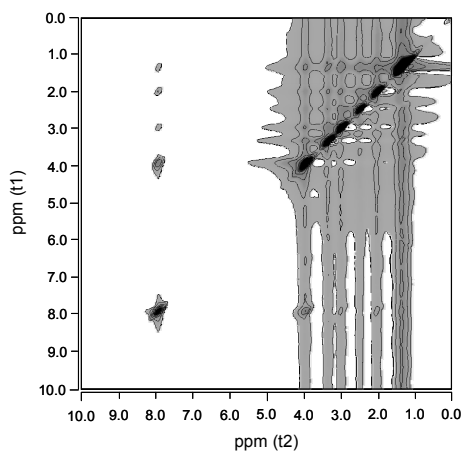


Figure 4.6: A 2-D ^1H NOESY spectrum of melt crystallized BDHA recorded at 30 kHz MAS at 50°C, probing the correlation of the amide and hydroxyl protons positioned at 7.94 and 3.96 ppm respectively.

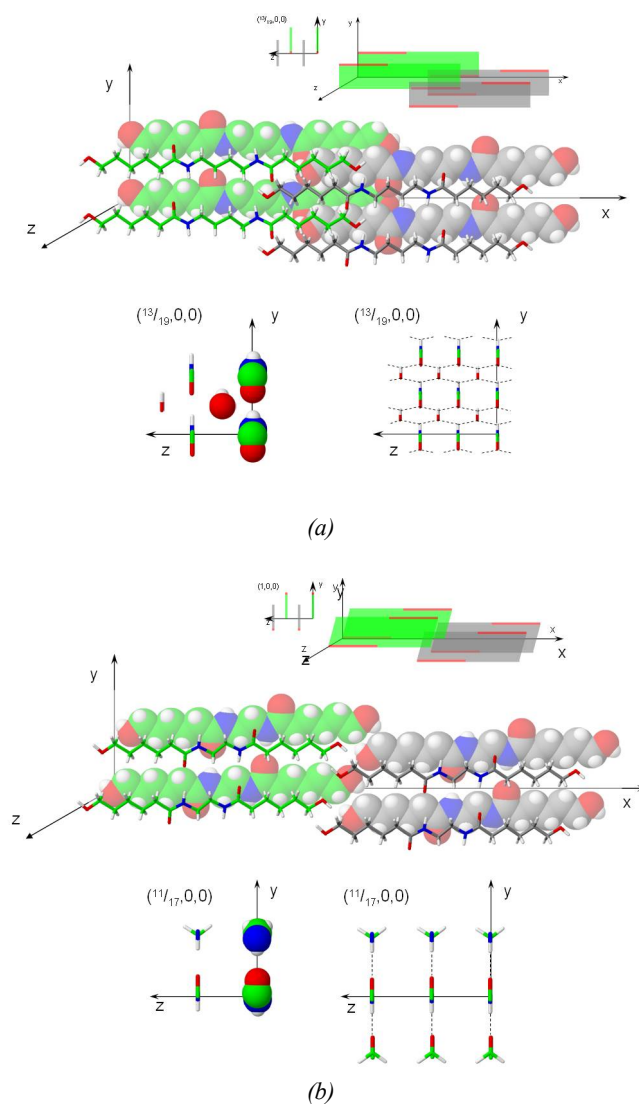


Figure 4.7: The structural organization of BDHA molecules at optimal hydrogen bonding efficiency, Figure 4.7a. Though polyamides and EDHA feature a single amide-amide hydrogen bonded plane as recapitulated in Figure 4.7b, in BDHA the amide-hydroxyl interaction in BDHA entails two hydrogen bonded planes localized between the amide planes. The maximum hydrogen bonding between BDHA molecules originates in interdigitation of the green and grey molecules (or planes). This geometrical scenario arises due to translation of a molecule by $(\frac{13}{19}|x|, \frac{1}{2}|y|, \frac{1}{2}|z|)$, i.e. $\frac{13}{19}$ of the molecular length along the x -axis (having 19 main chain covalent bonds, excluding the hydroxyl protons), $\frac{1}{2}$ the distance between molecules within a single amide plane in the y direction (denoted by the either green or grey planes in the top Figure), and $\frac{1}{2}$ the distance between the amide planes. The mirrors are located at $(0, n+\frac{1}{2}y, 0)$ with n as a multiple of $|I|$.

a correlation between the amide and hydroxyl moieties of the same molecule. The increase in the alkyl diamine segment, with respect to EDHA, apparently facilitates different hydrogen bonding geometries sheet structures. In stead of a unit cell that comprises two planes of in-planar hydrogen bonded molecules, as observed in EDHA, the BDHA unit cell features amide-hydroxyl hydrogen bonding between molecules of neighboring sheets (Figure 4.7). Thus, instead of hydrogen bonding along the y -direction only, like in EDHA, in BDHA the hydrogen bonding is located in the yz plane. Such a possibility arises due to the presence of hydroxylic end groups between the planes of the amide motifs, rendering maximum hydrogen bonding efficiency.

Despite the fact that the role of BDHA as a model molecule, which represents the crystalline domains in 4Y polyamides, is questionable, the thermodynamic transitions do originate from thermally triggered molecular motion and hydrogen bonding efficiencies. In the following section we will address the influence of superheated water on the crystallization of BDHA and the implications on hydrogen bonding in these specific geometries.

4.3.2 Crystallization from the superheated state of water; chain packing and hydrogen bonding efficiencies

Saturation of the amide moieties by water molecules, originating in continuous electron exchange processes as revealed in chapter 2 and 3, may mediate crystallization^{9,10}. The DSC thermogram of BDHA crystals grown from water, Figure 4.8, reveals the disappearance of the endothermic transition at 79°C and the appearance of a novel endothermic transition of 10.4 J/g at 120°C prior to melting at 138°C. It is to be noted that the melting temperature and enthalpy hardly differ from the melt crystallized BDHA samples. Exposing the water crystallized crystals to sequential temperature cycles below the melting temperature, viz. temperatures between -25 and 125°C, does not induce thermodynamic changes. These findings suggest that the endothermic transition at 120°C, which prevails during the temperature profiles, cannot be attributed to structural reorganization processes or the pre-melting of a less ordered crystal structure. The absence of crystals with a reduced melting temperature was besides confirmed by optical microscopy, where all crystals melt simultaneously upon heating.

In order to investigate the structural implications of water molecules, present during crystallization and possibly trapped within the crystal lattice, temperature dependent WAXD experiments were performed in the range of 5 to 125°C at a rate of 10°C/min, Figure 4.9. In comparison with the diffraction pattern of melt crystallized BDHA at 5°C, the diffraction pattern of the water crystallized sample is better resolved. Peak indexing, resulting in the peak assignment as partly presented in Figure 4.9c, shows that the 010 diffraction signal remains unchanged while the 100 signal slightly, though significantly

changes from 0.432 to 0.426nm. In combination with the enhanced resolution the decrease in the 100 diffraction signal suggests a better and denser molecular packing within the crystal lattice, that may to be attributed to the fact that the crystals have been grown from solution. Moreover, although some changes in the integrated diffraction patterns are observed on heating to the endothermic transition at 120°C, for example the 001 diffraction signal that increases from 1.86 nm at 5°C to 1.93 nm at 115°C, the interchain/intrasheet and interchain/intersheet diffraction signals remain fairly constant. Above the endothermic transition at 120°C the interchain/intersheet or van der Waals related 010 and 111 diffraction signals tend to increase. The expansion is likely to arise from reduced van der Waals attraction forces on heating in combination with enhanced molecular motion. These findings suggest that crystallization from the superheated state of water entails an improved molecular packing in the lattice, which induces spatial restrictions and enhanced hydrogen bonding efficiencies since less intermolecular distances promote electron exchange efficiencies in the hydrogen bonded moieties. The 001 diffraction signal however increases from 1.93 nm to 1.97 nm. These observations indicate that the *c*-axis of the unit cell does not correspond with the molecular axis. Whereas the contour length of the molecules generally decreases with the induction of gauche conformers, the 001 signal and hence the *c*-axis increases on heating. The balance between thermally triggered gauche conformers and hydrogen bonding efficiencies induces changes in the position of the molecules in the crystal unit cell, viz. changes in the lattice parameters.

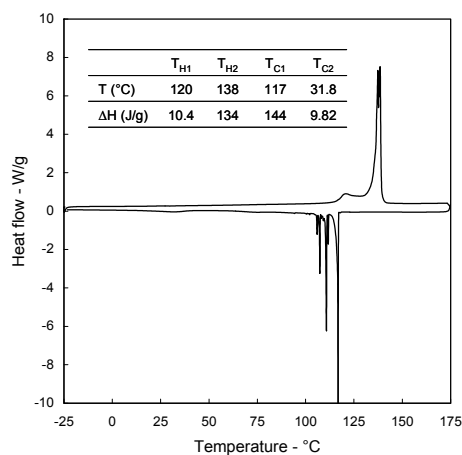


Figure 4.8: DSC thermogram of BDHA crystals grown from the superheated state of water. The transition temperatures and corresponding enthalpies upon heating (T_{H1} and T_{H2}) and cooling (T_{C1} and T_{C2}) are listed in the embedded table.

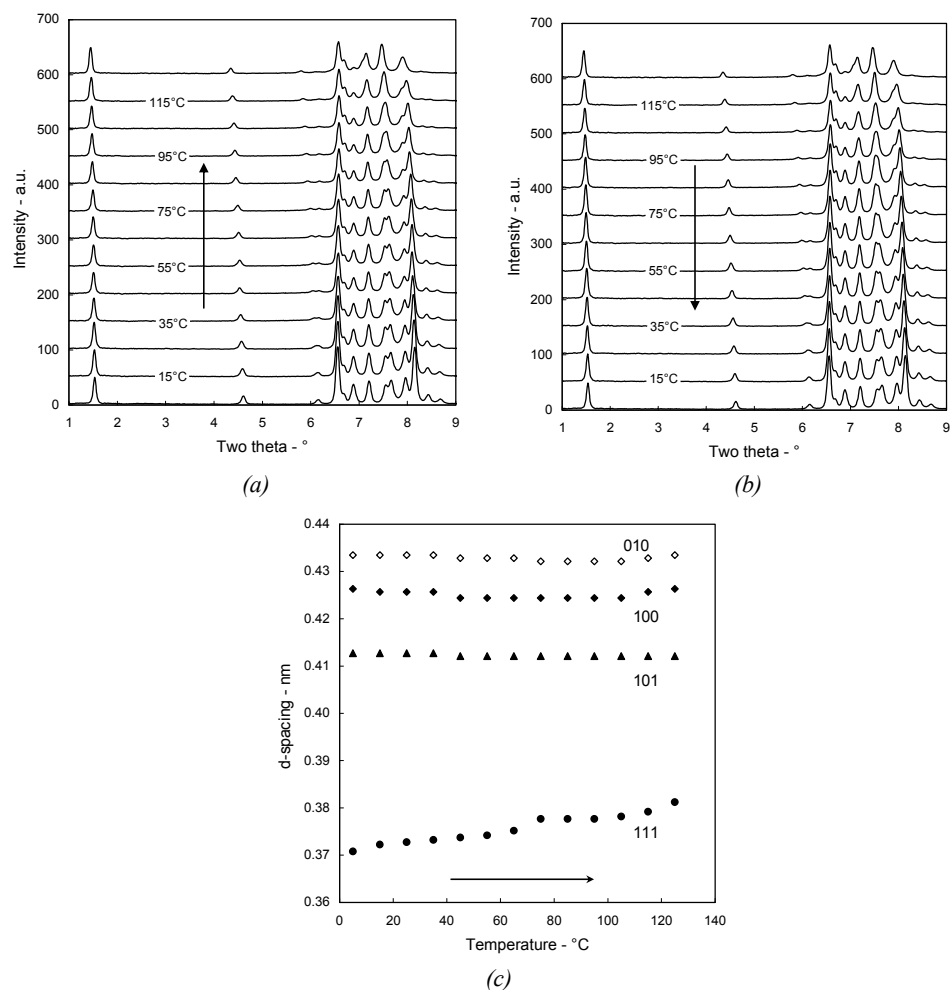


Figure 4.9: Azimuthally integrated diffraction patterns of water crystallized BDHA upon heating (a) and cooling (b) at 10°C/min by time-resolved WAXD ($\lambda = 0.0496$ nm). Analysis of the Bragg reflections in combination with the TREOR90 powder diffraction indexing method resulted in assigning the crystallographic planes to the observed diffraction signals. The interchain/intrasheet and interchain/ intersheet spacings, given by closed and open symbols respectively, are followed on heating (c).

FTIR spectroscopy, whether or not in polarized mode, has proven to be a successful method in the localization of possibly hosted water molecules in the lattice, chapter 3¹⁰. In Figure 4.10 the spectra of melt and water (superheated water) crystallized BDHA are compared. Before discussing the conformational differences it has to be noted that the absence of specific carboxylic acid carbonyl stretch vibrations, in the range of 1760 to

1735 cm^{-1} for hydrogen bonded and from 1730 to 1705 cm^{-1} for non-hydrogen bonded species²², indicates that hydrolyses does not occur within the experimental time scale of dissolution.

Crystallization from the superheated state of deuterium oxide, which induces proton deuterium exchange reactions, enables the discrimination of the NH and OH stretch bands in the high frequency region (3600 to 3200 cm^{-1}). In analogy to EDHA the strong band at approximately 3300 cm^{-1} represents a combination band of two vibrational modes, the relatively efficient hydrogen bonded NH and OH stretch vibrations. Upon crystallization from D_2O two of the four polar stretch bands prevail in the high frequency region. Since the C-OH stretch vibration in the region of 1060 to 1050 cm^{-1} appears in the three spectra, regardless the wavenumber, it is likely that H-D exchange of the hydroxylic end groups does not occur. In fact, the comparison of the H_2O and D_2O crystallized samples shows that the amide II band, which is a combination band comprising the C-N stretch and C-N-H bending in-plane vibrations, partially disappears. On the expense of the amide II band at 1541 cm^{-1} a new band arises at 1450 cm^{-1} , a change that according to Grdadolnik et al. is attributed to the deuterium exchange of the amide proton resulting in a C-N-D bending in-plane vibration^{10,23,24}. These findings indicate that two prevailing bands in the high frequency region at 3407 and 3314 cm^{-1} of the D_2O crystallized sample originate in OH stretch vibrations. The same spectrum shows a set of vibrations in the region of 2550 to 2400 cm^{-1} that correspond to two types of hydrogen bonded N-D stretch vibrations^{23,24}.

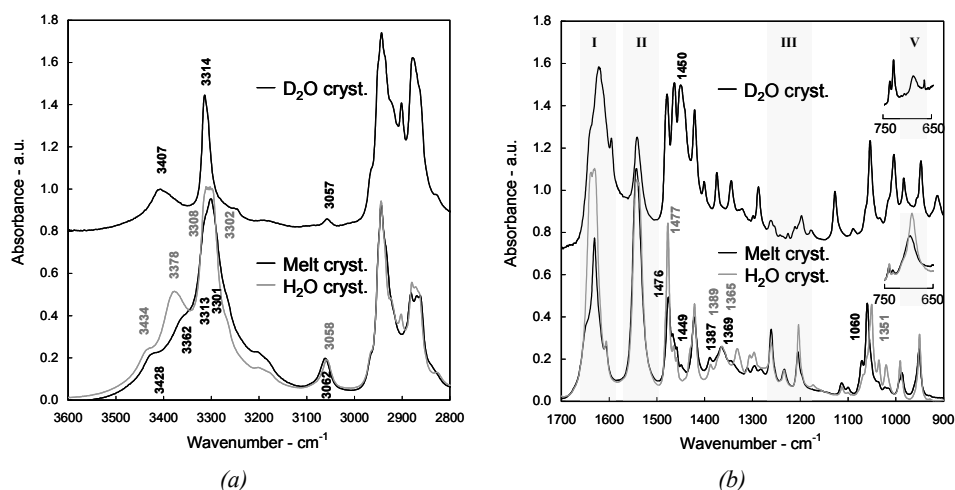


Figure 4.10: FTIR spectra presenting the conformational differences between melt crystallized BDHA (black bottom spectrum) and BDHA crystallized from the superheated state of water (grey bottom spectrum). The upper spectrum crystallized represents BDHA crystals grown from the superheated state of D_2O , in which amide proton deuterium exchange processes assist the vibrational band assignments²²⁻²⁴. Scaling the spectra with respect to the antisymmetric CH_2 stretching vibration at 2944 cm^{-1} validates the comparison in relative absorbance.

Although the OH and NH stretch bands, appearing both as hydrogen bonded and non-hydrogen bonded entities, are identified successfully, saturation of efficiently hydrogen bonded NH, OH and CO stretching in the single crystal spectra limit adequate peak positioning. Differences in the less efficiently hydrogen bonded OH and NH stretch are observed, from 3428 to 3434 cm^{-1} and from 3362 to 3378 cm^{-1} respectively, that most likely originate either in the interaction of amide motifs with water molecules or in the polar moieties located at the crystal surface (Figure 4.7). As such these bands do not validate changes in hydrogen bonding of the bulk. However, the amide II overtone, the amide V (NH out-of-plane scissoring) and C-OH stretch bands, which shift from 3062 to 3058 cm^{-1} , from 698 to 693 cm^{-1} and from 1060 to 1051 cm^{-1} respectively upon crystallization from the superheated state of water, are assigned to assess changes in hydrogen bonding efficiencies. The decrease in these specific wavenumbers arises from improved hydrogen bonding efficiencies. The spatial restrictions as observed by WAXD, which promote the hydrogen bonding efficiency, are depicted by the apparent absorption increase of the amide V band, Figure 4.10b. The denser and well ordered packing of the water crystallized sample results in the disappearance of the disordered gauche CH_2 scissoring at 1449 cm^{-1} ¹⁰ and imposes a confined environment on the α_{N} amide-methylene linkages, witnessed by the intensified α_{N} CH_2 scissoring at 1477 cm^{-1} . The confinement in combination with enhanced hydrogen bonding efficiencies hampers the out-of-plane scissoring of the NH group.

In EDHA crystals grown from the superheated state of water, chapter 3, the weakly hydrogen bonded OH and NH stretch band, positioned at 3401 and 3332 cm^{-1} respectively, in combination with specific (anti)symmetric COO^- vibrations at 1610 and 1442 cm^{-1} , indicating the presence of water molecules in the vicinity of the amide motifs¹⁰, vanish throughout a temperature profile that ranges between 5 and 125°C. Besides, polarized FTIR spectroscopy showed that the less efficiently bound NH stretch band was positioned in the opposite orientation direction of the carbonyl stretch (amide I) vibrations, probing the shielding of the amide-amide hydrogen bonding by water molecules. The migration of the water molecules in the single EDHA crystals induced the re-establishment of amide-amide hydrogen bonding, rendering a solid state crystal transformation. Subtracted polarized FTIR spectra on single BDHA crystals, where the polarized light was either directed perpendicular or parallel to the orientation of the molecules, are presented as function of temperature in Figure 4.11. Upon heating the less efficiently hydrogen bonded NH stretch vibration, which is located in a deviating polarization direction compared to the carbonyl stretch band, broadens significantly on heating. As well at 95 as at 125°C the mobility of the weakly bound NH moiety, depicted by the broadening, increases. The width at half height of the (anti)symmetric CH_2 stretch vibrations increases simultaneously and accounts for enhanced molecular motion and the induction of gauche conformers. The disruption of the rigid trans conformations in the aliphatic moieties erases the confined α_{N} CH_2

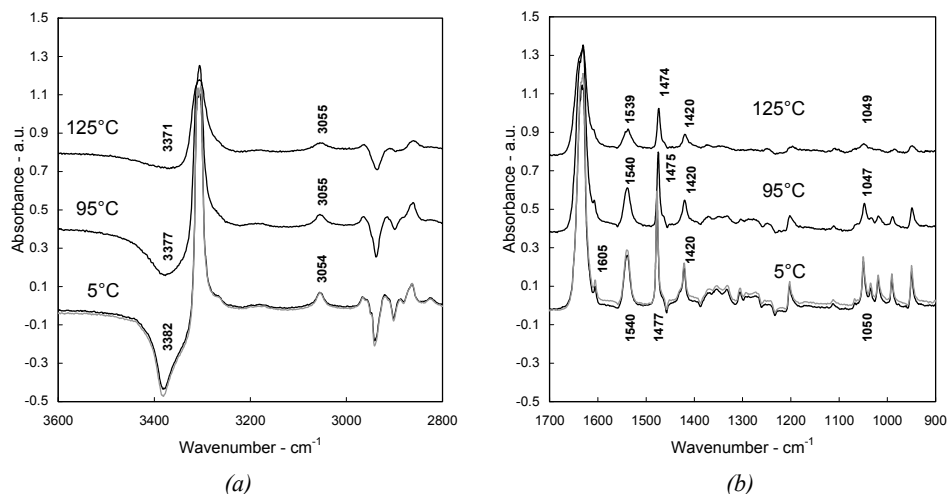


Figure 4.11: Subtracted polarized FTIR spectra ($90\text{-}0^\circ$) of a single BDHA crystal on heating to 125°C (black spectra) and after cooling to 5°C (grey spectrum). The polarization direction was either parallel (0°) or perpendicular (90°) to the molecular axis.

scissoring that is imposed by the organizational discrepancy of the planar amide and tetrahedral hydroxyl hydrogen bonded geometries¹⁰. However, the hydrogen bonding efficiencies, primarily assessed by the well resolved polarized amide II band at approximately 1540 cm^{-1} , seem to decrease only from the endothermic transition onwards. The highly efficient hydrogen bonding in water crystallized BDHA apparently withstands the influence of gauche conformers, which are actually present at low temperatures up to a temperature of 120°C that matches with the endothermic transition observed in the DSC thermogram of figure 4.8. The spectral comparison of the water crystallized sample before (in black) and after heating (in grey) at 5°C shows that the weakly bound NH stretch and the antisymmetric carboxylate vibration at 1605 cm^{-1} prevail throughout the temperature cycle. Would this mean that physically bound water molecules, if present in or at the surface of the lattice, form thermodynamically stable structures in these specific geometries? The answer will be revealed in the detailed solid state NMR spectroscopy studies that follow.

A comparison of the ^{13}C CP-MAS spectra at 20°C , Figure 4.12a, reveals that with the exception of the ^{13}C chemical shift of the carbonyl, which hardly alters in terms of the chemical shift and relative intensity, the overall spectrum of the water crystallized sample is better resolved. Considering the fact that the ^{13}C chemical shift is sensitive to changes in the chemical environment and the spatial restrictions, narrowing of the peaks is likely to arise from an improved chemical shift distribution of spin that may result from a highly

ordered molecular packing²⁵⁻²⁷. Although the chemical shift of the ω_C ^{13}C peak of the melt crystallized sample, induced by the coexistence of two types of hydroxylic end groups that reside in different chemical environments. On crystallization from the superheated state of water the less efficiently hydrogen bonded entity at lower chemical shift tends to disappear. In general, if the hydroxylic oxygen electrons are involved in electron exchange processes, either with other hydroxyl groups, amide moieties or water molecules, the electron donating oxygen pulls more electrons from its covalently bonded ω_C carbon atom that hence becomes less shielded (ppm \uparrow). Since the population of ω_C carbons next to less hydrogen bonded hydroxylic end groups diminishes, the chemical shift distribution narrows and the ω_C ^{13}C CP-MAS signal intensifies. These findings support the earlier statement that the high resolution of the ^{13}C CP-MAS spectrum of the water crystallized sample does not result from enhanced molecular motion, which significantly reduces as the hydrogen bonding efficiency of the hydroxyl moieties raises.

In analogy to the ω_C ^{13}C CP-MAS chemical shift the α_N and α_C methylene units, which are located on either side of the amide motifs, are likely to be affected by the increase in hydrogen bonding efficiency as well. The water crystallized ^{13}C CP-MAS spectrum reveals a better defined chemical environment of the α_N CH_2 group that besides slightly shifts from 42.9 to 43.0 ppm. A slight, though subtle change that indicates that the hydrogen bonding in which the amide groups are involved also slightly increases in efficiency. Ando and Asakura besides assigned an increase in the ^{13}C CP-MAS α_N CH_2 signal to crystal perfection²¹. While the chemical shift of the α_N methylene unit increases

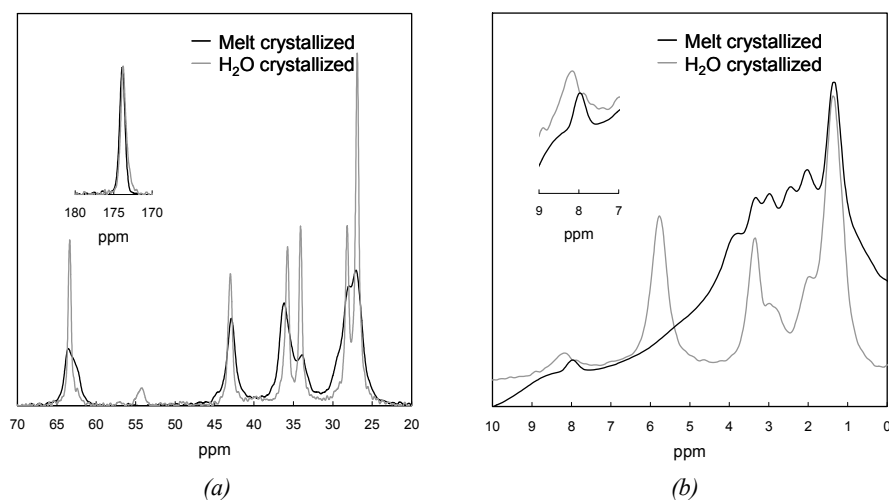


Figure 4.12: Solid state ^{13}C and ^1H NMR spectroscopy, figure (a) and (b) respectively, probing conformational changes and differences in hydrogen bonding upon crystallization from the superheated state of water. The melt crystallized spectra serve as a reference and are plotted in black, while the water crystallized spectra are presented in grey.

upon crystallization from superheated water the α_C ^{13}C chemical shift decreases from 36.1 to 35.8 ppm. Lowering of this specific aliphatic ^{13}C CP-MAS signal is also encountered in hydrogen bonded amide based crystals that are exposed to a decrease in temperature, as for example extensively discussed in chapter 3 of this dissertation¹⁰. In that scenario, due to low temperatures, and thus low molecular motion, the hydrogen bonding efficiencies increase. These changes go along with a reduced chemical shift of the ^{13}C CP-MAS α_C CH_2 signal^{10,21}.

So far the interpretation of the ^{13}C CP-MAS differences clearly demonstrated increased hydrogen bonding and crystal perfection. Two parameters that hinder or suppress molecular motion. However, upon crystallization from the superheated state of water the ^{13}C CP-MAS signal of methylene segments in gauche conformation (34.1 ppm) intensifies significantly. The drastic increase in this signal, especially with respect to the observed changes in the other aliphatic ^{13}C CP-MAS responses, suggests a higher quantity of gauche conformers. Since crystal perfection and efficient hydrogen bonds prohibit high molecular motion, the gauche conformers arise from conformational restrictions or confinement in the aliphatic sequences. A conformational disparity between efficiently hydrogen bonded planar amide motifs and tetrahedrally organized hydroxyl groups, as observed in EDHA and postulated in the preceding FTIR paragraphs as well, prevents all-trans conformations in the methylene segments of the molecules. Crystallization from the superheated water results apparently in ideal amide and hydroxyl hydrogen bonding on the expense of all-trans conformations in the aliphatic regions.

In comparison with the melt crystallized spectra, the ^1H MAS spectra of the water crystallized samples are much better resolved as depicted in Figure 4.12b. Broad peaks in ^1H NMR generally account for ^1H - ^1H dipolar coupling, which can be disrupted by high molecular motion and mechanical rotation of the sample such as magic angle spinning²⁸. A large peak width may also arise from a broad chemical shift distribution of spin, which is a more liable explanation considering the discussion on the ^{13}C CP-MAS spectra above. The conformational distortion of the aliphatic regions reflects in the aliphatic ^1H MAS signals that are positioned between 3.5 and 1.0 ppm. Though the chemical shift of the ω_C proton at 3.34 ppm does not change upon the crystallization from the superheated state of water, both the chemical environment of the hydroxyl and amide protons changes dramatically. The amide ^1H MAS signal shifts from 7.87 to 8.17 ppm, whereas the hydroxyl proton is characterized by an increase in the chemical shift from 3.82 to 5.78 ppm. It is to be noted that an accurate comparison of the relative intensity of the respective ^1H MAS signals is hindered by the unresolved ^1H MAS spectrum of melt crystallized BDHA and is as a consequence excluded from the present discussion. Since the amide and hydroxyl moieties act as proton donor, and hence as electron acceptor in hydrogen bonding electron exchange processes, one would expect an accumulation of electrons around the nuclei of the respective protons at first sight. Nevertheless, sharing of electrons between hydrogen bonded motifs entails a travel of the protons along the electron exchange path. In other

words, if the hydrogen bonding efficiency in the OH or NH moieties is low, the electron deficient proton sits in the close proximity of the electron rich oxygen or nitrogen to fulfill its continuous quest for electrons and the chemical shift will be comparably low. If the local density of highly electronegative atoms, such as oxygen or nitrogen, increases, electron exchange processes, viz. hydrogen bonding, establishes²⁸. As a consequence the proton, though satisfying the need for free electrons, will be pulled from its covalently bonded atom, increasing the bond length or inter-atomistic distance. On average this results in less shielding of the proton nuclei by surrounding electrons and the chemical shift increases. The two-dimensional ¹H NOESY spectrum, presented in Figure 4.13, shows an apparent correlation between the amide proton and the hydroxyl proton at 8.17 and 5.78 ppm respectively. This cross correlation indicates that the molecular organization, featuring amide-hydroxyl hydrogen bonding and accounting for the prevailing carboxylate vibrations (1605cm⁻¹), of BDHA molecules on crystallization from the superheated state of water remains unchanged.

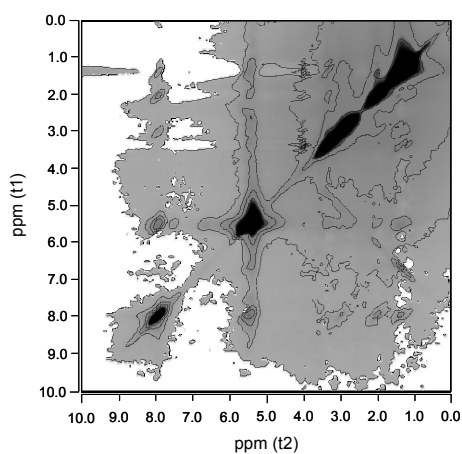


Figure 4.13: A 2-D ¹H NOESY spectrum of BDHA crystals obtained from the superheated state of water recorded at 30 kHz MAS at 50°C, probing the correlation of the amide and hydroxyl protons positioned at 8.17 and 5.78 ppm respectively.

Spectroscopic analyses of water crystallized N,N'-1,4-butanediyl-bis(6-hydroxyhexanamide) does not reveal any evidence for the accommodation of physically bound water molecules in the crystal or at the crystal surface. Yet it is demonstrated that crystallization from the superheated water entails crystal perfection and mediates the hydrogen bonding, yielding thermodynamically more stable crystalline structures. Nonetheless, though amide-hydroxyl hydrogen bonded structures do not favor stable water-amide or water-hydroxyl interactions by the absence of vacant positions, a single batch of

water crystallized BHDA crystals was encountered where water molecules in fact were incorporated in the vicinity of the polar moieties. In the following section I take the opportunity to reveal the implications on hydrogen bonding in these specific geometries using temperature dependent solid state ^1H MAS and ^{13}C CP-MAS NMR spectroscopy.

4.3.3 Influence of enclosed H_2O molecules on hydrogen efficiencies

Figure 4.14 presents ^{13}C CP-MAS and ^1H MAS NMR spectra of BDHA crystals grown from the superheated state of water under identical crystallization conditions. Along the coming discussion the black spectrum appears to hold water molecules in the vicinity of the polar moieties. The first striking effect is that the chemical shifts of the ^{13}C CP-MAS signals do not change at all. The relative peak intensities changes of the black ^{13}C CP-MAS spectrum decrease significantly. Though the peak positions do not alter significantly, shoulders at lower chemical shift are observed for the ω_{C} and α_{N} ^{13}C CH_2 signals at 63.4 and 43.0 ppm respectively. As elaborately discussed in previous paragraphs, these shoulders represent methylene groups that are located next to the less efficiently hydrogen bonded or even amorphous amide and hydroxyl motifs²¹. Due to the presence of less efficiently hydrogen bonded moieties more molecular motion may be anticipated. However, a higher mobility of the molecule or segments of the molecule would lead to sufficient decoupling power and thus intensified ^{13}C CP-MAS signals. In combination with the less hydrogen bonded entities the diminished peak intensities and increased peak widths of the black spectrum are attributed to broader chemical shift distributions of the ^{13}C spins.

In agreement with the ω_{C} and α_{N} methylene segments, the black ^1H MAS spectrum (Figure 4.14b) reveals distinct differences in the hydrogen bonding efficiencies as well. Focusing on the hydrogen bonding moieties, an asymmetric amide ^1H MAS signal, representing two different chemical environments, is observed in the black spectrum and becomes more prominent on heating, Figure 4.15. The NH proton, of which the nucleus is less shielded by electrons and hence strongly hydrogen bonded, is positioned at 7.94 ppm, while the less effectively hydrogen bonded amide proton is observed at 7.87 ppm (Table .2). The broadness of ^1H MAS signal at 7.94 ppm marks the rigidity of the amide proton that is imposed by the highly efficient hydrogen bonding. In comparison with the previously described water crystallized ^1H MAS spectrum (grey), where the hydroxyl proton is located at 5.78 ppm, a novel hydroxyl proton signal evolves (5.01 ppm) at the expense of the most efficiently hydrogen bonded hydroxyl that is located at 5.85 ppm. The fact that two hydroxylic proton signals are depicted suggests variations in the hydrogen bonding efficiencies of the hydroxyl moieties as well. The distinct decrease in the hydroxylic hydrogen bonding efficiency possibly arises from entrapped water molecules shielding the hydrogen bonding motifs. Electron exchange processes are dynamic in nature

and as water molecules introduce extra electrons in the vicinity of the polar moieties, such as the hydroxyl group, the net shielding of hydroxyl nuclei increases.

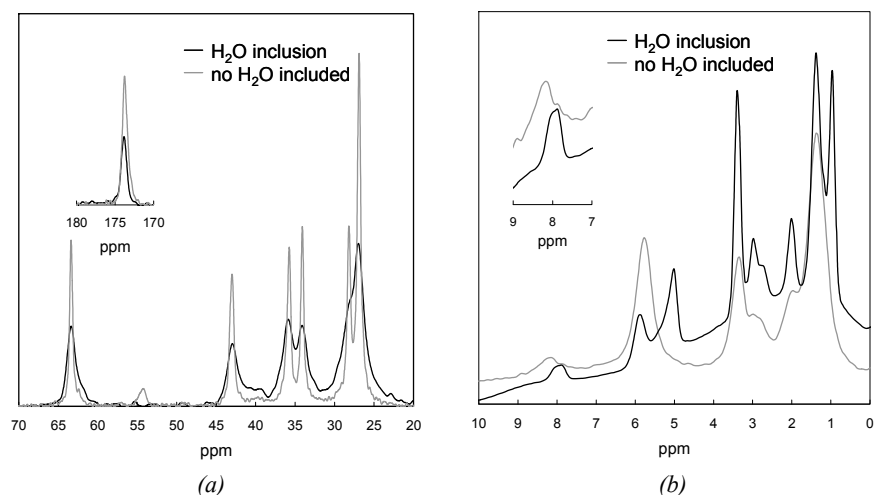


Figure 4.14: Solid state ^{13}C and ^1H NMR spectroscopy, figure (a) and (b) respectively, probing conformational changes and differences in hydrogen bonding on accommodating water molecules in close vicinity of the polar moieties. Grey spectra represent BDHA crystals grown from the superheated state of water. The black spectra arise from BDHA crystals that host water molecules after crystallization from the superheated state of water.

The ^1H MAS and ^{13}C CP-MAS signals of the black spectra show typical temperature dependent behavior for hydrogen bonded amide based crystals (Figure 4.15). To summarize, as a function of temperature the population of gauche conformers either increases or decreases. Gauche conformers, which are clearly present though the population seems to be smaller if water molecules are around (34.1 ppm at 20°C), induce a crankshaft type of motion along the molecular axis on heating that accounts for sharpening of the signals and intensified peaks. The crankshaft type of motion in the aliphatic domains is transferred progressively to the amide motifs that as a consequence start wagging out of their plane, resulting in decreased hydrogen bonding efficiencies. As discussed previously the decrease in the hydrogen bonding efficiencies in the amide motifs explains the decrease in the chemical shift of the amide ^1H MAS signal and the increase in the chemical shift of the ^{13}C CP-MAS carbonyl signal on heating (Figure 4.15a, b). On cooling, presented in figure 4.15c and d, the opposite trends are observed. Following the amide ^1H MAS signals, positioned at 7.94 and 7.87 ppm at 50°C, through the exposed temperature cycle that ranges between 50 and 130°C, the two signals tend to merge into a single, relatively efficiently hydrogen bonded amide proton at 8.00 ppm at 50°C upon cooling (Figure 4.15d,

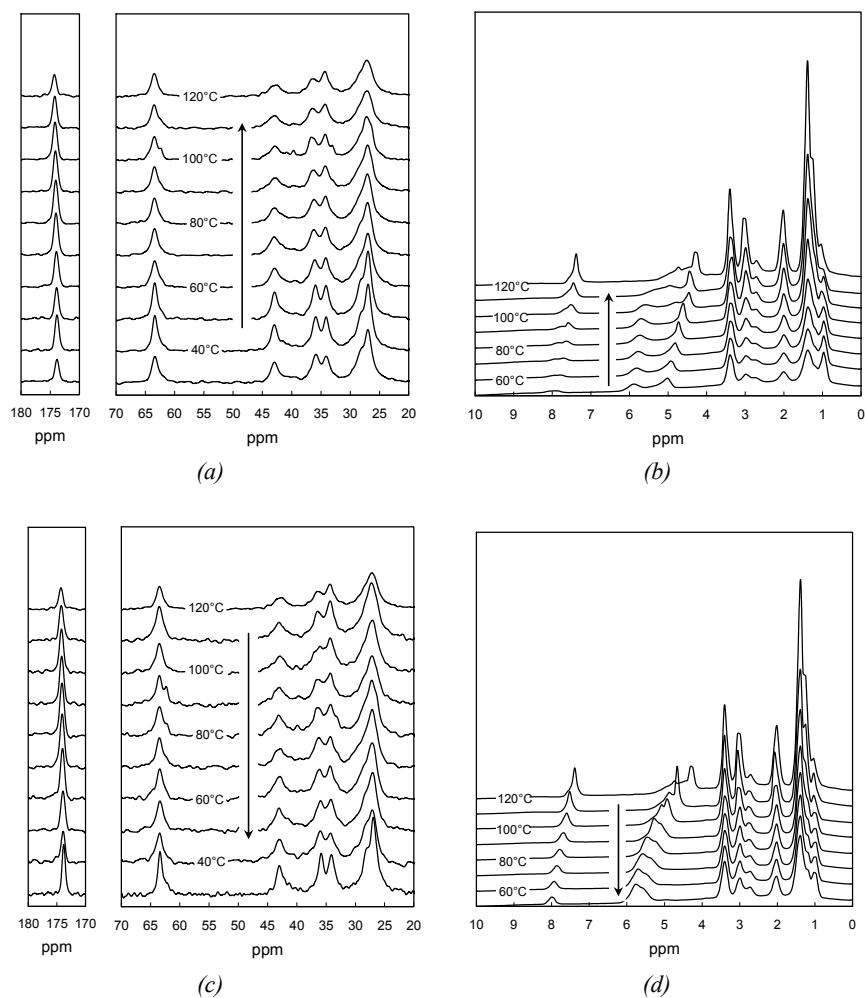


Figure 4.15: Solid state ^{13}C CP-MAS spectra, (a) and (c), and ^1H MAS spectra, (b) and (d), following the balance between thermal motion and hydrogen bonding efficiencies through the sequential heating, (a) and (b), and cooling profile, (c) and (d), below the melting temperature.

Table 4.2). In agreement the shoulder of the ^{13}C CP-MAS carbonyl signal at higher chemical shift, representing less effectively hydrogen bonded carbonyl entities, merges with the superimposed signal as revealed in Figure 4.15c. The increase in the peak intensity is hence attributed to a narrow chemical shift distribution of the carbonyl ^{13}C CP-MAS and the amide proton ^1H MAS signals. Vanishing of the non-hydrogen bonded α_{N} ^{13}C CP-MAS signal at approximately 40 ppm supports the increased hydrogen bonding efficiencies in the

amide moieties²¹. Disappearance of the less effectively hydrogen bonded entities is also observed for the hydroxylic ¹H MAS signal, initially positioned at 5.01 ppm as witnessed in the ¹H MAS spectra, though an asymmetric hydroxylic ¹H MAS signals prevails (Figure 4.16). Note that the decrease in the chemical shift of the hydroxylic protons upon heating arises from decreased hydrogen bonding efficiencies and improved electron shielding of the hydroxyl proton nuclei as the temperature rises. Moreover, with the temperature cycle below the melting temperature the chemical shift distribution of the aliphatic ¹H MAS signals narrows. However, care should be taken to assess differences in molecular motion before and after heating, especially in the ¹H MAS spectra, by means of relative peak intensities. Upon cooling, the temperature of the sample may not have passed the transition temperature of 31.8°C that is associated to the sufficiently low molecular motion to establish highly effective hydrogen bonding (Figure 4.8). These findings suggest that the water molecules, either residing at the crystal surface or within the crystal lattice, migrate from the polar moieties, resulting in the reestablishment of amide-hydroxyl hydrogen bonding. Taking the overall of effect of the water molecules on especially the ¹³C CP-MAS spectra into account suggests that water molecules do not solely associate and interact intimately with the polar motifs at the crystal surface but also within the crystal lattice. The presence of water molecules in the vicinity of amide motifs during crystallization of EDHA was found to erase the resonance and rigid character of the amide motifs¹⁰. Though amide-hydroxyl hydrogen bonding does not provide free or open hydrogen bonding vacancies to host water molecules, the “saturation” of polar moieties introduces an extra degree of freedom in the crystallization process, increasing the hydrogen bonding efficiencies.

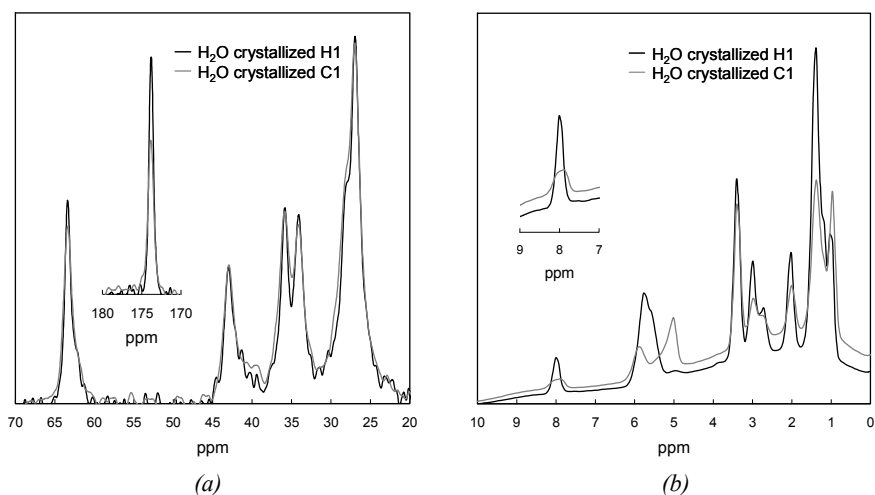


Figure 4.16: Solid state ¹³C and ¹H NMR spectroscopy, figure (a) and (b) respectively, probing conformational changes and differences in hydrogen bonding before (H1) and after the migration of water molecules from the polar moieties(C1) by a temperature cycle below up to 120°C.

Table 4.2: Chemical shifts of specific ^{13}C CP-MAS and ^1H MAS signals of BDHA crystals grown from the superheated state of water. The influence of water molecules on hydrogen bonding and conformational changes through the exposed temperature profile that ranges from 20 up to 130°C.

	CO ^{13}C	ω_{C} ^{13}C	α_{N} ^{13}C	α_{C} ^{13}C	$^{13}\text{C}_{\text{gauch}}$ e	N-H ^1H	O-H ^1H
	ppm	ppm	ppm	ppm	ppm	ppm	ppm
H ₂ O crystallized ^{T†}							
120°C	174.3	63.5	42.6	36.4	34.3	7.52 7.38	4.73 4.31
80°C	174.0	63.6	42.9	36.2	34.2	7.87 7.66	5.71 4.73
60°C	173.9	63.4	42.9	36.1	34.2	7.94 7.80	5.85 4.94
20°C / 50°C ^{a)}	173.8	63.4	43.0	35.9	34.1	7.94 7.87	5.85 5.01
H ₂ O crystallized ^{T‡}							
120°C	174.3	63.5	42.6	36.4	34.3	7.52 7.38	4.73 4.31
80°C	174.1	63.5	43.1	36.5	34.2	7.80	5.43
60°C	174.0	63.4	42.9	36.2	34.3	7.94	5.71
20°C / 50°C ^{a)}	173.8	63.4	43.0	35.8	34.1	8.00	5.78

^{a)} Since the high spinning speed (30kHz) in the ^1H MAS experiments increases the sample temperature with approximately 30°C, the minimum temperature for the ^1H MAS signals is 50°C.

4.4 Conclusions

Although N,N'-1,4-butanediyl-bis(6-hydroxy-hexanamide) was primarily selected as a model to investigate the influence of physically bound water molecules on hydrogen bonding in polyamide 4Y polymers, the molecular packing is characterized a second hydrogen bonded plane. Instead of amide-amide hydrogen bonding the symmetry in the aliphatic segments entails highly efficient amide-hydroxyl hydrogen bonding, filling all hydrogen bonding vacancies optimally. Nonetheless, the revealed hydrogen bonding geometry offers a unique opportunity to study the role of potentially enclosed water molecules on the electron exchange processes in hydroxyl-amide hydrogen bonded crystals. As function of temperature the population of gauche conformers either increases or decreases. Once the population of gauche conformers is sufficiently high the rotational motion is transferred to the amide moieties that start wagging out of their plane, witnessed by an endothermic transition at 78.6°C. Up to 78.6°C only minor changes have been observed in as well the hydrogen bonding efficiencies as the crystalline structure. Above 78.6°C the rotational motion is transferred progressively to the polar hydrogen bonded moieties, weakening the hydrogen bonding. Due to increased molecular motion, the “interchain/intersheet” distance increases significantly, while the “interchain/intrasheet” distance hardly changes. Upon cooling the opposite effects are observed, where the reduced molecular motion allows the establishment of efficient amide-hydroxyl hydrogen bonding, inducing an exothermic transition at 23.5°C.

Wide angle X-ray scattering strengthened with indexing of the diffraction signals reveals that crystallization from the superheated state of water entails a denser molecular packing with enhanced hydrogen bonding efficiencies, though the molecular organization within the unit cell remains unaffected. Effective hydrogen bonding in as well the amide as hydroxyl moieties, which are positioned in different orbital directions, requires non-trans conformations in the aliphatic segments of BDHA molecules. The crystal perfection does not only promote the hydrogen bonding efficiency, by decreasing the inter-atomic distances, but also imposes a spatial confinement. Upon heating, these constraints hinder molecular motion and more thermal energy, expressed as aliphatic gauche conformers, is required to transfer the rotational motion to the amide moieties effectively. The endothermic transition on heating, marked by the out-of-plane wagging of the amide motifs and reduced hydrogen bonding efficiencies, shifts from 78.6 to 120°C. Although amide-hydroxyl hydrogen bonded structures do not favor stable water-amide or water-hydroxyl interactions to host water molecules firmly, the increased hydrogen bonding efficiency, which is conformationally not preferred, suggests an active role of water during crystallization. In fact, in our solid state NMR studies crystals we did encounter physically interactive water molecules within the crystal lattice, albeit being unstable in nature. The intimate electron exchange processes with the polar motifs induces saturation of the amide motifs. The saturation disrupts the conformational confinement normally imposed by the planar resonance character during crystallization. Increasing the temperature to 120°C induces the migration of water molecules from the polar moieties and effective amide-hydroxyl hydrogen bonding establishes.

4.5 References

1. Jeffrey, G.A.; Saenger, W. *In Hydrogen Bonding in Biological Structures*, Springer-Verlag Berlin Heidelberg, **1994**.
2. Levy, Y.; Onuchic, J.N. *Annu. Rev. Biophys. Biomol. Struct.* **2006**, 35, 389-415.
3. Rastogi, S.; Terry, A.E.; Vinken, E. *Macromolecules* **2004**, 37, 8825-8828.
4. Vinken, E.; Terry, A.E.; Van Asselen, O.; Spoelstra A.B.; Graf, R.; Rastogi, S. *Langmuir* **2008**, 24, 6313-6326.
5. Yoshioka, Y.; Tashiro, K.; Ramesh, C. *Polymer* **2003**, 44, 6407-6417.
6. Yoshioka, Y.; Tashiro, K. *J. Phys. Chem. B.* **2003**, 107, 11835-11842.
7. Vinken, E.; Terry, A.E.; Hoffmann, S.; Vanhaecht, B.; Koning, C.E.; Rastogi, S. *Macromolecules* **2006**, 39, 2546-2552.
8. Challa, G., *Plastica* **1969**, 22, 204-208.
9. Harings, J.A.W.; Van Asselen, O.; Graf, R.; Broos, R.; Rastogi, S. *Cryst. Growth Des.* **2008**, 8, 2469-2477.

-
10. Harings, J.A.W.; Van Asselen, O.; Graf, R.; Broos, R.; Rastogi, S. *Cryst. Growth Des.* **2008**, *8*, 3323-3334.
 11. Jones, N.A.; Atkins, E.D.T.; Hill, M.J.; Cooper, S.J.; Franco, L. *Macromolecules* **1996**, *29*, 6011-6018.
 12. Jones, N.A.; Atkins, E.D.T.; Hill, M.J.; Cooper, S.J.; Franco, L. *Polymer* **1997**, *38*, 2689-2699.
 13. Jones, N.A.; Atkins, E.D.T.; Hill, M.J.; Cooper, S.J.; Franco, L. *Macromolecules* **1997**, *30*, 3569-3578.
 14. Nair, S.S.; Ramesh, C.; Tashiro, K. *Macromolecules* **2006**, *39*, 2841-2848.
 15. Li, Y.; Goddard III, W.A. *Macromolecules* **2002**, *35*, 8440-8455.
 16. Katayama, S.; Horikawa, H. *J. Appl. Polym. Sci.* **1971**, *15*, 775-796.
 17. Werner, P.E.; Eriksson, L.; Westdahl, M. *J. Appl. Cryst.* **1985**, *18*, 367-370.
 18. Engel, G.E.; Wilke, S.; Harris, K.D.M.; Leusen, F.J.J. *J. Appl. Cryst.* **1999**, *32*, 1169-1179.
 19. Langer, B.; Schnell, I.; Spiess, H.W.; Grimmer, A.R. *J. Magn. Reson.* **1999**, *138*, 182-186.
 20. Brill, R. *J. Prakt. Chem.* **1942**, *161*, 49-64.
 21. Ando, I.; Asakura, T. *In Solid State NMR of Polymers, Studies in Physical and Theoretical Chemistry*, Vol. 84, **1998**.
 22. Lin-Vien, D.; Colthup, N. B.; Fateley, W. G.; Grasselli, J. G. *In The Handbook of Infrared and Raman Characteristic Frequencies of Organic Molecules*, Academic Press: SanDiego, **1991**.
 23. Grdadolnik, J.; Maréchal, Y. *Appl. Spectrosc.* **2005**, *59*, 1347-1356.
 24. Grdadolnik, J.; Maréchal, Y. *Appl. Spectrosc.* **2005**, *59*, 1357-1364.
 25. Wishart, D.S.; Nip, A.M. *Biochem. Cell Biol.* **1998**, *76*, 1-10.
 26. Wuthrich, K. *In NMR of Proteins and Nucleic Acids*, Wiley: New York, **1986**.
 27. Slichter, C.P. *Springer Series in Solid-State Sciences*, 3rd ed.; Springer-Verlag: Berlin; Vol.1 **1990**.
 28. Levitt, M.H. *In Spin Dynamics: Basics of Nuclear Magnetic Resonance*, 1st ed.; John Wiley & Sons: New York, **2001**.

Chapter 5

Shielding and de-shielding of hydrogen bonding for the development of oriented polyamide crystals; inspiration by natural silk spinning

In natural silk spinning, for instance by spiders and silkworms, ions are amongst several other environmental parameters crucial for mediating the transition from the solubilized random coil into a liquid crystalline helical conformation and into crystalline β sheets successively. Prior to the assembly into β sheets, which give rise to a unique combination of properties, ions inhibit the specific hydrogen bonding. Recently we showed that polyamide crystals can be dissolved in the superheated state of water, forming single crystals on cooling. The presence of ions in the superheated state of water promotes shielding of hydrogen bonding, raising the possibility to obtain amorphous polyamides that can be oriented at room temperature. With increasing ionic strength large non-hydrating (chaotropic) anions, such as bromide and iodide decrease progressively the hydrogen bonding efficiency between the water molecules. This further enhances the diffusivity of water and its solutes, of which the cations assist in perturbation of the hydrogen bonding, and suppresses the dissolution temperature. With the depression of the dissolution temperature, the recrystallization temperature also decreases in the presence of small kosmotropic (hydrating) cations and large chaotropic anions. At high ionic strength hydrophobic hydration enforces the secretion of "hydrophobic" anions to the aliphatic polyamide segments, minimizing the exposed nonpolar surface area. Together with the cations, which interact electrostatically via the first hydration shell with the electron rich amide moieties, a positive and negative charge distribution is formed along the polymer chain that suppresses crystallization in water even at room temperature. Extensional deformation of the obtained viscous aqueous polyamide solution results in oriented structures that prevail by the diffusion of the ions in excess of water and the restitution of amide-amide hydrogen bonding.

5.1 Introduction

The presence of water molecules in biological structures, especially in proteins and nucleic acids, is crucial in all kind of sophisticated processes that sustain life. Dependent on the hydrogen bonding geometries and the location of water molecules, biological structures can be stabilized enthalpically or entropically¹. During evolution water has even adopted an active role in self-assembly phenomena such as protein folding, protein-protein recognition and protein-DNA binding². Here, van der Waals interactions, hydrogen bonding, electrostatic and hydrophobic interactions are the key for sequence-specific DNA recognition by proteins. However, prior to the influence of the direct interactions, water molecules indirectly mediate the recognition and specificity, acting as a guide mapping unfavorable electrostatic forces and hydrogen bonding.

Despite the versatility of water, which is exquisitely used in nature, the use of water in synthetic polymeric structures, such as polyamides, has been scarcely exploited. At elevated temperature it is the disruption of the percolating hydrogen bonded network between the water molecules together with the weakening of van der Waals H₂O-H₂O attraction forces that favor the dissolution of polyamides³⁻⁵. Simultaneously, with increasing thermal motion along the *c*-axis of the polyamide crystals, the efficiency in electron exchange between amide moieties in adjacent crystal stems decreases⁶⁻⁸. The electron exchange between mobile water molecules and amide motifs results in the dissolution of polyamides in the superheated state of water^{3,4}.

On cooling crystallization occurs above the boiling point of water, where a continuous electron exchange between the water molecules and the amide motifs lead to the entrapment of water molecules within the crystal lattice. These physically bound water molecules shield the amide moieties to an extent that changes in the NMR and FTIR spectra are realized^{4,9-11}. A question arises if the shielding of the hydrogen bonding motifs can be used for deformation of the crystals to make oriented structures.

In the case of polymers where the secondary interactions (van der Waals forces) between adjacent stems are weak, for example in polyethylene, crystals can be easily deformed to form oriented chains. However, to achieve high mechanical strength in polymers with weak secondary interactions a high molar mass is required, imposing challenges in processing.

In polyamides the energy required to disrupt the hydrogen bonds that reside between the chain stems is close to the dissociation energy of a covalent carbon-carbon bond, causing difficulties in chain orientation¹². Hence, temporary shielding of hydrogen bonding will facilitate large scale deformation to create oriented structures at room temperature. Re-establishment of strong hydrogen bonding will result in oriented polyamides that are easily processable due to low molar mass.

In the past several attempts in achieving high orientation of polyamides were based on the use of reversible interactions of plasticizers comprising ammonia^{13,14}, iodine^{15,16},

inorganic salts in melt spinning¹⁷⁻²⁰, Lewis acid-base complexes, e.g. GaCl₃²¹ and polar aprotic solvents, all with limited success. Nature shows exquisite examples of highly oriented drawn polypeptides. The crystalline domains in silk, either from spiders or worms, resemble chain folded crystals in synthetic polyamides²². It is reported that prior to spinning ionic interactions and pH in the gland inhibit the hydrogen bonding between adjacent amide moieties²³⁻²⁶. During the spinning process variations in ionic strength and pH determine the ultimate structure development, e.g. liquid crystalline helical conformations and β -sheets, which eventually result in the unique properties. In this paper we investigate the use of superheated water in combination with ions.

5.2 Experimental section

5.2.1 Polyamides, kosmotropic cations and chaotropic anions

Based on the Hofmeister series, a classification that describes to which extend proteins are solubilized or precipitated by the presence of ions in an aqueous environment²⁷, Figure 1.4, solubilizing salts were selected comprising kosmotropic cations like Li⁺, Na⁺ and Ca²⁺ and chaotropic anions such as Cl⁻, Br⁻ and I⁻. Whereas kosmotropic ions order water molecules, chaotropic ions disorder water. Stock solutions, covering the nine possible combinations of ions, were prepared with ionic strengths ranging between 0 and 10 mol/L.

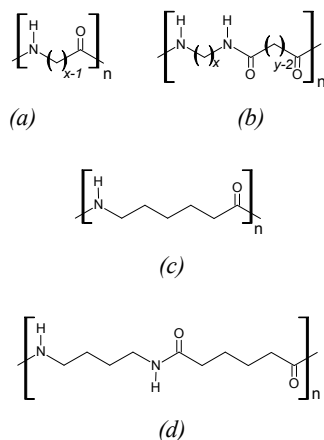


Figure 5.1: General polyamide chemistry and nomenclature. The numbers used in the nomenclature of polyamides (PA_{xy}) represent the number of carbon atoms present in the monomers. A single number *x* represents a di-functional monomer with *x* carbon atoms (a), while two successive numbers *xy* indicate the number of carbon atoms in the mono- functional diamine and diacid or diacyl monomers respectively (b). For example the structural formulas of (c) PA6 and (d) PA46.

5.2.2 Dissolution in superheated water; differential scanning calorimetry

Using differential scanning calorimetry (DSC) the dissolution and precipitation of commercial polyamide (PA) 46 (Stanyl[®], DSM), 6 (Ultramid[®] A, BASF) and 66 (Ultramid[®] B, BASF) in superheated water, whether or not in the presence of ions, was monitored in Perkin Elmer high volume DSC pans under a nitrogen atmosphere. Molecular differences, directly defining the nomenclature, are depicted in Figure 5.1. The cryo-ground polymeric samples were immersed in the aqueous solutions and exposed to a temperature program ranging between 30 and 240°C at a rate of 10°C/min. To ensure an equilibrium state, an isothermal period of 3 min was applied at the temperature limits. Since the evaporation of water is inhibited, the sealed environment facilitates the superheated conditions automatically.

5.2.3 Restoration of hydrogen bonding; crystallization

The reversible nature of the potential shielding effect of the ions, required for ultra-drawing of polyamides, was verified by investigating the polyamide samples obtained as received after the above mentioned temperature profile and after rinsing with distilled water. It has to be noted that rinsing with water induced instant crystallization of the polyamides, as discussed later in paragraph 5.3. Instead of high volume DSC pans an in-house designed pressure cell was used, Figure 5.2. As witnessed by the DSC experiments, dependent on the ionic strength the PA samples either crystallized or remained solubilized. Despite the difference, both types of samples were studied by FTIR spectroscopy, solid state ¹H and ¹³C NMR spectroscopy and time-resolved WAXD.

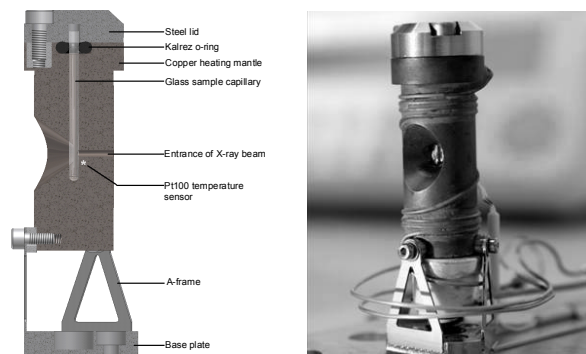


Figure 5.2: Illustration and photograph of the pressure cell, consisting of a copper heating mantle that surrounds a glass tubes, hosting the polymeric sample in aqueous solutions. The system was sealed by a Kalrez O-ring and a steel lid to realize the required water vapor pressure on heating. A Linkam TMS 94 controller was used to control the applied temperature profiles.

5.2.4 Characterization by FTIR, NMR and WAXD

The samples were placed on a zinc selenium disk and the average of 100 FTIR spectra were recorded on a Bio-Rad FTS6000 spectrometer equipped with a microscope with a resolution of 2 cm^{-1} in transmission mode. Solid state ^1H and ^{13}C NMR spectroscopy were performed on a Bruker 700 MHz and a Bruker 500 MHz spectrometer at the Max Planck Institute for Polymer Science (MPIP) in Mainz, Germany. The samples were placed in a 2.5 mm diameter rotor and placed in a solid state MAS probe. Whereas the samples were spun at 30 kHz in ^1H NMR, a frequency of 10 kHz was used in the ^{13}C NMR. Wide angle X-ray diffraction experiments were performed at the high Brilliance beamline ID02, located at the European Synchrotron Radiation Facility (ESRF), Grenoble, France. Two-dimensional diffraction patterns were recorded using a MCP-Sensicam CCD detector having 640×1280 arrays of pixels. The samples were placed in a 1 mm diameter Lindemann capillary and exposed to a temperature profile dependent on the nature of the sample, using a linkam TMS94 hotstage at a heating/cooling rate of $10^\circ\text{C}/\text{min}$. A 12.46 keV ($\lambda = 9.96 \cdot 10^{-2}\text{ nm}$) X-ray beam was used and two-dimensional diffraction patterns of 0.2 s exposure time were collected at every 6 s. The scattered intensity was plotted versus Bragg distance d that was obtained from the modulus of the scattering vector

$$q = |\vec{q}| = (4\pi / \lambda) \sin(\theta / 2) \quad (5.1)$$

and Bragg's law

$$n\lambda = 2d \cdot \sin\theta \quad (5.2)$$

where λ is the wavelength and 2θ is the scattering angle.

5.2.5 Restoration of hydrogen bonding after extensional deformation

Using the pressure cell previously mentioned and sufficient ionic strength to suppress crystallization as revealed by DSC, resulted in viscous polyamide solutions. The solution was transferred to a zinc selenium disk and exposed to extensional deformation using a razor blade. Immediately after deformation, the samples were rinsed with distilled water to remove the ions and crystallization occurred instantly. Orientation was studied by Optical Microscopy (crossed polarizers) and dichroic measurements using polarized FTIR. The polarized FTIR spectra, either parallel or perpendicular to the deformation direction, were recorded on a Bio-Rad FTS6000 spectrometer equipped with a microscope with a resolution of 2 cm^{-1} . Normalization of the crystalline CH_2 scissoring band at 1417 cm^{-1} under the two polarization directions enables the determination of the dichroic ratio

$$D = A_{\parallel} / A_{\perp} \quad (5.3)$$

where A is the maximum absorption in parallel \parallel or perpendicular \perp orientation direction, and the Hermans orientation factor f by

$$\langle P_2(\cos \theta) \rangle = f = [(D-1)/(D+2)] \div \frac{1}{2}(3 \cos^2 \beta - 1) \quad (5.4)$$

in which β is the molecular transition-moment angle. For the crystalline CH_2 scissoring band at 1414 cm^{-1} a transition moment angle of 85° was used²⁸.

5.3 Results and discussion

5.3.1 Influence of ions on the dissolution behavior in superheated water

The dissolution of polyamides in superheated water is dependent on a delicate balance between the weakening of hydrogen bonding in the polymeric crystals and the decrease in hydrogen bonding efficiency between neighboring water molecules. In figure 5.3 the influence of Li^+ and I^- ions on the dissolution processes of PA 46, 6 and 66 is followed for different polymer concentrations. It is evident that the presence of the kosmotropic lithium cations and the chaotropic iodide anions reduces the dissolution temperature. Interpretation of the observations is presented with the help of the Mercedes

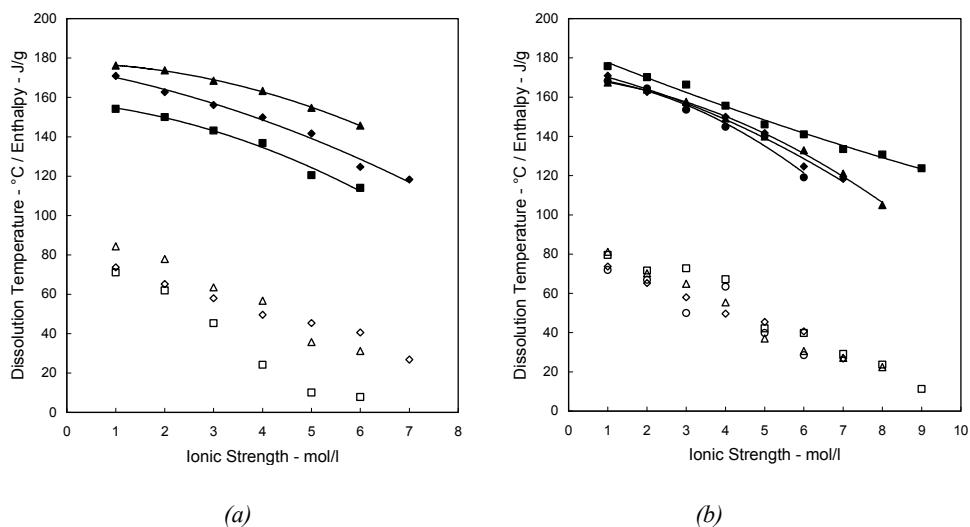


Figure 5.3: (a) The influence of kosmotropic Li^+ and chaotropic I^- ions on the dissolution temperature (closed symbols) and corresponding enthalpies (open symbols) of 29 % w/w (\blacklozenge) PA46, (\blacktriangle) PA66 and (\blacksquare) PA6 in the superheated state of water. (b) Concentration dependence of PA46 dissolution in superheated LiI solutions; (\bullet) 23, (\blacklozenge) 29, (\blacktriangle) 33, and (\blacksquare) 38 % w/w.

Benz (MB) model introduced by Ben-Naim²⁹. In this simplified model water molecules are represented by 2-dimensional disks with 3 radial wings where the interaction energy between adjacent water molecules equals the sum of a Lennard-Jones attraction and repulsion and an orientation dependent hydrogen bonding interaction³⁰, Figure 5.4. Maximum hydrogen bonding efficiency occurs when the radial wings, being a 2 dimensional projection of the actual tetrahedral water structure, of neighboring water molecules are optimally aligned, not discriminating between electron donors and acceptors. Hribar et al. expanded the model by the inclusion of the dipole moment that occurs in water³¹. The dipole moment of water, having a partial negative charge on the oxygen and a partial positive charge on the hydrogen atoms, allows anions to reside in the direct vicinity of water molecules. Since the negative charge of water is localized in the centre of the molecule, cations in comparison with anions of identical size interact relatively poor with water molecules. Furthermore, while the physical behavior of water in the presence of

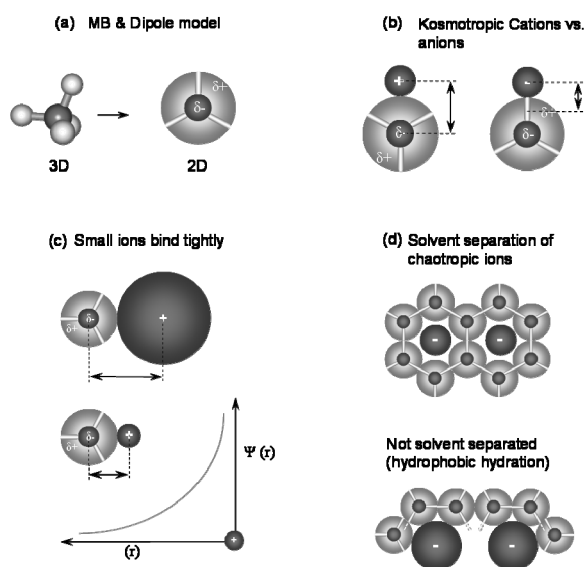


Figure 5.4: The Mercedes Benz model of water. A 2 dimensional model of water in which water molecules are represented by disks, having three radial wings representing a 2D projection of the 3D tetrahedral water structure. Taking the dipole moment of water into account gives a negatively charged centre and a positively charged corona (a). Due to the positively charged corona kosmotropic anions bind stronger to water molecules, or other polar entities, than kosmotropic cations of the same ionic radii (b). In analogy, kosmotropic ions of small radii interact more efficient than kosmotropic ions of large radii since the electrostatic potential ψ decreases exponentially with an increase the ionic radii (c). In the case of chaotropic ions (d), small ions do not perturb the water-water attraction forces such as hydrogen bonding, while large ions do disrupt the organization of water molecules. As a consequence, water tends to cluster the chaotropic components, minimizing the exposed surface area. (Reproduced from Dill et al.²⁷).

small ions is influenced by electrostatic interactions (e.g. orbital overlap), larger ionic radii perturb the hydrogen bonding network in water, explaining the Lennard-Jones relationship.

Iodide is the largest chaotropic anion of the halogens, resulting in the lowest ion-H₂O hydrogen bonding energy, -10.3 ± 0.3 kcal/mol compared to -11.7 ± 0.4 and -14.7 ± 0.6 for Br⁻-H₂O and Cl⁻-H₂O bond energies respectively³². As large chaotropic anions are nonpolar substances, water molecules form a surrounding cage-like solvation shell to maintain maximum water-water hydrogen bonding that in fact is stronger than iodide-water hydrogen bonding³³. Above a critical ionic radius of the chaotropic ion, maximum hydrogen bonding efficiency in the first shell is perturbed by geometrical limitations. The first solvation shell of iodide exhibits only 2.5 hydrogen bonds between water molecules on average, while bulk water possesses 3.4 water-water hydrogen bonds³³. Since not all hydrogen bonded vacancies in water can be used optimally, the overall hydrogen bonding efficiency in water diminishes, especially in solutions with high ionic strength. This means that the diffusion rate of water molecules and its solutes increases significantly at a certain temperature. It is likely that water molecules, assisted by the kosmotropic Li⁺ ions that have a tendency to interact intimately with electron rich species such as the amide motifs, penetrate the polyamide crystals at relatively low temperatures to perturb the hydrogen bonding. In other words, with increasing ionic strength “bulk” water tends to disappear and water only resides in ionic shells. Because of the local disruption of the hydrogen bonded water structure, the water diffusivity enhances and water reaches its superheated or expanded state at lower temperatures. The fact that the enthalpy of dissolution for the same crystallinity of polyamides also decreases with increasing ionic strength, supports the

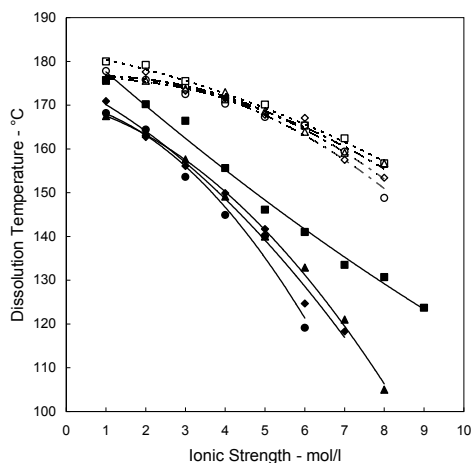


Figure 5.5: Suppression of the dissolution temperature of PA46 in LiI and LiBr solutions (closed and open symbols respectively) at various ionic strengths; (●) 23, (◆) 29, (▲) 33, and (■) 38 % w/w PA46. At identical ionic strengths I⁻ ions suppress the dissolution temperature more effectively than Br⁻ ions.

change in solvent characteristics from bulk to “superheated” state of water in the presence of salts. If the opposed hypothesis is correct, the suppression of the melting temperature will be less in selecting chaotropic anions of smaller atomic radii in the series I^- , Br^- and Cl^- . Figure 5.5 shows the influence of LiBr on the dissolution temperature of polyamide 46 at equal ionic strengths. Since the effect of the bromide ions on the dissolution temperature is less, in comparison with iodide ions at identical ionic strength, the hypothesis stating that the diffusion rate of water and its solutes increases on increasing atomic radius of the chaotropic anions is validated. Not only the ionic radius is smaller, and thus the solvation shell consists of less water molecules, but also the Br^-H_2O binding energy is more effective. At identical ionic strength more bulk water is left in lithium bromide solutions. This means that in this scenario more thermal energy is required to pursue the dissolution of polyamide in water.

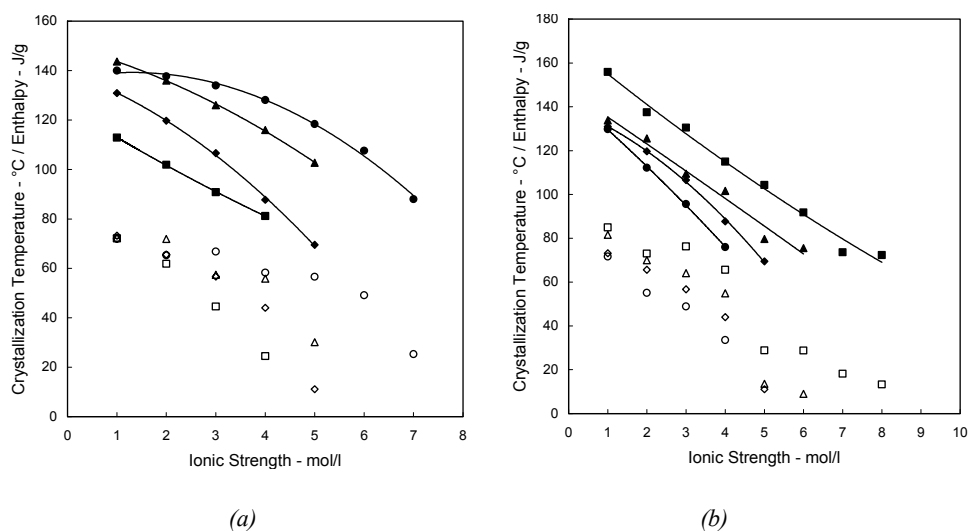


Figure 5.6: (a) The influence of kosmotropic Li^+ and chaotropic I^- ions on the crystallization temperature (closed symbols) and corresponding enthalpies (open symbols) of 29 % w/w (◆) PA46, (▲) PA66 and (■) PA6 in LiI solutions. The crystallization of 29 % w/w PA46 in LiBr solution is presented as well (●). (b) Concentration dependence of PA46 crystallization in LiI solutions of various ionic strengths; (●) 23, (◆) 29, (▲) 33, and (■) 38 % w/w. At high ionic strengths the crystallization of polyamide is completely suppressed.

5.3.2 Shielding of hydrogen bonding on crystallization from the superheated state from water

On cooling the crystallization temperature and corresponding enthalpy are identically influenced by the ions (Figure 5.6). However, dependent on the polymer

concentration crystallization of the polyamides at 30°C is completely suppressed at relatively high ionic strength. The molar ratios salt:amide motifs required to suppress crystallization at 30°C as function of the polymer concentration follows exponential relationships as presented in Figure 5.7. In comparison with polyamide 46 and 66, polyamide 6, in which hydrogen bonding affects the crystal modulus the least, remains solubilized at relatively low ionic strengths. It is to be noted that Gel Permeation Chromatography and FTIR measurements, discussed later, show hardly any hydrolysis within the experimental time scale.

Because of the extremely high solubility of lithium salts in water, though sodium and calcium salts show similar results, Li^+ ions are chosen as kosmotropic cation to reveal the role of the chaotropic anions. The anions, halogenic in nature, were tested with increasing atomic radii. The combination of Li^+ ions with Cl^- ions showed the least effect on the dissolution and (re)crystallization temperature. Suppression of crystallization in LiBr solutions was only observed for polyamide 46, whereas in LiI solutions the crystallization of polyamide 46, 6 and 66 was suppressed. Besides the fact that lithium ions, based on their highly electron deficient character, are expected to exchange electrons with the electronegative carbonyl, these findings suggests a correlation between the atomic radii of the chaotropic anions and the length of the nonpolar methylene segments of the polyamides. Preliminary molecular dynamics simulations reveal, figure 5.12, an indirect shielding effect of Li^+ ions. At ambient conditions extremely efficient Li^+ - H_2O hydrogen bonding results in a rigid first hydration shell, via which the amide moieties are shielded.

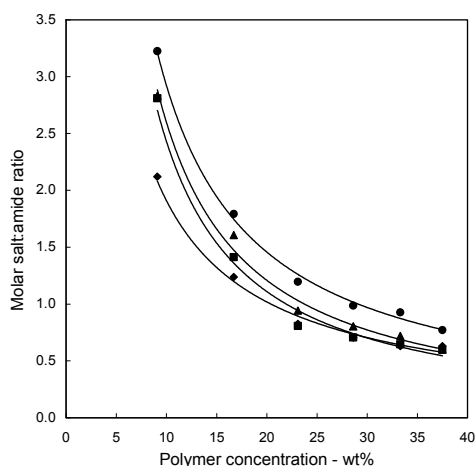


Figure 5.7: The amount of ions per amide moiety, expressed as the molar salt:amide ratio, to solubilize (♦) PA46, (▲) PA66 and (■) PA6 in an aqueous LiI solution at 30°C and PA46 in an aqueous LiBr solution at 30°C as well (●). The exponential trends distinguishes two phases at 30°C, where either sufficient or insufficient ions, above and below the lines respectively, are present to suppress the crystallization completely.

The lithium hydration shell comprises 4 water molecules that have an average residence time of roughly 30 ps (compared to 8-10 ps in iodine solvation shells)³³.

Upon cooling liquid water towards the crystallization or freezing temperature, H₂O-H₂O hydrogen bonding replaces more and more the van der Waals H₂O-H₂O attraction forces in governing the water structure. To minimize the penalty for accommodating large nonpolar species such as the anions, as discussed previously, water enforces clustering of the nonpolar components to decrease the exposed surface area. The higher the penalty in terms of intermolecular water-water hydrogen bonding, the more pronounced is the effect, especially at lower temperatures. A phenomenon known as hydrophobic hydration. Since hydrophobic hydration seems to be correlated to the length of the aliphatic polyamide segments, which are besides apolar in nature as well, anions are likely to be secreted to the aliphatic domains. Due to the charge distribution along the polymer chain, similar to polyelectrolytes, the aqueous polyamide solutions exist even at 30°C.

5.3.3 Re-establishment of hydrogen bonding

The success of the explored route, comprising drawing of polyamides and freezing the desired structure at room temperature by temporary shielding of the hydrogen bonding in the amide moieties, depends on the restitution of the hydrogen bonding. The reversibility of the shielding effect is influenced by the binding efficiency of the ions with the amide motifs and the diffusivity of the ions. The reversibility of hydrogen bonding is investigated for PA 46, 6 and 66 with both insufficient and sufficient ions to suppress crystallization at 30°C, using FTIR, solid state ¹H and ¹³C NMR spectroscopy, and time-resolved WAXD.

Figure 5.8 presents the FTIR spectra of (a) PA46 crystallized from the superheated state of water, (b) PA 46 solubilized in 9M LiBr solutions (ionic strength is 9mol/L) and (c) PA 46 after recrystallization by rinsing out the ions with water. Whereas the crystalline spectra (a) and (c), depicted by the crystalline CH₂ scissoring vibration at 1416 cm⁻¹, are similar, the spectrum of the solubilized polyamide (b) differs significantly. Especially the amide I (C=O stretch) and amide II (C-N stretch and C-N-H bending in-plane) vibrations, which directly reflect the hydrogen bonding efficiency. The low amide I and high amide II wavenumbers indicate that the suppression of crystallization occurs with perturbation of the hydrogen bonding. The presence of the gauche CH₂ scissoring band at 1442 cm⁻¹ and the overall low resolution, in particular below 1500 cm⁻¹, stresses the amorphous/ solubilized state. Rinsing with excess of water induces instant crystallization of the polyamide as depicted by the similarities with the water crystallized PA 46 spectrum. The absence of a carboxylic carbonyl vibration in the range from 1800 to 1700 cm⁻¹ in spectrum (c) indicates that hydrolysis did not occur within the experimental time scale.

Besides FTIR spectroscopy, the reversibility of the shielding effect is also

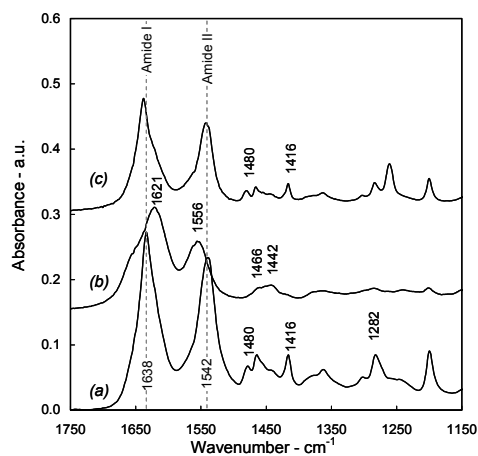


Figure 5.8: FTIR spectra representing the reversible nature of the shielding of hydrogen bonding in the presence of Li^+ and Br^- ions. As a reference spectrum (a) represents PA46 crystallized from superheated water. Via the amide I and II vibrations spectrum (b) demonstrates the implications of the ions on the hydrogen bonding efficiencies in the aqueous polyamide solution, while spectrum (c) shows the reestablishment of hydrogen bonding by the diffusion of ions in excess of water.

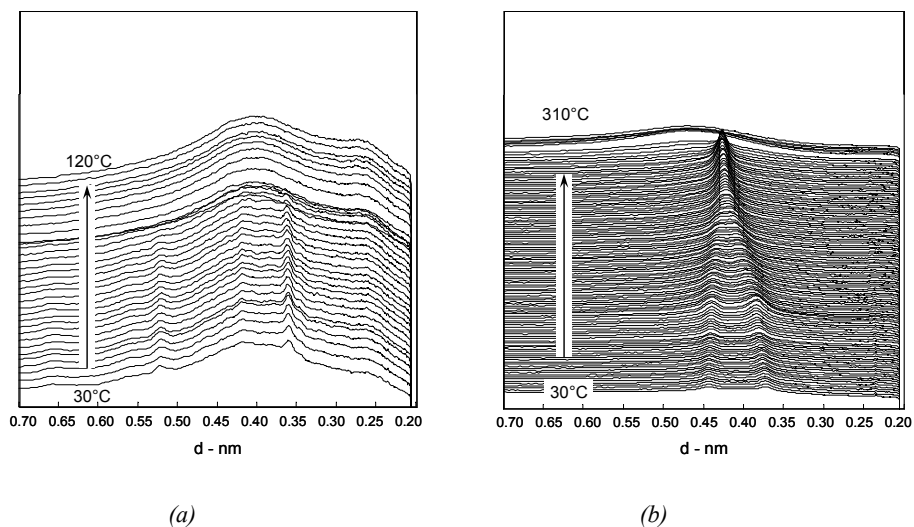


Figure 5.9: Time-resolved WAXD of (a) a metastable PA46- Li^+ / Br^- complex, which contains insufficient ions to suppress crystallization completely, that melts at 80°C upon heating. After the reestablishment of hydrogen bonding by immersion in excess water, the specific temperature dependant structural behavior of PA46 is shown in Figure (b) by the interchain/intrasheet and interchain/intersheet diffraction signals that merge prior to melting at 293°C .

demonstrated by X-ray diffraction. A molar salt: amide motif ratio below the exponential curves (Figure 5.7), i.e. insufficient ions to suppress crystallization completely, results in some resolved diffraction signals that represent structural order, while the superimposed broad halo indicates the presence of a significant amorphous component. The apparent metastable PA 46-ion complex melts at 80°C on heating, witnessed by vanishing of the weakly defined diffraction signals, and does not crystallize on cooling to 30°C. Immersion in excess of water, allowing the ions to diffuse from the polymer, results in crystallization of the polymer. It is to be noted that the X-ray diffraction pattern recorded at 30°C depicted in Figure 5.9a is very different than the one depicted for the same temperature in Figure 5.9b. The reversible nature of the concept is further verified by investigating the anticipated structural changes in polyamides on heating. Figure 5.9b reveals the specific physical behavior of polyamide 46 where on heating the interchain/intrasheet and interchain/intersheet distances at 0.44 and 0.37 nm respectively merge prior to melting at approximately 300°C - this merger point is known as Brill transition.

Solid state ^{13}C NMR spectra of (a) PA 46 crystallized from the superheated state of water, (b) PA 46 with insufficient amount of LiBr and (c) recrystallized on the removal of the ions are presented in Figure 5.10. All spectra are recorded at room temperature. In the ^{13}C spectra the amorphous state is confirmed by the typical amorphous α_{N} and β_{N} CH_2 signals at 39.6 and 26.3 ppm respectively, combined with the increased chemical shift of the carbonyl signal to 176.5 ppm that originates in lesser shielding of its carbon nuclei by shielding of the hydrogen bonding.

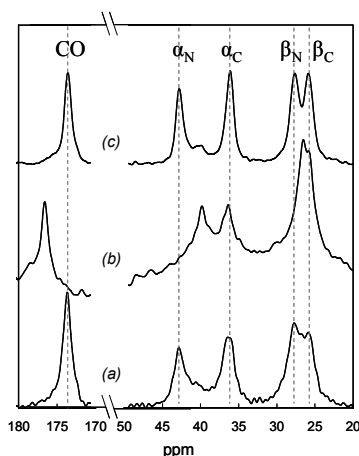


Figure 5.10: Solid state ^{13}C CP-MAS spectra of (a) PA46 crystallized from the superheated state of water as reference, (b) a metastable PA46- Li^+/Br^- complex where the amorphous nature is expressed by the enhanced mobility and changes in the chemical environments and (c) the restoration of hydrogen bonding PA46 after immersion in excess of water.

Immersion of the metastable phase in excess of water results in the reestablishment of hydrogen bonding as depicted by the ^{13}C carbonyl signal that adopts the crystalline chemical shift³⁴. The slightly decreased mobility in the proton spectra, though the peaks are shifting towards the crystalline positions, suggests that some ions still reside in the vicinity of the polyamide. Apparently the diffusivity of the ions in the relatively dense metastable state limits the complete exclusion of ions within the experimental time scale. Nevertheless, the shielding and reestablishment of hydrogen bonding in the presence of less Li^+ and Br^- ions, forming a metastable PA46- Li^+/Br^- complex, is reversible as well.

Extensional deformation of viscous aqueous polyamide solutions, which thus contain sufficient ions to suppress crystallization at 30°C , followed by freezing the structure by diffusion of ions in excess of water, forms the structures presented in the optical micrographs (Figure 5.11, inlay). Rotating the sample with an angle of 45° induces the (dis)appearance of highly birefringent fibrils. The birefringence arises from the direction of the polarized light changing from parallel to perpendicular to the orientation direction of the samples. In figure 5.11 typical polarized FTIR spectra of polyamide 46 fibrils are presented, where the polarization direction is either parallel (0°) or perpendicular (90°) to the orientation of the chains. The Hermans orientation factor f_H , indicating orientation on molecular level, of the crystalline CH_2 scissoring band at 1417cm^{-1} reached a value of 0.93. The dilute polyamide solutions can be extensionally deformed into aqueous polyamide filaments, but structural strength is lost on crystallization. To circumvent this loss in strength an alternative route has been adopted in the following chapter.

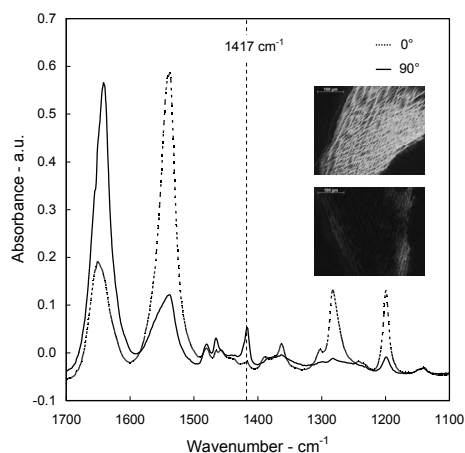


Figure 5.11: Polarized FTIR spectra of the dichroic measurements, in which the difference in absorbance of the crystalline CH_2 scissoring vibration at 1417cm^{-1} between the parallel (0°) and the perpendicular (90°) orientation direction was used to determine the Hermans orientation factor. The inlay consists of two optical micrographs stressing the chain orientation by the change in birefringence on a 45° sample rotation between crossed polars.

5.4 Conclusions

The presence of large chaotropic halogenic anions perturbs the hydrogen bonding network in water. With increasing ionic strength the overall hydrogen bonding efficiency in water weakens to such an extent that the diffusivity of water and its solutes increases. Water molecules, assisted by small kosmotropic cations, having enhanced diffusivity in superheated or expanded state penetrate the polyamide crystals at relatively low temperatures, resulting in complete dissolution. The combination of kosmotropic cations and chaotropic anions influences the crystallization temperature. At relatively high ionic strength the crystallization of the polyamide 46, 6 and 66 is suppressed completely and amorphous polyamides can be obtained at 30°C. Minimizing the penalty for the accommodation of large anions, sufficiently large to perturb intermolecular water-water hydrogen bonding, the anions are clustered near the aliphatic domains in the polyamide by hydrophobic hydration. Due to hydrophobic nature of the methylene sequences, between the amide motifs in polyamides, the hydrogen bonded network of the surrounding water molecules is perturbed as well. The distribution of positive (near the amide moieties) and negative (near the methylene segments) charges along the polymer backbone suppresses crystallization even at room temperature.

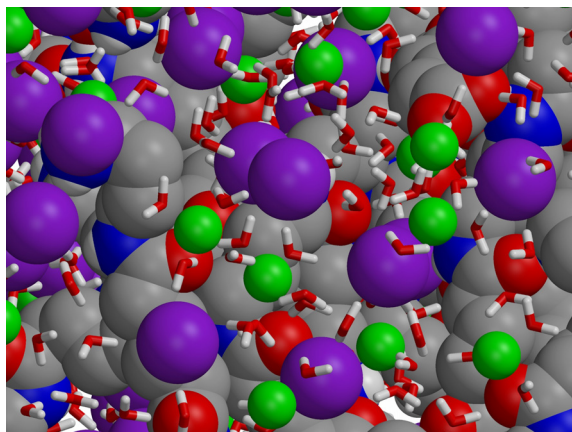


Figure 5.12: Molecular dynamics simulations by Berk Hess (MPI-P, Mainz), probing the indirect shielding of hydrogen bonding by the hydration shell of Li^+ ions in the solubilized state. Carbon is grey, nitrogen blue, oxygen red, iodine purple and lithium green. The water molecules are moreover presented in stick model. (Courtesy: Berk Hess)

Dependent on the ionic strength and the polymer concentration a metastable polyamide-ion complex, with a strongly reduced melting temperature, or an aqueous polyamide solution is obtained. The success of the ultra-drawing of polyamides having

shielded hydrogen bonding motifs relies on the restitution of the interchain/intrasheet amide-amide hydrogen bonding. This is achieved by the removal of ions by immersion of the extensionally deformed metastable polyamides in excess of water. With the instant reestablishment of hydrogen bonding the orientation is prevailed in highly birefringent polyamide fibrils, though strength of the oriented fibrils is lost on the induction of crystallization with the removal of ions. A cause for such a loss in strength can be attributed to the absence of chain overlap between the crystals. To achieve high strength after crystallization an alternative route for spinning is explored in the following chapter. The proposed concept can be applied in a range of hydrogen bonded polymers-providing a route to obtain high strength wovens.

5.5 References

1. Jeffrey, G.A.; Saenger, W. *In Hydrogen Bonding in Biological Structures*, Springer-Verlag Berlin Heidelberg, **1994**.
2. Levy, Y.; Onuchic, J.N. *Annu. Rev. Biophys. Biomol. Struct.* **2006**, 35, 389-415.
3. Rastogi, S.; Terry, A.E.; Vinken, E. *Macromolecules* **2004**, 37, 8825-8828.
4. Vinken, E.; Terry, A.E.; Van Asselen, O.; Spoelstra A.B.; Graf, R.; Rastogi, S. *Langmuir* **2008**, 24, 6313-6326.
5. Challa, G. *Plastica* **1969**, 22, 204-208.
6. Yoshioka, Y.; Tashiro, K.; Ramesh, C. *Polymer* **2003**, 44, 6407-6417.
7. Yoshioka, Y.; Tashiro, K. *J. Phys. Chem. B.* **2003**, 107, 11835-11842.
8. Vinken, E.; Terry, A.E.; Hoffmann, S.; Vanhaecht, B.; Koning, C.E.; Rastogi, S. *Macromolecules* **2006**, 39, 2546-2552.
9. Harings, J.A.W.; Van Asselen, O.L.J.; Graf, R.; Broos, R.; Rastogi, S. *Cryst. Growth Des.* **2008**, 8, 2469-2477.
10. Harings, J.A.W.; Van Asselen, O.L.J.; Graf, R.; Broos, R.; Rastogi, S. *Cryst. Growth Des.* **2008**, 9, 3323-3334.
11. Hess, B.; Harings, J. A. W.; Rastogi, S.; Van der Vegt, N. F. A. *J. Phys. Chem. B.* **2009**, 13, 627-631.
12. Postema, A.R.; Smith, P.; English A.D. *Polym. Comm.* **1990**, 31, 444-447.
13. Zachariades, A.E.; Porter R.S. *J. Appl. Pol. Sci.* **1979**, 24, 1371-1382.
14. Kanamoto, T.; Zachariades, A.E.; Porter, R.S. *J. Appl. Polym. Poly. Phys. Edn.* **1982**, 20, 1485-1496.
15. Chuah, H.H.; Porter, R.S. *Polymer* **1986**, 27, 1022-1029.
16. Lee, Y.H.; Porter, R.S. *J. Macromol., Sci., Phys. B* **1995**, 34, 295-309.
17. Acierno, D.; Bianchi, E.; Ciferri, A.; Cindio, B.; Migliaresi, C.; Nicolais, L. *J. Polym. Sci. Polym. Symp.* **1976**, 54, 259-269.

-
18. Acierno, D.; Lamantia, F.P.; Polizzotti, G.; Ciferri, A. *J. Polym. Sci. Polym. Phys. Edn.* **1979**, 17, 1903–1912.
 19. Ciferri, A.; Acierno, D.; Alfonso, G.C. *Patent US4167619* **1979**.
 20. Richardson, A.; Ward, I.M. *J. Polym. Sci., Polym., Phys. Edn.* **1981**, 19, 1549–1565.
 21. Vasanthan, N.; Kotek, R.; Jung, D.W.; Shin, D.; Tonelli, A.E.; Salem, D.R. *Polymer* **2004**, 45, 4077-4085.
 22. Van Hest, J.C.M.; Tirrell, D. *Chem. Comm.* **2001**, 1897-1904.
 23. Dicko, C.; Vollrath, F.; Kennedy, J.M. *Biomacromolecules* **2004**, 5, 704-710.
 24. Zhou, L.; Chen, X.; Shao, Z.; Huang, Y.; Knight, D.P. *J. Phys. Chem. B.* **2005**, 109, 16937-16945.
 25. Holland, C.; Terry, A.E.; Porter, D.; Vollrath, F. *Nature Mat.* **2006**, 5, 870-874.
 26. Wong Po Foo, C.; Bini, E.; Hensman, J.; Knight, D.P.; Lewis, R.V.; Kaplan, D.L. *Appl. Phys. A* **2006**, 82, 223-233.
 27. Dill, K.A.; Truskett, T.M.; Vlachy, V.; Hribar-Lee, B. *Annu. Rev. Biophys. Biomol. Struct.* **2005**, 34, 173-199.
 28. Cole K.C.; Depecker, C.; Jutigny, M.; Lefebvre, J.M.; Krawczak, P. *Pol. Eng. Sci.* **2004**, 44, 231-240.
 29. Ben-Naim, A. *In Water and Aqueous Solutions Plenum*, New York, **1974**.
 30. Silverstein, K.A.T.; Haymet, A.D.J.; Dill, K.A. *J. Am. Chem. Soc.* **2000**, 122, 8037-8041.
 31. Hribar B.; Southall N.T.; Vlachy V.; Dill, K.A. *J. Am. Chem. Soc.* **2002**, 124, 12302-13311.
 32. Hiraoka, K.; Mizuse, S.; Yamabe, S. *J. Phys. Chem.* **1988**, 92, 3943-3952.
 33. Heuft, J.M. *In An ab initio study of ion solvation in water*, PhD Thesis Van t' Hoff Institute for Molecular Sciences, Faculty of Science, University of Amsterdam, The Netherlands, **2006**.
 34. Ando, I.; Asakura, T. *In Solid State NMR of Polymers, Studies in Physical and Theoretical Chemistry*, Vol. 84, **1998**.



Chapter 6

Strain induced crystallization of polyamide 46 from aqueous lithium iodide solution; a technological assessment

The calculated chain modulus for polyamides is close to 250 GPa. However, the cooperative energy of hydrogen bonds between adjacent lamellar stems prevents lamellar crystal deformation into extended chain crystals, limiting the success of polyamides in high strength and high modulus applications. In this chapter a new reversible plasticization route to shield the hydrogen bonding temporarily is explored. Attempts in the past failed because of selective absorption of shielding agents, ineffective drawing due to chain slippage and inefficient removal of shielding agents. In this chapter it is shown that amorphous polyamide 46 samples, possessing a glass transition temperature in the proximity of 20°C, can be extruded from the superheated state of water in the presence of Li⁺ and I⁻ ions. Strain induced crystallization by drawing, preferably in water above the glass transition temperature and eventually quenched in cold water, results in restoration of hydrogen bonding, high orientation factors, up to 0.99, and lattice perfection where the spacings adopt single crystal values. However, the crystallinity and the melting temperature are considerably suppressed in the presence of ions. Time-resolved X-ray experiments reveal that the migration of ions is primarily time dependent at temperatures above the glass transition temperature. Upon efficient removal of ions in the superheated state of water at 150°C, the high orientation and crystal perfection are preserved. With the removal of ions the crystallinity increases to 53% and the melting temperature to 289°C. However, from the reported studies one cannot conclude whether extended chain crystals are present.

6.1 Introduction

High performance fibers of polymeric origin benefit from the high energy required to distort covalent bonds along the molecular axis in the extended chain crystals. Due to the resulting high modulus and strength combined with low specific weights, this class of materials is nowadays successfully used in various lightweight applications¹. The idea of single chain deformation, resulting in entropy driven rubber elasticity on removal of the applied forces, was first postulated by Treloar. His calculations further showed that deformation of an individual fully extended polyethylene or polyamide molecule, which in reality does not exist, requires deformation of bond lengths and bond angles, raising the elastic modulus of the single chain tremendously². Due to the small dimensions of a polymer molecule, that is less than 10 microns in length and roughly 1 nm in diameter for the most simple polymer polyethylene (PE), ideal alignment of the ensemble of chains in the fiber direction and sufficient chain overlap/intermolecular interaction for adequate stress transfer is required³. However, it is crucial to realize the anisotropic nature of strong and weak modulus along and perpendicular to the chain axis, respectively. Thus the ultimate performance in polyethylene is limited to the axial or fiber direction.

Freezing of flexible polymers in extended chain conformation is also hindered by the rotational freedom of C-C bonds. Upon extensional deformation polymer chains tend to relax to adopt the thermodynamically favorable random coil conformation. To evade entropy arising due to loss of chain alignment, rigid or semi-rigid polymer molecules such as poly(*p*-phenylene benzobisoxazole) (PBO), poly(*p*-phenylene terephthalamide) (PPTA) or poly(pyridobisimidazole) (PIPD), Figure 6.1, can be used for high demanding applications^{1,4}. Though small amounts of single bonds may introduce rotational motion in these aromatic polymers, the contour of the molecule is hardly affected as the rigidity dominates. Due to the intrinsic chain stiffness, a small difference in entropy between crystalline and liquid state increases the melting temperature beyond the degradation temperature. As a consequence these (semi-) rigid polymers are processed via solution routes. In solution, with the increasing concentration of the polymer, the rigid molecular contour triggers the formation of lyotropic liquid crystalline solutions, promoting chain alignment at the same time. Though the molecular weights are limited, secondary interactions, such as hydrogen bonding interactions (15-120 kJ/mol)⁵, promote adequate chain interaction to maintain structural integrity, thus yielding a modulus that approaches the maximum calculated elastic modulus in the case of PPTA for instance⁶.

An exquisite example where chain relaxation due to entropy in a flexible polymer could be overcome is ultra high molecular weight polyethylene (UHMWPE). In this specific scenario the calculated polymer modulus of 220 GPa, as determined by Nakamae and Nishino⁶, is obtained in reality as well. This value of modulus is obtained due to crystallization of the PE chains in fully extended chain conformation on post drawing of the solution spun fibers below their melting temperature. Desired high molecular weights in

PE are inevitable to achieve the high modulus since the intermolecular van der Waals attraction forces are in the order of 5 kJ/mol or less and ideal stress transfer is only reached if the sum of the intermolecular secondary interactions equals at least the covalent bond energies in the main chain. However, due to the presence of entanglements above a critical molar mass the zero-shear viscosity scales with M^3 . Considering the average molar mass between entanglements, in the region of 1500g/mol, the number of entanglements present in UHMWPE (where average molar mass is greater than a million g/mol) exceeds 600, causing processing of the polymer melt via conventional means near impossible. To reduce the number of entanglements per chain, solution spinning of the dilute solutions of UHMWPE is used. The presence of solvent imposes challenges in processing⁷⁻¹¹. Recently, a route for the development of disentangled PE chains, based on controlled synthesis, was introduced^{12,13}.

Considerable efforts have been made in the use of polyamides, where depending on the amide density, calculated polymer moduli around 250 GPa could be achieved⁶. The interchain hydrogen bonding between adjacent amide motifs introduces high temperature resistance and may overcome creep, which is slippage of the chains and eventual fiber failure under long term stress parallel to the chain axis. However, hydrogen bonding that prevails even in the melt hinders the formation of extended chain polyamide crystals. It has to be realized that the energy required to disrupt the hydrogen bonds that reside between the crystalline chain stems is close to the dissociation energy of a covalent carbon-carbon bond¹⁵. The maximum draw ratio is therefore determined by the presence of hydrogen bonding acting as physical constraints and is limited to 5, independent of temperature¹⁵. The eventual elastic modulus of polyamide is generally only 5% of the calculated value.

Perturbation of amide-amide hydrogen bonding, which is close to 35 kJ/mol at an interchain distance of roughly 0.4 nm, facilitates the large scale deformation upon drawing that is required to obtain maximum chain alignment. Fully extended chain conformations, essential for ultimate mechanical properties, can be preserved by restitution of the hydrogen bonding. Reversible plasticization attempts so far are based on ammonia^{16,17}, iodine^{18,19}, inorganic salts in melt spinning²⁰⁻²³, Lewis acid-base complexes such as GaCl_3 ²⁴ and polar aprotic solvents. Selective absorption of shielding agents in the amorphous phase only, inefficient removal of the plasticizing/shielding agent or ineffective drawing by chain slippage rather than chain extension are considered to be the main reasons for the limited success. The highest elastic modulus, 23.4 GPa, was reported by Jung et al. using nylon 66 plasticized with GaCl_3 ²⁵. Gupta et al. developed recently a successful electro-spinning process for porous polyamide 6 filaments using GaCl_3 shielding²⁶. Even then the elastic modulus of the thus obtained extrudates, hardly reaches 10% of the calculated polymer modulus.

In chapter 5, a novel concept based on the dissolution of polyamides in the superheated state of water²⁷⁻²⁸ and inspired by natural silk spinning²⁹ in shielding of the hydrogen bonding has been introduced. At this point it is useful to recall some of the

prominent findings. With increasing ionic strength, large chaotropic anions, being non-hydrating in nature, promote the diffusivity of water molecules. Hence, the superheated or expanded state of water is reached at relatively low temperature, suppressing the dissolution temperature of polyamides. With depression of the dissolution temperature, the recrystallization temperature also decreases in the presence of small kosmotropic (hydrating) cations and large chaotropic anions. At high ionic strength hydrophobic hydration enforces the secretion of “hydrophobic” anions to the aliphatic polyamide segments. With the cations, which interact via the first hydration shell with the electron rich amide moieties, a charge distribution is formed along the polymer chain that suppresses crystallization even at room temperature. Extensional deformation of the aqueous polyamide solution results in oriented structures that prevail by efficient diffusion of the ions in excess of water and the restitution of amide-amide hydrogen bonding. However, although oriented structures were obtained, strength of the oriented fibrils was lost on the induction of crystallization, possibly caused by the absence of chain overlap between the crystals. Adopting the proposed route, the present chapter presents a structural development for higher polymer concentrations, promoting chain overlap during crystallization. Moreover, water combined with ions of the Hofmeister series may mediate crystallization and eventual structure development³⁰⁻³³.

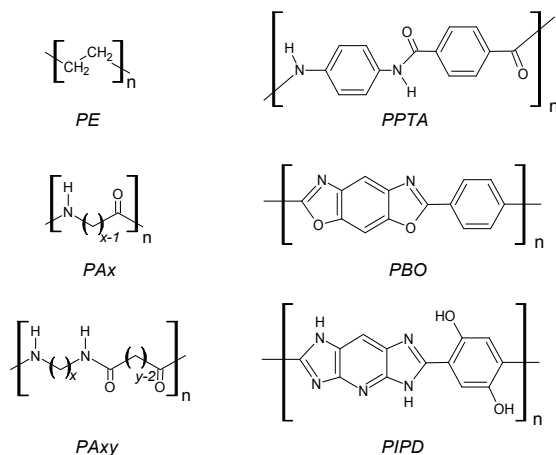


Figure 6.1: Chemical structures of flexible and (semi-)rigid polymers. The flexible polymers comprise polyethylene and polyamides (PA) of which the latter is divided in two categories, namely polyamide x and polyamide xy . Polyamides with a single number, here denoted with x , are made of a di-functional monomer with x carbon atoms such as caprolactam in PA6. Two numbers, represented by xy , indicate that the polyamide is synthesized from two mono-functional monomers, a diamine and a diacid or diacyl with x and y carbon atoms respectively. Poly(p -phenylene terephthalamide), poly(p -phenylene benzobisoxazole) and poly(pyridobisimidazole) are examples of (semi-)rigid polymers that due to the rigid contour can be spun from lyotropic liquid crystalline solutions, promoting chain alignment.

6.2 Experimental section

6.2.1 Materials and sample preparation

Commercial polyamide 46 (Stanyl[®] KS300) and lithium iodide beads were supplied by DSM and Aldrich respectively. A premix of 84% w/w PA46 and 16% w/w 9M LiI solution was prepared and fed to an Haake Rheomex OS PTW 16 co-rotating twin screw extruder having a screw configuration as depicted in Figure 6.2. Feeding was torque controlled at 80% of the maximum, 130 Nm, at a screw speed of 100 rpm. The temperature profile ranged from 325°C in the first zone to 240°C in the last zone, resulting in an extrudate temperature of 240°C at the die. It has to be noted that dissolution in the superheated state of water and the presence of Li⁺ and I⁻ ions facilitate extrusion at temperatures well below conventional PA46 processing temperatures. The transparent extrudate was collected carefully to minimize pre-orientation induced by the extrusion process. As a reference polyamide 46 extrudates were prepared identically resulting in semicrystalline samples (PA46sc). However, the temperature zones were set from 325°C in the first zone to 300°C in the last zone, resulting in an extrudate temperature of 310°C at the die. Samples from the LiI (PA46LiI) and the melt route (PA46sc) were drawn successively by hand in air and water at 20, 55 and 95°C.

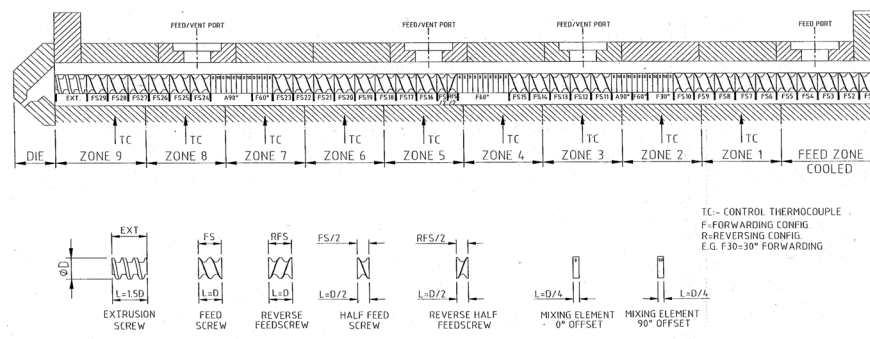


Figure 6.2: Screw configuration of the co-rotating twin-screw extruder characterized by several mixing and reverse screw elements, providing the pressure required for dissolution of PA46.

6.2.2 Dynamic mechanical thermal analyses

The PA46 extrudates obtained from the melt and LiI route were measured at on a TA DMA Q800 with a tension setup. A temperature sweep from -50 to 350°C was applied with a heating rate of 3°C/min at a frequency of 1 Hz. A preload force of 0.01 N, an amplitude of 10 μm and a force track of 110% were used.

6.2.3 Tensile testing

The drawing behavior of PA46sc and PA46-LiI extrudates, being less than 0.5 mm diameter, was monitored at 5 mm/min using a ZwickZ100 tensile tester equipped with a 100 N load cell and 0.1 N preload. As the initially transparent PA46LiI filaments became white on tensile deformation, suggesting strain induced crystallization or micro crazing, the influence of drawing was evaluated by a second, identical tensile test immediately after breakage of the samples. The influence of draw rate was furthermore monitored on a Textechno Favimat tensile tester using draw rates ranging between 20 and 240 mm/min. As a reference, strain induced crystallization and molecular orientation of the PA46 melt extrudate as function of draw ratio A was also investigated by preparing samples with different draw ratios.

The influence of drawing media, either air or water, and temperatures on the eventual mechanical performance was investigated by testing the extensively dried samples (30°C under vacuum) at 2 mm/min using an Instron 5564 tensile tester equipped with a 2 kN load cell and pneumatic action grips.

6.2.4 Differential scanning calorimetry

Crystalline structure development on drawing, whether or not with efficient removal of ions, was investigated by exposing the samples to two successive temperature profiles, ranging from 5 to 325°C at a rate of 10°C/min and 3 minutes of isothermal conditions at the temperature limits. The experiments were performed on a TA Q1000 DSC apparatus under nitrogen atmosphere. Crystallinity X_C was determined by the quotient of the measured heat of fusion in the first temperature cycle $\Delta H_{exp.}$ and 210 J/g, the heat of fusion of a 100% crystalline PA46 $\Delta H_{100\%}$ ³⁴, as given by equation 6.1.

$$X_C = \frac{\Delta H_{exp.}}{\Delta H_{100\%}} \cdot 100\% \quad (6.1)$$

6.2.5 Solid state ⁷Li nuclear magnetic resonance spectroscopy

Solid state ⁷Li MAS NMR spectroscopy was used to probe the dissociation of the LiI salt in the PA46LiI extrudates using a Bruker 500 MHz spectrometer (11.75 T) at the Max Planck Institute for Polymer Science (MPIP) in Mainz, Germany. ⁷Li NMR spectra of PA46LiI sample (the as extruded), LiBr and LiI were recorded at ambient temperature employing a 2.5 mm probe, a spinning speed of 25.0 kHz and ¹H decoupling during acquisition.

6.2.6 Wide angle X-ray diffraction

Wide angle X-ray diffraction was used to follow structure development as function of draw ratio in different environments and as function of the migration efficiency of ions from the samples. Whereas the effect of drawing media and temperatures was studied by means of wide angle X-ray diffraction experiments at the Dutch/Belgium beamline BM26b (DUBBLE), the migration of ions from oriented samples was evaluated at the high resolution Materials Science Beamline ID11, both located at the European Synchrotron Radiation Facility (ESRF), Grenoble, France. At BM26b two-dimensional diffraction patterns were recorded using a Frelon CCD detector, employing a 10.3 keV ($\lambda = 0.120$ nm) X-ray beam of $200 \times 200 \mu\text{m}^2$ size and 3 s acquisition time.

A Frelon 4M CCD camera was used at ID11 to collect two-dimensional diffraction patterns that were acquired using a 29.8keV ($\lambda = 0.417$ nm) X-ray beam of $50 \times 200 \mu\text{m}^2$ size and 10 s exposure time. The drawn PA46sc and PA46LiI filaments were placed in glass capillaries and immersed in distilled water. The filled capillaries were then placed in the pressure cell presented in chapter 5, Figure 5.2, and exposed to a temperature cycle ranging between 30 and 150°C at a rate of 5°C/min, using a Linkam TMS 94 temperature controller. As a calibration standard lanthanum hexaboride was used. The diffraction patterns were corrected for background scattering and detector response both by subtraction. Azimuthal integration over the arc range of individual diffraction arcs lead to the intensity against the scattering vector q . The relation $d = 2\pi/q$ was used to convert the scattering into d -spacing.

6.2.7 Polarized infrared spectroscopy

Orientation of the drawn samples was studied by dichroic measurements using polarized FTIR. The polarized FTIR spectra of 20 μm thick slices were recorded either parallel or perpendicular to the orientation direction using a Bio-Rad FTS6000 spectrometer equipped with a microscope and a resolution of 2 cm^{-1} . Normalization of the crystalline CH_2 scissoring band at 1417 cm^{-1} under the two polarization directions enables the determination of the dichroic ratio and the Herman's orientation factor f , as given by equation 5.3 and 5.4 in chapter 5. For the crystalline CH_2 scissoring band at 1414 cm^{-1} a transition moment angle of 85° was used³⁵.

6.3 Results and discussion

6.3.1 Crystal and orientation development in semicrystalline PA46 at ambient conditions

The presence of hydrogen bonding in polyamide crystals, arising due to a decrease in entropy and hence an increase in melting temperature, prevents chain deformation to form extended chain crystals. The hydrogen bonded crystallites, which are interspersed in an amorphous matrix, act as physical constraints that limit the drawability to a maximum draw ratio of 5^{15} . To evaluate the structure formation in the PA46-LiI samples as function of draw ratio in a later stage of this chapter, this paragraph discusses the crystal and orientation development of semicrystalline PA46 (PA46sc) as a basis.

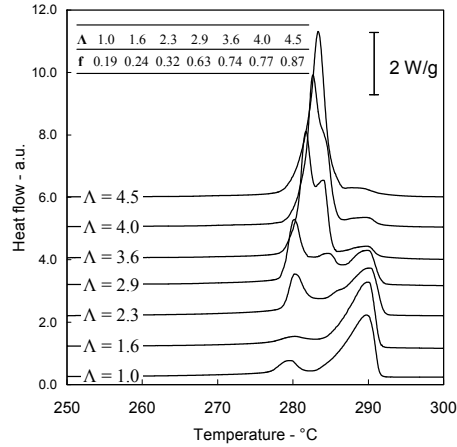


Figure 6.3: DSC thermograms of semicrystalline polyamide 46 samples. Influence of draw ratio Λ on melting characteristics is illustrated. The inlay shows the Herman's orientation factors f obtained at different draw ratios.

Figure 6.3 depicts the effect of draw ratio on the melting behavior of semicrystalline PA46 by DSC and reveals two melting peaks at 279.5 and 289.8°C for the undrawn sample ($\Lambda = 1$). Following the Gibbs-Thomson equation for lamellar crystals, expressed in equation 6.6, the presence of two melting peaks may arise from lamellar crystals of different thickness.

$$T_m = T_m^\infty \left(1 - \frac{2\sigma_e}{l \cdot \rho \cdot \Delta H_m} - \frac{2\sigma}{A \cdot \rho \cdot \Delta H_m} - \frac{2\sigma}{B \cdot \rho \cdot \Delta H_m} \right) \quad (6.6)$$

Here, T_m is the experimental melting temperature, T_m^∞ is the equilibrium melting temperature for infinite perfect crystals, σ_e is the surface free energy of the fold planes, σ is the surface free energy of the lateral planes, l is the crystal thickness in chain direction or fold length, ΔH_m is the heat of fusion, ρ is the crystal density, and A and B are the lateral crystal dimensions. Since the lateral dimensions of melt and solution crystallized samples are relatively large in size, the last two terms of the Gibbs-Thomson equation are often ignored. As a consequence the melting temperature is only related to the thickness of the lamellae. Thus, if the fold l length increases, the experimental melting temperature increases as well.

Upon deformation in the solid state (below melting temperature), eventually up to a value of 4.5, a single melting peak at (283.3°C, 100.2 J/g) appears at the expense of the two melting peaks observed in the undrawn sample. Since hydrogen bonding limits the deformation of the polyamide crystals, it could be expected that the crystals representing the higher melting temperature in the undrawn sample should prevail upon further deformation. However, the higher melting peak vanishes upon solid state deformation and appears once again when the deformed sample is recrystallized from the melt, indicating that the higher melting peak arises due to recrystallization upon heating in DSC³⁶.

Fast cooling of the melt extrudate below the glass transition temperature hinders the crystallization of the polyamide, resulting in a heat of fusion of only 7.2 J/g for the undrawn sample. Low heat of fusion suggests poor crystallinity of 3.4% only. At the maximum draw ratio of 4.5 below the melting point the crystallinity changes from 3.4% to 47.8%. Strain induced crystallization upon deformation results in increasing Herman's orientation factors (from 0.19 to 0.87) as given in the inlay of Figure 6.3.

6.3.2. Characterization of semicrystalline and amorphous samples

To assess the proposed route, based on the suppression of polyamide crystallization from the superheated state of water in the presence of lithium and iodide ions, the dissociated state of the ions has to be confirmed. In figure 6.4 the chemical environment of lithium in the PA46LiI sample is compared with the chemical environments of LiI and LiBr salts. The narrow line width of the PA46LiI sample indicates that lithium ions are highly mobile. Moreover, in comparison with the ⁷Li MAS signal of the lithium iodide salt, the chemical shift of the lithium ions in the PA46LiI sample is significantly higher. A higher chemical shift accounts for less shielding of the nucleus and stresses the dissociated state of the lithium ion. The other electron donors present, that is the carbonyl moiety in the amide bonds or water molecules, cannot offer as much electrons as iodide ions. As a result, less shielding of the Li nuclei leads to an increase in the chemical shift.

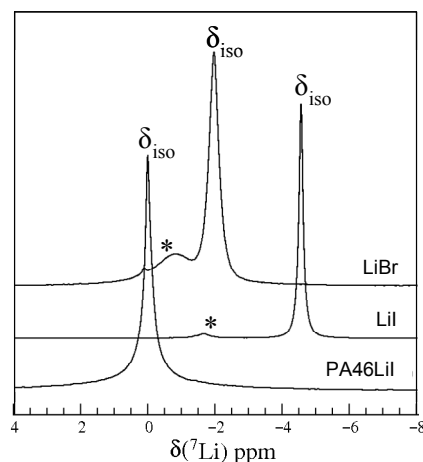


Figure 6.4: Solid state ${}^7\text{Li}$ MAS spectra of lithium bromide, lithium iodide and the PA46LiI sample as extruded, revealing clear changes in the chemical environment. Since the electron cloud of iodine is more populated compared to the electron cloud of bromide, the lithium nuclei in the LiI salt is more effectively shielded. The asterisks most likely arise due to hydration products.

Figure 6.5 addresses the storage (a) and loss modulus (b) as a function of temperature for the semicrystalline PA46 and the PA46LiI (from solution) samples. It is evident that below the glass transition temperature, which for both samples is in the proximity of 20°C , the storage modulus of the PA46LiI sample is higher than the storage modulus for the semicrystalline PA46 sample, 4.3 and 2.5 GPa respectively. The difference in storage modulus suggests different characteristic ratios (chain stiffness) for the two samples. The high storage modulus for PA46LiI suggests higher chain stiffness due to the interaction of ions with the polyamide molecules^{23,37}, supporting the conclusions of chapter 5. Due to the presence of crystals in the semi-crystalline PA46sc sample some stiffness is retained above the glass transition temperature, featuring a storage modulus of 0.66 GPa. Whereas, the storage modulus of the PA46LiI sample reaches the rubber plateau (0.20 GPa) and upon further heating the material flows at 106°C . These results conclusively demonstrate that the presence of lithium and iodide ions suppresses crystallization of polyamide 46.

Drawability of the semicrystalline and amorphous PA46 samples was monitored under tensile deformation. Figure 6.6a shows the engineering stress-strain curves of the two successive tensile deformations. The very first striking difference in the initial tensile experiments between the PA46sc and PA46LiI sample is the yield stress, being 58 and 20 MPa respectively. The low yield stress of the PA46LiI sample arises due to the absence of crystalline domains that are known to contribute more to the yield stress than the amorphous component³⁸. The elasticity modulus E is 1.3 and 0.45 GPa for the

semicrystalline and amorphous PA46 respectively. At large strain deformation strain hardening is observed in both samples. Since polyamides are generally of relatively low molecular weight, reducing the number of entanglements, strain hardening cannot be explained by trapped chain entanglements acting as physical constrains/cross-links³⁹. Instead, strain induced crystallization, as depicted for the PA46sc samples by the DSC thermograms in figure 6.3 and whitening of the initially transparent PA46LiI sample, is likely to result in tie molecules bridging the crystallites that effectively contribute to the network. It can be stated that tensile deformation of the amorphous PA46LiI sample requires less stress compared to the semicrystalline PA46sc sample.

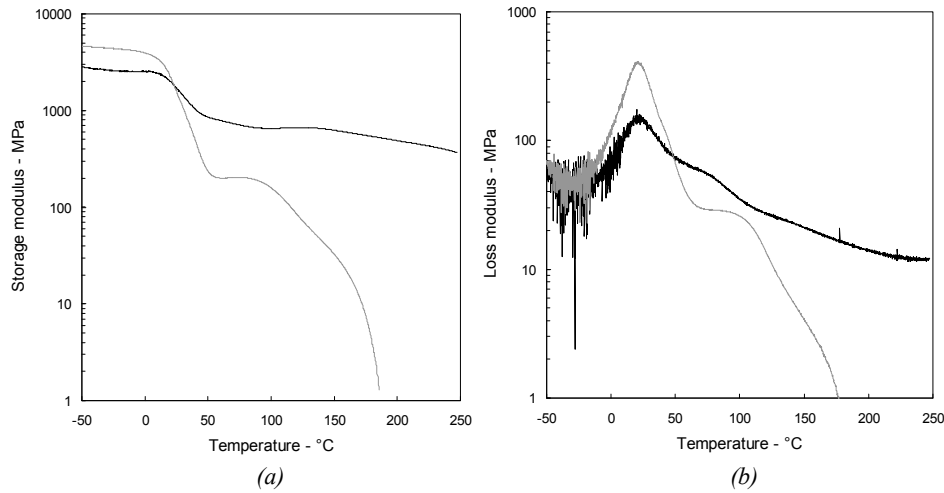


Figure 6.5: Storage modulus (a) and loss modulus (b) as function of temperature for semicrystalline PA46sc (black) and amorphous PA46LiI samples (grey).

In the second tensile experiment performed on the samples drawn in the first tensile experiment, the effect of strain induced crystallization is clearly demonstrated. Not only does the elastic modulus of the PA46sc and PA46LiI samples increase significantly, 2.6 and 1.1 GPa respectively, but also the yield stress increases from 112 and 84.8 MPa to 445 and 333 MPa respectively.

The influence of deformation rate on the engineering stress-strain curves of the amorphous polyamide samples is shown in Figure 6.6b. Upon increasing deformation rates the yield stress of the PA46LiI samples decreases significantly. Since the yield stress is governed by the crystalline fractions, fast deformation appears to result in suppression of the strain induced crystallization. The sample drawn at 20 mm/min, shows the highest yield stress suggesting the highest crystallinity in the investigated samples, hardly shows strain softening and the progression of crystallization is depicted by strain hardening at relatively

small strain deformation. Fast drawing, especially at 160 and 240 mm/min, results in a relatively low yield stress, where suppression of crystallization induces more strain softening. In fact, the respective samples neck considerably until strain hardening occurs at larger deformation rates. At high deformation rates however, strain induced crystallization is postponed. It has to be noted that the highly oriented WAXD patterns show no significant changes of the evolving crystallites upon different deformation rates, Figure 6.7. A detailed assignment of the diffraction signals will be discussed in the following paragraph, addressing the structural development upon drawing in different environments.

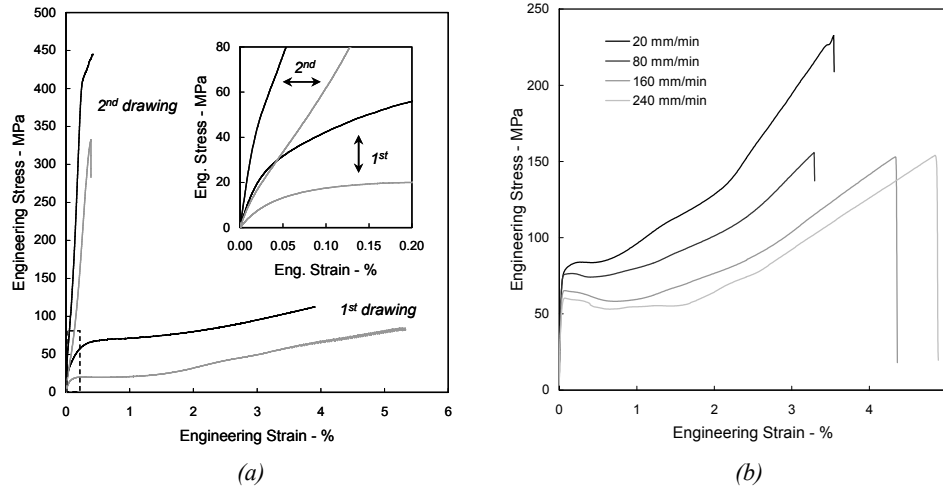


Figure 6.6: Stress-strain curves of the semicrystalline PA46sc (black) and amorphous PA46LiI (grey) samples in two successive tensile tests, Figure 6.6a. Figure 6.6b shows the influence of deformation rate on the stress-strain diagrams.

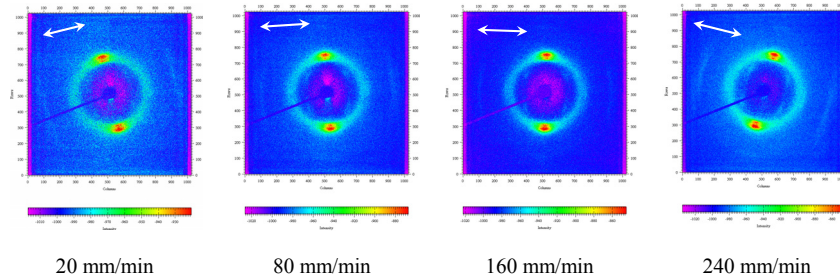


Figure 6.7: Typical fiber-like wide angle X-ray diffraction patterns of the initially amorphous PA46LiI samples after different deformation rates. The arrows indicate the deformation direction of the samples (and the meridian). The intense diffractions spots on the equator (perpendicular to the meridian) represent the interchain/intrasheet (inner) and intersheet (outer) distances. The Miller indices of the interchain/intrasheet and intersheet spacings are (200) and (020) respectively.

6.3.3 Structural development on drawing: do the ions migrate?

Among selective absorption of shielding agents and ineffective drawing due to chain slippage, inefficient removal of shielding agents played a key role in the failure of reversible plasticization techniques in the past¹⁶⁻²³. Immersion of dilute polyamide LiI solutions, which are characterized by shielding of the amide-amide hydrogen bonding, in excess of water entails instantaneous crystallization with re-establishment of interchain hydrogen bonding and without influencing the high melting temperature of polyamides, Chapter 5. Following these thoughts, strain induced crystallization and simultaneous migration of the ions from the polyamide samples, promoting hydrogen bonding, may lead to extended chain polyamide crystals. Figure 6.8a shows the influence of drawing temperature T_d on the thermal behavior of the initially amorphous PA46LiI samples drawn in air. Besides the slight, though subtle changes in the glass transition temperature, endothermic events of large enthalpic values are observed between 75 and 175°C. This specific endothermic event goes along with the evaporation of water as depicted by thermogravimetric analyses. Since the large enthalpic value cannot be attributed to the evaporation of water only, it is likely that the evaporation of “bound” water results in the re-association of ions, which in the case of lithium and iodide requires evolution of heat. With an increase in the drawing temperature the heat of fusion, directly reflecting the crystallinity after drawing (Table 6.1), increases from 17.6 to 21.1 J/g.

Drawing of the PA46LiI samples at 5, 55 and 95°C in water results in similar trends, Figure 6.8(b). However, though the glass transition temperature decreases upon increasing drawing temperatures, the values are significantly lower than in the samples drawn in air. Both the melting temperature and the corresponding heat of fusion increases with increasing drawing temperature. Whereas the melting temperature in the air drawn samples does not change with variations in the drawing temperature, the melting temperature of the water drawn samples increases to significantly higher values. Thus drawing in water induces higher crystallinity that is promoted at higher temperatures. This is likely to arise in the diffusion of ions out of the samples. The fact that the melting temperature and the respective enthalpies are considerably lower than the maximum enthalpy observed in the semicrystalline PAsc samples, as revealed in Figure 6.3, suggests that the presence of ions prevails. Due to increased molecular mobility, both in the polymeric as aqueous phase, increased temperatures promote the removal of the shielding agents.

The hypothesis that not all ions have been removed efficiently upon drawing in water is strengthened by the second heating ramp in DSC (Figure 6.8c,d). Whereas the thermal characteristics hardly vary in the semicrystalline air drawn samples, the variations in the melting temperature of the water drawn samples prevail even after melt crystallization. These findings indicate that the presence of ions, which is less after drawing in water on increasing temperature, suppresses the melting temperature of polyamides.

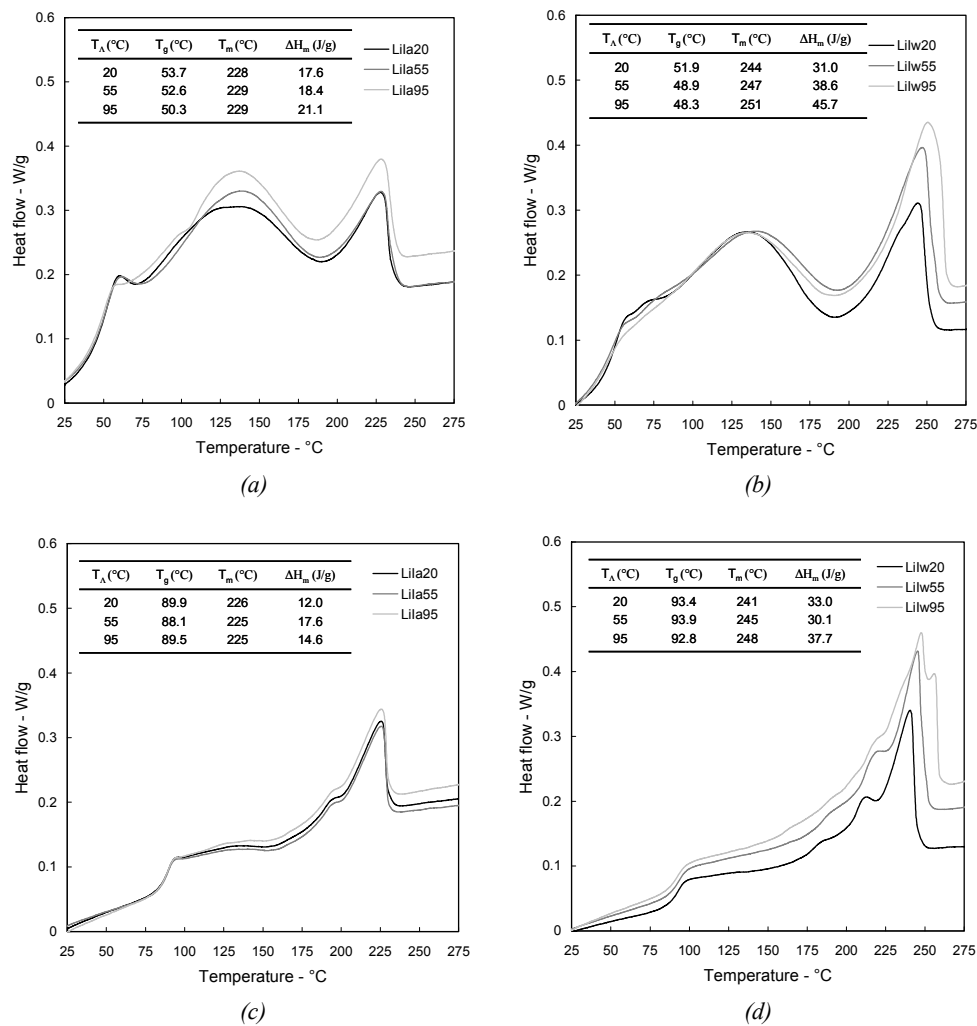


Figure 6.8: DSC thermograms of drawn PA46LiI samples in air (Lila, left) and water (Lilw, right) at 20, 55 and 95°C during the first (a), (b), and second (c) and (d) heating ramp. The grey scale of the curves is related to the drawing temperature as indicated in the figures. The inlays list the thermal characteristics, where T_A is the drawing temperature, T_g the glass transition temperature, T_m the melting temperature and ΔH_m the heat of fusion.

Moreover, both the air and water drawn samples show a distinct increase in the glass transition temperature of approximately 40°C after melting. The glass transition temperature of pure PA46 is around 75°C⁴¹. However, plasticizers such as water and ammonia are known to reduce the glass transition temperature and water potentially assisted by ions, are responsible for the reported T_g close to 20°C of the as extruded

samples by DMTA (Figure 6.5). Richardson and Ward however showed that extrusion of polyamide 6 with 2% LiCl, both extensively dried under vacuum, results in a shift of the glass transition from 89 to 110°C. The authors ascribed the increase to strong polymer-ion interaction. A six member ring coordination model was hypothesized by Wu et al.⁴². Such a complex formation may arise due to the evaporation of water on heating in DSC, supporting the re-association of ions causing the increase in glass transition temperature.

Two important questions need to be answered: (1) To what extent does hydrogen bonding establish itself during strain induced crystallization? (2) How does orientation evolve on drawing in air and water at different temperatures? Hydrogen bonding as well as chain orientation is essential for effective resistance of covalent bonds upon deformation parallel to the chain axis. Polarized FTIR spectroscopy has proven to be a powerful technique in addressing both issues. In Table 6.1 the aforementioned melting characteristics are combined with the Herman's orientation factor and the wavelength of the amide II vibration band. The amide II band, which comprises the C-N stretch band and the C-N-H bending in plane vibration, is sensitive for changes in the hydrogen bonding environment³¹. The more efficient the amide hydrogen bonding, the lower is the wavenumber. Amide moieties in amorphous phase polyamides generally occur above a wavenumber of 1450 cm⁻¹. Hence, the amide II wavenumbers presented in Table 6.1 are all of crystalline nature, suggesting that during strain induced crystallization the ions are secreted from the lattice. As a result the amorphous becomes more plasticized, explaining the decrease in T_g upon increasing crystallinity, see Figure 6.8a for example. Since the ions remain present in the air drawn PA46LiI samples, the amide hydrogen bonding is less efficient than in the water drawn samples where the ions are partially removed. The sample drawn in water at 55°C shows the lowest wavenumber suggesting the formation of most efficient hydrogen bonds.

Table 6.1: The effect of drawing conditions on hydrogen bonding, orientation and melting characteristics

drawing environment		H-bonding	orientation	melting characteristics		
medium	temperature	amide II	f	T _m ^{a)}	ΔH _m ^{a)}	X _c ^{a)}
-	°C	-	-	°C	J/g	%
air	20	1544.3	0.97	228	17.6	8.40
air	55	1544.5	0.80	229	18.4	8.78
air	95	1543.7	0.90	229	21.1	10.1
H ₂ O	20	1543.7	0.94	244	31.0	14.8
H ₂ O	55	1542.0	0.98	247	38.6	18.4
H ₂ O	95	1542.7	0.93	251	45.7	21.8
H ₂ O	55/5	1542.1	0.99	270	63.5	30.2
H ₂ O	95/5	1542.4	0.91	269	63.0	30.0

^{a)} Where T_m is the melting temperature, ΔH_m the heat of fusion and X_c the crystallinity.

The Herman's orientation generally increases in analogy to the decrease in the amide II wavenumber and the increase in crystallinity. However, two exceptions have to be made. The first is at 20°C in the absence of additional water, acting as a plasticizer (the air drawn sample). Deformation of the sample close to the glass transition temperature (Figure 6.5) reduces chain relaxation in the amorphous state, preserving the relatively high orientation factor. The second scenario is encountered if the drawing temperature is 95°C. Here, thermal motion promotes relaxation of the amorphous chains, diminishing the orientation factor. To minimize the influence of relaxation upon drawing at 55 and 95°C, water drawn PA46LiI samples after maximum deformation were successively quenched under constant stress in cold water (~5°C). Though chain relaxation could not be suppressed in case of the 95°C water drawn samples, depicted by an orientation factor f of 0.91, quenching of the 55°C water drawn samples renders an ideal set of properties. The highest hydrogen bonding efficiency with the highest percentage of crystals, which are very well oriented.

Next to high hydrogen bonding efficiency and high orientation, crystal perfection in terms of well-alignment, stability and dense chain packing is crucial as well in realizing ultimate properties in fibers⁴⁰. Figure 6.10 shows the wide angle diffraction patterns of both the semicrystalline PA46sc and initially amorphous PA46LiI samples drawn in air as well as water at 20, 55 and 95°C. Also the water drawn PA46LiI samples that were quenched in cold water are incorporated. Based on an extensive crystallographic study by Atkins et al.⁴⁰, the diffraction signals were assigned in the right bottom picture. To assist the discussion on crystal perfection, table 6.2 lists the prominent signals.

The orientation or alignment of chains can be assessed by the azimuthal distribution of the equatorial diffraction signals in the WAXD patterns, in particular using the 200 and the 020 diffraction signals. These signals correspond to the interchain/intrasheet and intersheet spacings respectively. Figure 6.9 shows the monoclinic unit cell of polyamide 46 single crystals. The chain orientation in the PA46LiI samples follows the trends of the Herman's orientation factor. Broad 200 and 002 arcs on the equator reveal less orientation in the semicrystalline PA46 samples upon drawing. Moreover, the 20 and 95°C air drawn and the 20°C water drawn PA46sc samples, reveal superimposed interchain and intersheet diffraction signals on the equator (Table 6.2). The unresolved 200 and 020 diffraction signals indicate that the hydrogen bonded planes are poorly organized, though aligned. With an increasing drawing temperature of the semicrystalline samples, and in particular followed by cooling, the interchain distance tends to increase while the intersheet distance decreases, approaching but not reaching single crystal spacings reported by Atkins et al.⁴⁰. If ions prevail after strain induced crystallization, for example by drawing in air, only small changes in the interchain and intersheet spacings are observed as function of drawing temperature. With removal of ions, by drawing in water and preferably followed by quenching in cold water, the interchain and intersheet distances adopt the single crystal spacings⁴⁰. This trend is analogous to cooling polyamides below the Brill transition

temperature, where reduced molecular motion and restitution of crystalline hydrogen bonding induces an increase in the interchain distance and a decrease in the intersheet distance⁴⁴. Hence, the presence of ions in the lattice, at the crystal surface or both, weakens the crystalline hydrogen bonding as earlier suggested in the discussion on the amide II band. Furthermore, the amorphous halo in the PA46LiI samples shifts to higher values and tends to vanish with increased ion removal and increased crystallinity.

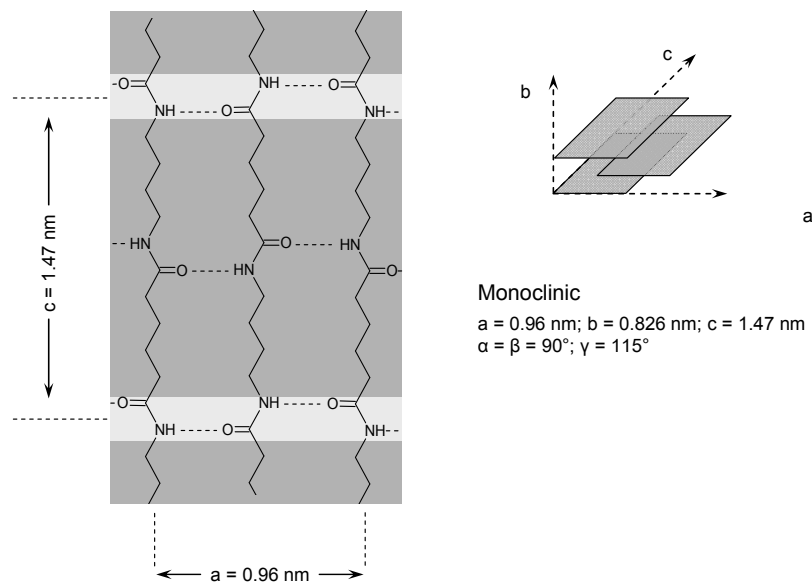


Figure 6.9: The monoclinic unit cell of polyamide 46 single crystals with $a = 0.96 \text{ nm}$, $b = 0.826 \text{ nm}$; $c = 1.47 \text{ nm}$ and $\gamma = 115^\circ$. It has to be noted that the true unit cell contains four chain segments and that the a and b values are hence doubled⁴⁰.

The best resolved diffraction patterns, reflecting high crystal perfection, with well defined hydrogen bonded planes were observed for the water drawn PA46 LiI samples at 55 and 95°C that were successively quenched in cold water. The semicrystalline nature of the PA46sc samples prior to drawing, introduces crystallites that acts as physical crosslinks, is likely to hinder ideal structure development.

Since crystal perfection, which evolves during strain induced crystallization of the PA46LiI samples, promotes the ultimate performance, the mechanical properties of the air and water drawn PA46LiI and PA46sc filaments was tested in terms of tenacity at break, elongation at break and the tensile modulus ($< 0.4\%$ elongation). The results of tensile testing are listed in Table 6.3. Due to large deviations, which are likely to arise in practically inconsistency drawing, no conclusive remarks can be made on the influence of

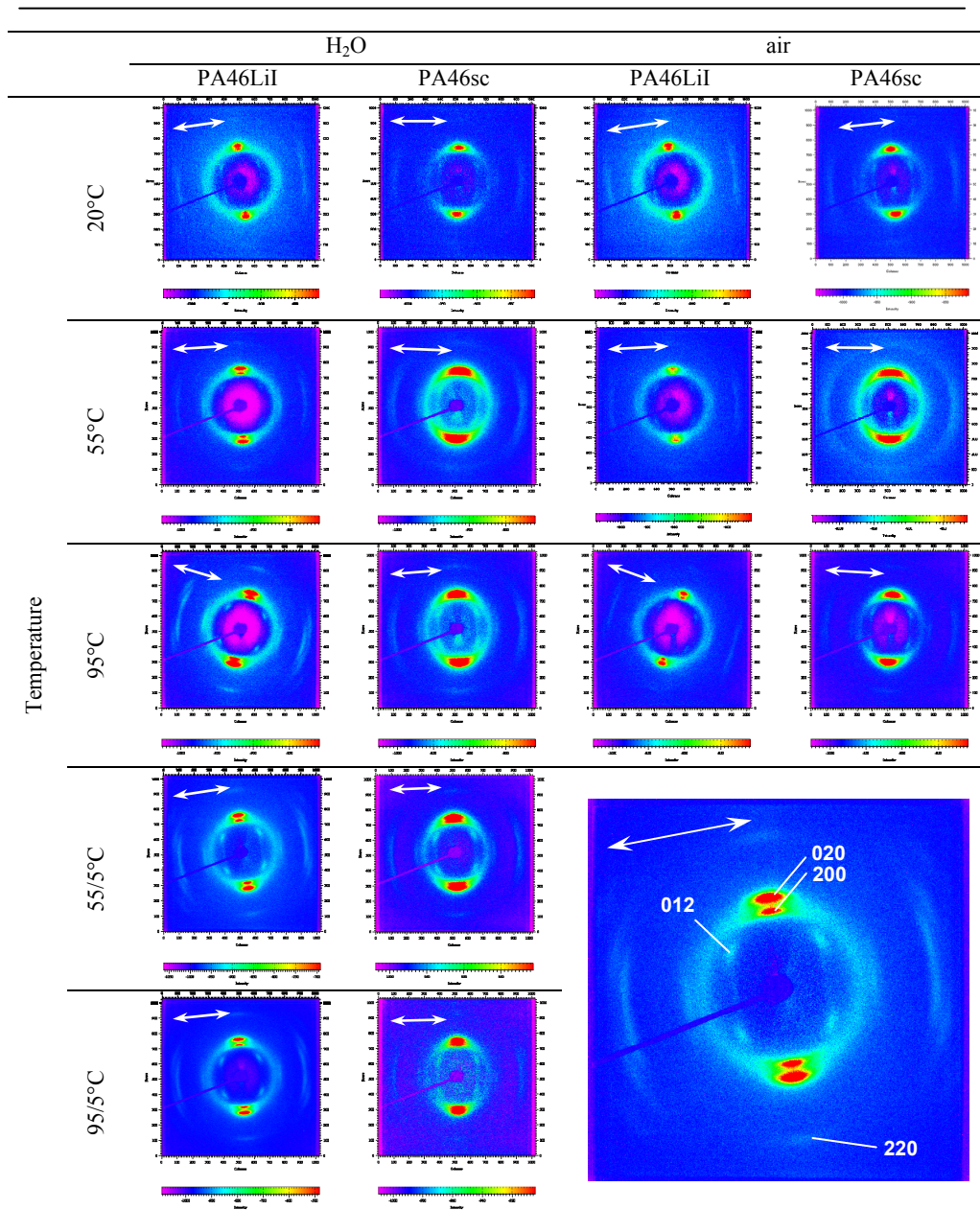


Figure 6.10: Structure development upon drawing the semicrystalline PA46sc and amorphous PA46LiI samples in water and air at 20, 55 and 95°C. To evaluate the influence of chain relaxation after deformation at 55 and 95°C, the PA46sc and PA46LiI samples were after maximum deformation in water quenched in water of 20°C. Based on the work of Atkins et al. the diffraction signals are assigned in the right bottom corner⁴⁰. The arrows indicate the fiber/drawing direction.

Table 6.2 The effect of the drawing conditions on the equatorial interchain, 200, and intersheet, 020, diffraction signals and the d-value of the amorphous halo in nm.

drawing environment		PA46 LiI			PA46sc		
medium	temperature	200	020	halo	200	020	halo
air	20°C	0.427	0.381	0.399	0.413 ^{a)}	0.413 ^{a)}	0.433
air	55°C	0.426	0.381	0.400	0.422	0.390	0.432
air	95°C	0.428	0.380	0.400	0.411 ^{a)}	0.411 ^{a)}	0.438
H ₂ O	20°C	0.426	0.384	0.400	0.413 ^{a)}	0.413 ^{a)}	0.433
H ₂ O	55°C	0.431	0.375	0.399	0.426	0.386	0.435
H ₂ O	95°C	0.435	0.375	0.404	0.421	0.392	0.437
H ₂ O	55/5°C	0.436	0.374	0.410	0.430	0.383	0.435
H ₂ O	95/5°C	0.436	0.373	0.417	0.426	0.386	0.440

^{a)} Here the interchain and intersheet diffraction signals are not well resolved, resulting in a single peak.

Table 6.3: Mechanical performance of semicrystalline PA46sc and initially amorphous PA46LiI

drawing environment		tenacity at break		elongation at break		tensile modulus	
medium	temperature	av.	sd.	av.	sd.	av.	sd.
PA46sc	°C	MPa	MPa	%	%	GPa	GPa
air	20	422	49	19.7	2.9	8.0	1.7
air	55	277	36	33.0	18.7	6.1	1.3
air	95	416	131	17.9	2.1	7.5	1.8
H ₂ O	20	277	112	60.4	15.4	5.5	0.6
H ₂ O	55	356	44	28.6	4.9	2.1	0.0
H ₂ O	95	427	120	25.8	1.1	2.4	0.7
H ₂ O	55/5	446	35	35.9	4.0	2.7	0.2
H ₂ O	95/5	436	45	28.2	5.8	2.6	0.3
PA46LiI	°C	MPa	MPa	%	%	GPa	GPa
air	20	423	76	28.0	9.0	7.1	1.3
air	55	432	36	30.7	4.2	6.8	0.9
air	95	455	69	21.9	3.7	8.2	0.5
H ₂ O	20	404	36	41.9	5.3	9.2	1.7
H ₂ O	55	483	59	42.6	1.9	7.2	1.3
H ₂ O	95	328	41	43.7	4.4	7.9	1.2
H ₂ O	55/5	360	159	30.2	11.7	8.3	0.2
H ₂ O	95/5	380	63	38.8	4.9	7.4	1.7

Where av. and sd. represent average values and standard deviations respectively.

drawing medium and drawing temperature on the mechanical properties of the samples. The discussion is hence limited to stating that for the semicrystalline PA46sc samples the tenacity at break ranges from 277 to 446 MPa, the elongation at break from 18 to 60% and the tensile modulus from 2 to 8 GPa, whereas the initially amorphous PA46LiI samples feature tenacities at break between 328 to 483 MPa, elongations at break between 22 and

44% and tensile moduli between 7 to 9 GPa. Incomplete drawing, promoted by inefficient removal of ions in LiI samples, is a possible cause for the relatively high elongation at break.

6.3.4 Structure development on complete removal of ions in superheated water

Incomplete removal of shielding components, comprising lithium and iodide ions in the present chapter, has been reported to be one of the main reasons for failure in the concept of temporary plasticization⁴³. Besides the disappointing mechanical performance, strain induced crystallization in water results only in partial removal of the ions, hindering the formation of highly crystalline polyamides with consequential high melting temperature. However, high Herman's orientation factors, up to 0.99, and crystal perfection, where the spacings are in agreement with single crystal values⁴⁰, triggered the need for a better understanding on the diffusion of the ions in excess of water. Since the residence time of the samples during the drawing process in water was relatively short, the removal of ions was investigated by exposing the 55°C water drawn PA46LiI samples to superheated water at 150°C for 5, 10 and 15 minutes. WAXD patterns and DSC curves before and after the superheated water treatment are compared below. Furthermore, structural changes were followed in-situ by time-resolved WAXD experiments, though at considerably lower heating and cooling rates.

Figure 6.11 reveals the crystallographic changes between the PA46LiI and PA46sc samples before and after immersion in the superheated state of water. In the previous paragraph, the isotropic ring in the PA46LiI sample was tentatively assigned to scattering of as well the amorphous phase as the iodide ions. Besides, the presence of ions suppresses crystallization and as a result promotes amorphous scattering. For both samples the amorphous halo vanishes after the superheated water treatment and suggests increasing crystallinities and in the case of the PA46LiI sample efficient ion removal. However, the two samples behave different. With the increase in crystallinity the crystal structure of the semicrystalline PA46sc sample, which was initially poorly resolved (Table 6.4), perfects as well. Although the interchain and intersheet spacings nearly adopt the single crystal values, broadening of the respective arcs in azimuthal direction suggests a reorganization process similar to annealing and moreover a decrease in orientation. In contradiction, both crystal perfection and orientation of the PA46LiI samples upon superheated water treatment prevails and only minor changes in the 200 and 020 spacing are observed. Following the amorphous scattering upon heating to the superheated state of water reveal a gradual decrease in the scattered intensity well below 100°C, indicating that the diffusion of ions is not primarily temperature but time dependent.

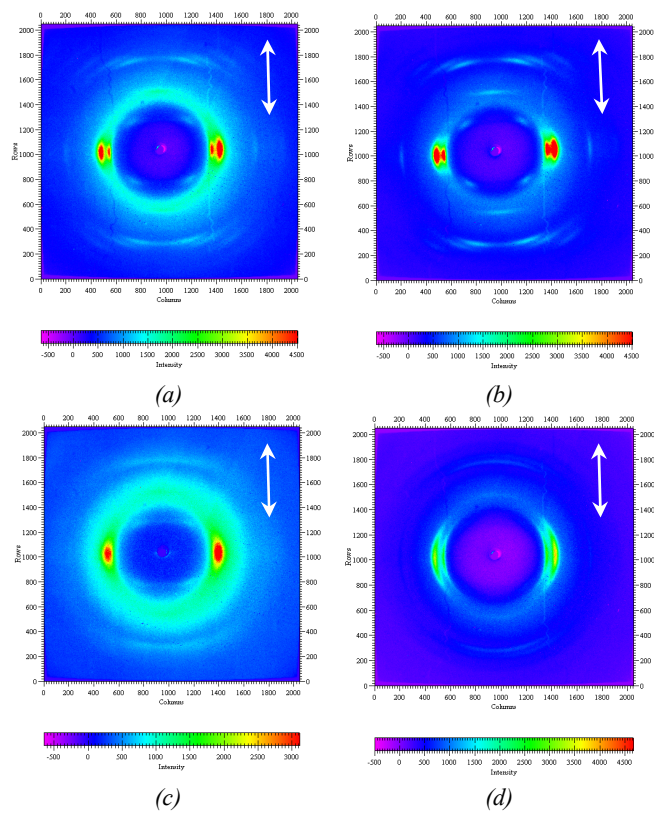


Figure 6.11: Wide angle X-ray diffraction patterns of water drawn PA46LiI and PA46sc (55°C) recorded before, (a) and (c) respectively, and after a 5 minutes' immersion in superheated water at 150°C, (b) and (d) respectively. The arrows indicate the sample drawing direction.

Table 6.4: Influence of superheated water on specific diffraction signals

index	PA46LiI spacings (nm)		PA46sc spacings (nm)	
	before	after	before	after
200	0.431	0.430	0.419 ^{a)}	0.434
020	0.374	0.376	0.404 ^{a)}	0.374

^{a)} Values derived from unresolved diffraction signals, resulting in a single asymmetric peak.

Since the wide angle X-ray diffraction study above suggests efficient ion migration and increased crystallinities, the melting characteristics are followed by DSC, Figure 6.12. Irrespective of time, immersion of the 55°C water drawn PA46LiI sample ($T_m = 229^\circ\text{C}$; $X_c = 8.8\%$) induces melting temperatures of 289°C and crystallinities of 53%. The heat of

fusion is 111 J/g, which is more than the reported values for solution grown crystals²⁸. The WAXD and DSC conclusively demonstrate that highly efficient removal of ions is feasible and time dependent, preserving high orientation, crystal perfection and high crystallinity.

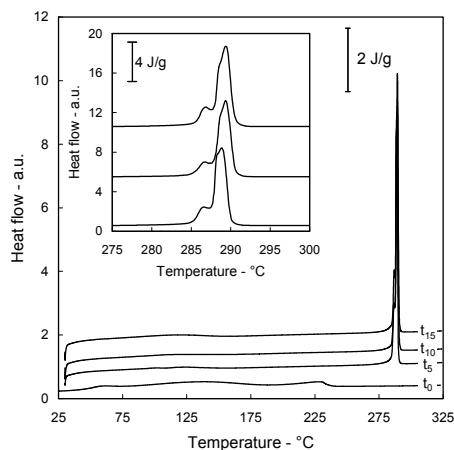


Figure 6.12: DSC thermograms depicting the changes in melting characteristics after immersion of the 55°C air drawn PA46LiI sample (t_0) in the superheated state of water at 150°C for 5, 10 and 15 minutes. The inset is a magnification of the melting peaks after immersion in superheated water.

6.4 Conclusions and recommendations

6.4.1 Conclusions

The cooperative energy of hydrogen bonds residing between crystalline lamellar stems is the elementary reason for the failure of polyamides as high strength and high modulus materials. This class of materials relies on the high distortion resistance of covalent bonds in perfectly oriented extended polymer molecules, assembled in extended chain crystals. Reversible shielding of the amide moieties by temporary dissolution in aqueous LiI solutions may entail ideal chain alignment and extended chain crystals strengthened by intermolecular hydrogen bonding after efficient removal of the ions. Extrusion of PA46 from superheated water in the presence of LiI results in amorphous PA46 samples, where a high ⁷Li MAS signal in NMR stresses the solution characteristics of the samples. Tensile deformation of the amorphous PA46, having a glass transition temperature around 20°C, shows a low yield stress due to the absence of crystals. At large strain deformation orientation induced crystallization caused by strain hardening. With increasing deformation rate, strain induced crystallization is postponed and more chain alignment may be realized upon drawing.

Inefficient deshielding by means of ion diffusion in water upon drawing, results in suppression of the crystallinity and melting temperature. Strain induced crystallization at temperatures above the glass transition temperature, preferably at 55°C followed by quenching in cold water, yields restoration of efficient repetitive interchain/intrasheet amide-amide hydrogen bonding, high Herman's orientation factors (up to 0.99), though the crystallinity and melting temperature are considerably lower than the conventional melt processed values. Strain induced crystallization under these specified conditions, entails crystal perfection where the spacings are in agreement with single crystal values. Adequate removal of ions is feasible by immersion of the drawn samples in water at elevated temperature (and pressure), preserving the high orientation, crystal perfection and the restoration of high crystallinity and consequential high melting temperature. However, from the studies reported in this thesis one cannot conclude to what extent the chains are extended in the crystals.

6.4.2 Recommendations

Strain induced crystallization in aqueous PA46LiI samples shows ideal structure development that can be maintained by sufficient diffusion of ions that above T_g is primarily time dependent. Hence, reduced sample diameters, for example obtained in yarns, shorten the diffusion path of ions. Efficient removal of the shielding ions in combination with adequate chain overlap for strong secondary interactions is likely to enhance the strength and modulus of polyamides. Nevertheless, the role of molar mass should be investigated as well. Though the amide-amide hydrogen bonding enables the use of relatively low molecular weight polymers (compared to UHMWPE), the influence of an increased amount of chain ends on for example crystal modulus is yet unknown. Instant drawing, i.e. directly after extrusion, besides suppresses ageing, which induces stronger secondary interactions and limits the draw ratio as well. High draw ratios, avoiding chain slip, prior to strain induced crystallization are desired for adequate chain alignment and minimizing defects in extended chain crystals. Small angle X-ray scattering showed no lamellar spacing, suggesting the absence of a well defined distribution of lamellar spacings. The main question yet to be answered is to which extent the chains in the crystalline domains are in extended chain conformation.

Ideal experimental conditions with respect to fiber diameter and spinning/drawing parameters, facilitating adequate ion removal and chain alignment, are of technological nature and require optimization in an industrial environment, hopefully contributing to the development of a new generation of (super)strong polyamide fibers.

6.5 References

1. Afshari, M.; Sikkema, D.J.; Lee, K.; Bogle, M. *Pol. Rev.* **2008**, 48, 230-274.
2. Treloar, L. R. G. *Polymer* **1960**, 1, 95-103.
3. Termonia, Y.; Meaking, P.; Smith, P. *Macromolecules* **1985**, 18, 2246-2252.
4. Kotek, R. *Polym. Rev.* **2008**, 48, 221-229.
5. Schalley, C.A. in *Analytical Methods in Supramolecular Chemistry*, Wiley-VCH Verlag GmbH&Co. KGaA, Weinheim **2007**.
6. Nakamae, K.; Nishino, T. *Polym. News.* **1989**, 14, 179-181.
7. Keller, A. In *Growth and Perfection of Crystals*, John Wiley and Sons Inc., New York, **1948**, 499-528.
8. Abo el Maaty, M. I.; Hosier, I. L.; Bassett, D. C. *Macromolecules* **1998**, 31, 153-157.
9. Mandelkern, L. In *Crystallization of Polymers, 2nd edition, vol.2 Kinetics and Mechanisms*, Cambridge University Press **2004**.
10. Wittmann, J. C. ; Lotz, B. *J. Polym. Sci. Polym. Phys. Edn.* **1985**, 23, 205-226.
11. Keller, A.; Pedemonte, E. *J. Cryst. Growth* **1973**, 18, 111.
12. Rastogi, S.; Lippits, D.R.; Peters, G.W.M.; Graf, R.; Yao, Y.; Spiess, H.W.; *Nature Mat.* **2005**, 4, 635-641.
13. Rastogi, S.; Kurelec, L.; Cuijpers, J.; Lippits, D.; Wimmer, M.; Lemstra, P.J. *Macromol. Mater. Eng.* **2003**, 288, 964-970.
14. Lemstra, P.J.; Kirschbaum, R.; Ohta, T.; Yasuda, H. In *Developments in Oriented Polymers 2*, Elsevier Science Ltd, Kidlington, Oxfordshire **1987**.
15. Postema, A. R.; Smith, P.; English A. D. *Polym. Comm.* **1990**, 31, 444-447.
16. Zachariades, A. E.; Porter R. S. *J. Appl. Pol. Sci.* **1979**, 24, 1371-1382.
17. Kanamoto, T.; Zachariades, A. E.; Porter, R. S. *J. Appl. Polym. Sci. Polym. Phys. Edn.* **1982**, 20, 1485-1496.
18. Chuah, H. H.; Porter, R. S. *Polymer* **1986**, 27, 1022-1029.
19. Lee, Y. H.; Porter, R. S. *J. Macromol., Sci., Phys. B* **1995**, 34, 295-309.
20. Acierno, D.; Bianchi, E.; Ciferri, A.; Cindio, B.; Migliaresi, C.; Nicolais, L. *J. Polym. Sci. Polym. Symp.* **1976**, 54, 259-269.
21. Acierno, D.; Lamantia, F. P.; Polizzotti, G.; Ciferri, A. *J. Polym. Sci. Polym. Phys. Edn.* **1979**, 17, 1903-1912.
22. Ciferri, A.; Acierno, D.; Alfonso, G. C. *Patent US4167619* **1979**.
23. Richardson, A.; Ward, I. M. *J. Polym. Sci., Polym., Phys. Edn.* **1981**, 19, 1549-1565.
24. Vasanthan, N.; Kotek, R.; Jung, D. W.; Shin, D.; Tonelli, A. E.; Salem, D. R. *Polymer* **2004**, 45, 4077-4085.
25. Jung, D.; Kotek, R.; Vasanthan, N.; Tonelli, A.E.; *Abstracts of Papers 228th ACS national Meeting, August* **2004**, 22-26.
26. Gupta, A.; Saquing, C.D.; Afshari, M.; Tonelli, A.E.; Khan, S.A.; Kotek, R. *Macromolecules* **2009**, in print.

-
27. Rastogi, S.; Terry, A. E.; Vinken, E. *Macromolecules* **2004**, *37*, 8825-8828.
 28. Vinken, E.; Terry, A. E.; Van Asselen, O.; Spoelstra A. B.; Graf, R.; Rastogi, S. *Langmuir* **2008**, *24*, 6313-6326.
 29. Wong Po Foo, C.; Bini, E.; Hensman, J.; Knight, D. P.; Lewis, R. V.; Kaplan, D. L. *Appl. Phys. A* **2006**, *82*, 223-233.
 30. Harings, J. A. W.; Van Asselen, O.; Graf, R.; Broos, R.; Rastogi, S. *Cryst. Growth Des.* **2008**, *8*, 2469-2477.
 31. Harings, J. A. W.; Van Asselen, O.; Graf, R.; Broos, R.; Rastogi, S. *Cryst. Growth Des.* **2008**, *8*, 3323-3334.
 32. Hess, B.; Harings, J. A. W.; Rastogi, S.; Van der Vegt, N. F. A. *J. Phys. Chem. B.* **2009**, *113*, 627-631.
 33. Harings, J. A. W.; Yefeng, Y., Van Asselen, O.; Graf, R.; Broos, R.; Rastogi, S. *Langmuir* **2009**, submitted.
 34. Brandrup, J.; Immergut, E.H.; Grulke, E.A., *Polymer Handbook 4th ed.*, Wiley, New York **1999**.
 35. Cole K.C.; Depecker, C.; Jutigny, M.; Lefebvre, J.M.; Krawczak, P. *Pol. Eng. Sci.* **2004**, *44*, 231-240.
 36. Schreiber Lee, S.; Phillips, P.J. *Eur. Polym. J.* **2007**, *43*, 1933-1951.
 37. Ober, C.K. *Science* **288**, 448-449.
 38. Schrauwen, B.A.G.; Janssen, R.P.M.; Govaert, L.E.; Meijer, H.E.H. *Macromolecules* **2004**, *37*, 6069-6078.
 39. Persyn, O.; Miri, V.; Lefebvre, J.M.; Depecker, C.; Gors, C.; Stroeks, A. *Polym. Eng.Sci.* **2004**, *44*, 21-271.
 40. Atkins, E.D.T; Hill, M.; Hong, S.K.; Keller, A.; Organ, S. *Macromolecules* **1992**, *25*, 917-924.
 41. Eersels, K.L.L.; Groeninckx, G. *Polymer* **1996**, *37*, 983-989.
 42. Wu, Y.; Xu, Y.; Wang, D.; Zhao, Y.; Weng, S.; Xu, D. *J. Appl. Polym. Sci.* **2004**, *91*, 2869-2875.
 43. Kotek, R.; Jung, D.; Tonelli, A.E.; Vansanathan, N. *J. Macromol. Sci. C., Poly. Reviews* **2005**, *45*, 201-230.
 44. Vinken, E.; Terry, A.E.; Hoffmann, S.; Vanhaecht, B.; Koning, C.E.; Rastogi, S. *Macromolecules* **2006**, *39*, 2546-2552.



Samenvatting

Polymeren zijn lange keten moleculen, opgebouwd uit repeterende eenheden, de zogenaamde monomeren, die chemisch aan elkaar zijn geschakeld via covalente bindingen, bijv. de C-C binding in polyethyleen. We maken onderscheid tussen biopolymeren die in de natuur worden gemaakt en synthetische polymeren die door de chemische industrie worden geproduceerd (plastics).

De eigenschappen van polymere materialen worden niet alleen bepaald door de primaire chemische structuur, de chemische opbouw van het polymeer, maar ook door de interacties tussen ketens (intermoleculaire interacties) en de conformatie (ruimtelijke vorm). Met name bij biopolymeren is er vaak een uniek samenspel tussen de primaire chemische structuur, d.w.z. de ketenopbouw, en de intermoleculaire interacties met als bekend voorbeeld de dubbele helix bij DNA, de drager van de erfelijke eigenschappen. Een ander bekend voorbeeld is de eiwitten (proteïnen), die hun unieke conformaties ontleen aan het samenspel tussen de volgorde van monomere eenheden, de aminozuren, en secundaire interacties (bijv. waterstofbruggen) tussen de aminozuren in het molecuul, de vorming van de bekende α -helix structuur en β -sheets, en/of tussen moleculen onderling.

Synthetische polymeren zijn t.o.v. biopolymeren chemisch eenvoudiger met het voordeel dat ze daardoor thermisch stabiel zijn en in gesmolten toestand kunnen worden verwerkt via bijv. spuitgieten of extrusie tot eindproducten. Dit in tegenstelling tot biopolymeren zoals cellulose (hout) dat verspanend moet worden verwerkt. Ook bij synthetische polymeren spelen de conformatie en secundaire interacties tussen moleculen een grote rol. Een extreem voorbeeld in dit verband is het meest simpele polymeer op aarde: polyethyleen (PE). Op basis van polyethyleen worden op industriële schaal flexibele films en containers gemaakt, maar ook supersterke vezels met een specifieke sterkte en stijfheid groter dan staal. In deze supersterke vezels liggen de moleculen in gestrekte vorm naast elkaar in de vezelrichting. Tussen de apolaire PE moleculen zijn alleen zwakke van der Waals krachten aanwezig, maar bij voldoende lengte van de moleculen is de som van deze zwakke interacties tussen de moleculen dermate groot dat een dusdanige frictie wordt opgebouwd tussen de gestrekte moleculen bij belasting (in de vezelrichting) dat de covalente bindingen in de ketens worden belast, resulterend in hoge sterkte en stijfheid. In zekere zin kunnen deze supersterke PE vezels worden beschouwd als 1-dimensionaal diamant bij kortstondige en snelle belasting maar bij langdurige belasting treedt kruip op en een ander nadeel van deze PE vezels is de relatief lage smelt temperatuur van circa 150°C.

Een beter basismateriaal dan PE voor het maken van supersterke vezels met minder kruip en een hogere smelt temperatuur zouden de zogenaamde polyamiden (nylons) zijn. Polyamiden zijn de synthetische tegenhanger van eiwitten met de amide binding als schakel tussen de monomere eenheden. Proteïnen worden door polymeerchemici ook wel gedecoreerde nylons (Nylon 2) genoemd. In de industrie is veel onderzoek verricht om op

basis van polyamiden supersterke vezels te maken door het uitlijnen c.q. vertrekken van de ketens in de vezelrichting zoals bij PE, maar helaas zonder succes. Bij het verwerken van polyamiden via de smelt of oplossing treedt bij afkoelen kristallisatie op en worden gevouwen ketenkristallen gevormd, te vergelijken met de bekende β -sheets bij proteïnen. Deze gevouwen ketenkristallen laten zich niet ontvouwen bij verstrekken zoals bij polyethyleen vanwege de relatief sterke intermoleculaire waterstofbruggen.

Het doel van het proefschrift is om deze waterstofbruggen in polyamiden tijdelijk af te schermen tijdens het verwerken en verstrekkproces, en weer te activeren wanneer de vezel gereed is. De natuur is hierbij in zekere zin de inspiratiebron, namelijk het spinproces van zijde waarbij de spin in de klieren de waterstofbruggen van de proteïnen ook afschermt in een samenspel tussen water, zouten (ionen) en de pH.

Op basis van resultaten in een eerder proefschrift van Esther Vinken (TU/e, 2008) inzake het gebruik van oververhit water om nylons op te lossen, zijn laag moleculaire modelverbindingen, die naar verwachting de kristallijne segmenten van alifatische polyamiden vertegenwoordigen, bestudeerd in het oplosproces in, en kristallisatie vanuit de oververhitte toestand van water (hoofdstuk 2, 3 en 4). De modelverbindingen zijn zogenaamde bisamide-diolen, die worden gekenmerkt door twee centrale amide groepen en twee hydroxyl eindgroepen. Net als in polyamiden, kan de lengte van de alifatische segmenten, die de polaire groepen scheiden, gevarieerd worden.

Waterstofbruggen in het vlak van de amide groepen zijn kenmerkend voor alifatische polyamiden. Het blijkt dat een kort alifatisch segment tussen de amide groepen in combinatie met twee langere en identieke segmenten tussen de amide en hydroxyl groepen leidt tot een stapeling van kristalvlakken waarin de moleculen door amide-amide waterstofbruggen bij elkaar worden gehouden. In het geval van een evenredige segmentenverdeling tussen de polaire groepen in het molecuul, worden amide-hydroxyl waterstofbruggen tussen de structurele amide vlakken gevormd. In dit scenario is de rol als modelverbinding twijfelachtig. Desalniettemin worden de thermodynamische, structurele en conformationele eigenschappen, net als in alifatische polyamiden, beïnvloed door een balans in thermische mobiliteit en waterstofbruggen efficiëntie. Beide modelverbindingen zijn eveneens oplosbaar in oververhit water. Tijdens het kristallisatieproces bij afkoeling worden rotatiebeperkingen van de intrinsiek starre amide groepen opgeheven door interactie van water moleculen met de amide groepen. De extra vrijheidsgraad in het kristallisatieproces resulteert in ideale kristallijne waterstofbruggen. Bovendien bestaat de kans dat water moleculen tijdens kristallisatie opgesloten worden in het kristal.

In het tweede deel van het proefschrift worden water moleculen in combinatie met ionen gebruikt in het afschermen en dirigeren van waterstofbruggen in polyamiden. Gebruik werd gemaakt van de zogenaamde Hofmeister ionen. De Hofmeister reeks is een indeling die gebaseerd is op het al dan niet hydraterende karakter van ionen. Hydraterende ionen, bekend als kosmotropisch, stimuleren de organisatie van water moleculen, terwijl niet hydraterende ionen, of te wel chaotropisch, de water structuur verstoren.

Alifatische polyamiden kunnen bij temperaturen rond de Brill transitie opgelost worden in de oververhitte toestand van water. De Brill transitie in polyamiden is een omkeerbare kristaltransformatie, die beïnvloed wordt door alifatische ketenmobiliteit en waterstofbruggen efficiëntie. Bij een toename van de ionische sterkte van grote, niet hydraterende anionen, zoals bromide en jodide, worden de waterstofbruggen tussen water moleculen verstoord. De diffusieconstante van water en opgeloste componenten neemt toe, waardoor water moleculen en kleine hydraterende kationen bij een relatief lage temperatuur de gevouwen polyamide ketenkristallen indringen. Niet alleen wordt de oplossings-temperatuur verlaagd, maar ook de kristallisatietemperatuur bij afkoeling. Om het apolaire contactoppervlak met water te minimaliseren, worden niet hydraterende anionen door hydrofobe hydratatie naar de alifatische segmenten van de polyamide ketens gedreven. Daarnaast gaan sterk hydraterende kationen, bij voorkeur lithium ionen, interactie aan met de amide groepen waardoor een ladingsverdeling langs de polyamideketen ontstaat. Als gevolg wordt de kristallisatie na oplossing in oververhit water onderdrukt, zelfs bij kamertemperatuur. Verstrekken van de polyamide oplossing in overmaat water leidt tot de diffusie van ionen, het herstel van amide-amide waterstofbruggen en oriëntatie. Ondanks het feit dat verstrekbaarheid van de polyamide oplossing mogelijk is, gaat de sterkte echter verloren door vermoedelijk onvoldoende ketenoverlap tijdens kristallisatie, d.w.z. de spanning kan niet worden overgedragen tussen de ketens.

Om ketenoverlap tijdens kristallisatie te bevorderen is in hoofdstuk 6 het verwerken (extrusie) van een geconcentreerde polyamide oplossing onderzocht. In dit proces worden de amide groepen tijdelijk door ionische interacties afgeschermd om het ontstaan van gevouwen ketenkristallen tegen te gaan. Tijdens het verstrekken vindt rek-geïnduceerde kristallisatie plaats waardoor amide-amide waterstofbruggen herstellen, en een hoge mate van oriëntatie en kristalperfectie bereikt worden. Ondanks het feit dat deze aspecten essentieel zijn voor een hoge sterkte en een hoge modulus, worden de kristalliniteit en de smelttemperatuur aanzienlijk verlaagd door onvoldoende verwijdering van de ionen. Synchrotron röntgendiffractie toont aan dat de diffusie van ionen vooral tijdsafhankelijk is boven de glasovergangstemperatuur. In de oververhitte toestand van water bij 150°C leidt efficiënte verwijdering van ionen tot een hoge mate van kristalliniteit en hoge smelttemperatuur met behoud van kristalperfectie en oriëntatie. Echter, experimentele verificatie van de ultieme doelstelling: het maken van polyamide vezels met hoge sterkte en stijfheid, kon niet worden gerealiseerd vanwege het intrinsieke probleem dat tijdens/na het verstrekken alle ionen moeten worden verwijderd en dat vereist optimalisering t.a.v. vezel diameter en spin/verstrekeparameters. Deze optimale experimentele condities zijn van technologische aard en vereisen optimalisatie in een industriële setting. De auteur hoopt dat de resultaten in dit proefschrift zullen bijdragen aan een nieuwe technologische procesvoering met als resultaat een nieuwe generatie (super)sterke polyamide vezels.



Acknowledgements

I would like to spend the last words of my thesis on thanking all the people who have had a specific role in the past 4 years. First of all I would like to thank my promoters Sanjay Rastogi and Piet Lemstra. Dear Sanjay, I sincerely appreciate your continuous support, inspiring and honest thoughts, and above all your great enthusiasm that you've been transferring. I have enjoyed our travels to Grenoble, Mainz, U.K. and Japan where you have been both a great supervisor/guide and a good friend. I'm looking forward to the future! Inspiring and motivating have been Piet Lemstra's wise lessons. Beste Piet, ik ben je uiterst dankbaar voor de kans die je me hebt gegeven, de promotieplek in SKT, je vertrouwen en je kritische blik op het onderzoek en proefschrift. Daarnaast zijn er veel memorabele momenten waar ik met veel plezier aan terug denk.

Secondly, I express my sincere gratitude to the committee members Prof. E.D.T. Atkins, Dr. C.W.M. Bastiaansen, Prof. J. Van Hest, Prof. B. Lotz, Prof. E.W. Meijer, and Prof. H.W. Spiess for reading the dissertation and participation in the committee. I would like to thank especially Prof. E.D.T. Atkins, for the constructive comments and great discussion in Nailsea, and Prof. H.W. Spiess for the crucial solid state NMR spectroscopy experiments in his laboratories. Before proceeding, I would like to thank my first serious organic chemistry teacher Dr. Ludo Joosten (HSZuyd), though not contributing during the past 4 years, but for transferring his enthusiasm in understanding organic molecules!

The importance of solid state NMR spectroscopy in unravelling the role of water molecules and ions on influencing hydrogen bonding is clearly reflected by the numerous NMR spectra presented in the thesis. However, without the expertise and great help, which I gratefully acknowledge, of Dr. Robert Graf, Dr. Michael Ryan Hansen and Dr. Yao Yefeng the data acquisition would never be as fruitful as presented. Besides, Yao you're really a great friend and I'm looking forward to your move to The Netherlands. The collaboration with Dr. Nico van der Vegt and Dr. Berk Hess, though both being Dutch also working at MPIP in Mainz, has been fruitful as well and I would like to thank them for the great discussions in terms of molecular dynamics simulations.

People who have read the thesis will agree in stating that synchrotron WAXD experiments have been equally important as NMR spectroscopy. Hence, I would like to thank Dr. Gavin Vaughan, Dr. Theyencheri Narayanan and Dr. Wim Bras for the assigned beam-time at ID11, ID02 and BM26 respectively. Of course I could not survive the nights without the excellent technical support of the local contacts Dr. Caroline Curfs, Dr. Andy Götz (not truly local contact but very helpful), Dr. Aleksei Bytchkov and Dr. Jonathan Wright (ID11), Dr. Peter Boesecke and Dr. Anuj Shukla (ID02) and Dr. Giuseppe Portale.

Though the days and especially the nights were quite exhausting, I was fortunately not alone. Special thanks to my fellow XRD colleagues/friends: Esther, with whom I have

shared most beam-times, Sainath, Joost, Irina, Yogesh, Roy, Maria, Bastiaan, Carmen, Denka, Luigi for our great conversations and the interesting trip to Japan, Nilesh K., Nilesh P. and Carmine. Three persons introducing me to the world of X-rays deserve special words for thanking: Dr. Ann Terry, Dr. Guido Heunen and of course Sanjay.

Now, one may wonder whether I performed experiments in the Netherlands, or better, in Eindhoven. In fact I did, and I would like to thank my colleagues who have contributed to collect the data. Otto van Asselen for our extensive FTIR measurements and discussions, Joost, Martijn and Weizhen for programming the DSC experiments, Bob for extrusion and many nice discussions, Pauline for micro-toming, Anne for TEM, Bjorn for tensile testing, Gisela and Maria for DMTA, Tiny Verhoeven for XPS, Chunxia and Esther for TGA and Cees W. for safety. I also appreciate the support of Dr. Jurriaan van den Heuvel, Dr. Enno Klop and especially Lieda van Broekhoven (Teijin Aramid) for tensile testing. I am looking forward to the 1st of March. A person who does not fit in the above list is Yogesh because you've done much more. Dear Yogesh, I really enjoyed our fruitful collaboration that not only resulted in your Master Thesis but also to a great extent in chapter 5 of this thesis. I wish you a lot of success with your current PhD study. Concerning SKT, I would also like to thank Elly and Ineke for their kind secretarial support and the not yet mentioned colleagues for the great environment.

The thesis is a result of strong collaboration of SKT and the Polymer Technology Group Eindhoven (PTG/e), where I have been officially accommodated. Here, I would like to thank Dr. Laurent Nelissen, Jan van den Oever and Marleen Schaminee and all the other colleagues for providing the comfortable working environment and trips to Shanghai, London, Rotterdam and Lieshout. A comfortable and especially amicable atmosphere I encountered in STO.044 daily. Dear Roy (and Catia obviously) and Chunxia, though I've left STO.044 by now, I am sure that our friendship after 4 years in 1 office continues! Also the friendship with Mark, Martijn, Bjorn and Anne, Marloes, Mark B., Rob, Cees, and Thierry definitely prevails. Personally I think that it would be great to spread as much as possible! In this way we're expanding our nightlife beyond Breda, Eindhoven, Heerlen (especially for Martijn), 's Hertogenbosch, Tilburg (also for Martijn!) and even Nijmegen. For the coming part, in which I'll thank my family, I'll switch to Dutch.

In de laatste paragraaf van het dankwoord wil ik graag mijn familie bedanken die mij de afgelopen jaren enorm heeft gesteund. Allereerst mijn ouders: Hans en mam, jullie luisterend oor, gezellige etentjes, wijntjes en geweldige thuishaven zijn mij, en ook Valérie, zeer dierbaar. Dan heb ik natuurlijk nog 2 zussen, 2 broertjes, 2 zwagers, 2 schoonzusjes, 2 neefjes en 3 nichtjes in één gezin, die ik allen willen bedanken voor de gezellige sfeer. Dan resten er nog de allerlaatste woorden van mijn proefschrift om de meest bijzondere persoon te bedanken. Lieve Valérie, jouw eeuwige lol, begrip, steun en liefde zijn ontzettend belangrijk voor me en ik weet zeker dat we in Nijmegen en ver daarna een bijzondere tijd tegemoet gaan.



Curriculum Vitae

Jules Harings was born in Heerlen (The Netherlands) April 21, 1979. After finishing his secondary education at R.K. Scholengemeenschap Rombouts College, Brunssum, he studied Chemical Engineering at the University Zuyd (Heerlen). He completed his Bachelor degree with a graduation project performed at the 3B's Research Group in Biomaterials, Biodegradables and Biomimetics of the Department of Polymer Engineering at the University of Minho (Portugal) in 2002, focusing on the mechanical performance and in-vitro degradation behavior of soy protein based membranes and thermoplastics. The following years he spent as a research fellow at Rodenburg Biopolymers (Oosterhout - The Netherlands), investigating processing and structure-property relationships of bio-based and biodegradable thermoplastic starch-polyester blends.

His scientific interest in (bio)polymers triggered him to join the Laboratory of Polymer Technology of Prof. P.J. Lemstra at the Eindhoven University of Technology in 2005, working as a PhD student supervised by Prof. S. Rastogi. During his PhD study, he attended the 10th Oxford School on Neutron Scattering and completed four modules of the postgraduate course Register Polymer Science (RPK) of the National Dutch Research School PTN. The modules comprise; A - Polymer Chemistry, B - Polymer Physics, C - Polymer Properties and π - Polymer Innovations.

Starting on March 1, 2009, Jules continues his career at Teijin Aramid, the Netherlands.

List of Publications

Jules A.W. Harings, Otto van Asselen, Robert Graf, Rene Broos, Sanjay Rastogi, *The Role of Superheated Water on the Crystallization of N,N'-ethanediyl-bis(6-hydroxy-hexanamide); Crystallographic and Thermodynamic Implications*, Cryst. Growth Des. 2008, 8, 2469-2477.

Jules A.W. Harings, Otto van Asselen, Robert Graf, Rene Broos, Sanjay Rastogi, *The Role of Superheated Water on Shielding and Mediating Hydrogen Bonding in N,N'-ethanediyl-bis(6-hydroxy-hexanamide) Crystallization*, Cryst. Growth Des. 2008, 8, 3323-3334.

Jules Harings, Deshmukh Yogesh Sheshrao, Esther Vinken, Sanjay Rastogi, *Polyamides with reduced crystallinity*, European Patent Application 08152691.5 – 2115, 2008.

Jules A.W. Harings, Yefeng Yao, Otto van Asselen, Robert Graf, Rene Broos, Sanjay Rastogi, *Erasing Conformational Limitations in N,N'-1,4-Butanediyl-bis(6-hydroxy-hexanamide) crystallization from the superheated state of water*, Langmuir 2009, submitted.

Jules A.W. Harings, Yogesh S. Deshmukh, Robert Graf, Sanjay Rastogi, *A New Water-based Process for Reversible Shielding of Hydrogen Bonding in the Development of Oriented Polyamide Crystals*, in preparation 2009.

Jules A.W. Harings, Michael R. Hansen, Robert Graf, Sanjay Rastogi, *Strain Induced Crystallization of Polyamide 46 from Aqueous Lithium Iodide Solution*, in preparation 2009.

S. Rastogi, E. Vinken, J. Harings, J. Yin, A. Terry, *Dissolution of Hydrogen bonded Polymers in Water: from Synthetic to Biopolymers*, in NSTI Nanotech 2006, NSTI Nanotechnology Conference and Trade Show; Editors: M. Laudon & B. Romanovicz, Boston, United States 2006, Vol 2. 762-765.

Berk Hess, Jules A.W. Harings, Sanjay Rastogi, Nico F.A. van der Vegt, *Interaction of Water with N,N'-1,2-ethanediyl-bis(6-hydroxy-hexanamide) Crystals: A Simulation Study*, J. Phys. Chem. B 2009, 13, 627-631.